

UNIVERSITY OF ICELAND

Ph.D. Dissertation
in Chemistry

Computational Study of CO Adsorption and Step Formation on Transition-Metal-Doped Copper Surfaces

Magnus Andreas Hilduberg Christiansen

November 2026

FACULTY OF PHYSICAL SCIENCES

Computational Study of CO Adsorption and Step Formation on Transition-Metal-Doped Copper Surfaces

Magnus Andreas Hilduberg Christiansen

Dissertation submitted in partial fulfillment of a
Philosophiae Doctor degree in Chemistry

Ph.D. Committee:
Hannes Jónsson (Chair)
Elvar Örn Jónsson
Max García-Melchor

Opponents:
Anders Hellman
Karoliina Honkala

Faculty of Physical Sciences
School of Engineering and Natural Sciences
University of Iceland
Reykjavik, November 2026

Computational Study of CO Adsorption and Step Formation on Transition-Metal-Doped Copper Surfaces

(Computational Study of CO Adsorption and Step Formation on Transition-Metal-Doped Copper Surfaces)

Dissertation submitted in partial fulfillment of a *Ph.D.* degree in Chemistry

Copyright © 2026 Magnus Andreas Hilduberg Christiansen
All rights reserved

Faculty of Physical Sciences
School of Engineering and Natural Sciences
University of Iceland
Dunhagi 5
107 Reykjavík Reykjavik
Iceland

Telephone: 525-4700

Bibliographic information:
Magnus Andreas Hilduberg Christiansen, 2026, *Computational Study of CO Adsorption and Step Formation on Transition-Metal-Doped Copper Surfaces*, Ph.D.Dissertation, Faculty of Physical Sciences, University of Iceland, 122 pp.

Author ORCID: 0009-0004-9837-3469
ISBN: 978-9935-585-10-3

Printing: Háskólaprent ehf.
Reykjavik, Iceland, November 2026

Abstract

Copper-based single-atom alloys (SAAs) offer a way to modify the adsorption of molecules by introducing isolated atoms of a more reactive element into the copper surface. This thesis applies density functional theory (DFT) to investigate the capability of substitutional transition-metal atoms to adsorb multiple CO molecules and the implications for surface restructuring. Multiple CO adsorption is examined at first- and second-row substitutional transition-metal atoms in Cu(100) and Cu(111) terraces and islands, forming surface transition-metal carbonyl complexes. Calculations based on the RPBE and BEEF-vdW functionals are used to characterize adsorption energetics and the accompanying structural and electronic changes. Calculated C–O stretching frequencies provide possible experimental indicators of multiple CO adsorption, while minimum-energy paths obtained using the nudged elastic band method describe CO diffusion across copper island terraces and along steps.

Distinct CO adsorption patterns emerge across the transition metals studied. Late transition metals, such as Fe and Co, generally bind the first CO molecule strongly, with weaker binding for subsequent CO adsorption, while substitutional atoms with strong initial magnetic moments exhibit increasing differential binding energy as their magnetic moments decrease in concert with CO adsorption. Early transition metals, such as Sc and Y, bind the first CO molecule weaker than the later transition metals, but show smaller variations in differential binding energy for subsequent CO adsorption, and can adsorb up to four CO molecules more strongly than the corresponding copper surfaces. The initial CO binding energy alone therefore does not describe the capacity of a substitutional atom for multiple CO adsorption. On pure copper, CO binds preferentially at undercoordinated step sites and lowers the calculated step formation energy to half. The calculated CO migration barriers favor diffusion along the steps rather than escape from the steps to the terrace, suggesting that CO molecules collect at steps even when the overall surface coverage is low. The transition-metal carbonyl complexes also generally favor step sites over terraces, Ti and Zr being the exceptions. The multiple CO adsorption on substitutional transition-metal atoms thereby provides an additional energetic driving force for step formation and will tend to pin fluctuating steps at their location.

These results connect CO adsorption and formation of carbonyl complexes at substitutional transition-metal atoms with the formation and stability of undercoordinated Cu step sites. They suggest that a possible explanation of the observed increase in catalytic activity with dilute alloying is due to changes in surface morphology, in particular step formation. Steps lead to accumulations of CO, thereby increasing the opportunity for neighboring CO molecules to undergo C–C bond formation. Establishing the consequences for catalytic activity and product selectivity requires further investigation of reaction kinetics and the electrochemical environment. More generally, the findings highlight the importance of considering both multiple adsorption and adsorbate-induced restructuring when describing SAA catalysts, with implications beyond CO_2 reduction.

Ágrip

Með því að bæta stökum íbótaratómum hvarfgjarnara frumefnis í málmyfirborð (e. single-atom alloys, SAA) er hægt að breyta aðsogi sameinda og þar með stöðugleika þeirra á yfirborðinu. Í þessari ritgerð er þéttnifellafræði (DFT) beitt til að kanna hversu margar CO-sameindir geta sogast á slík íbótaratóm og áhrif þess á myndgerð yfirborðsins könnuð. Niðurstöðurnar sýna að íbótaratóm úr fyrstu og annarri röð hliðarmálmanna í Cu(100) og Cu(111) yfirborðum, bæði flötum og með eyjum, geta myndað karbónýl komplexa á yfirborðinu. Reikningar með RPBE- og BEEF-vdW-fellum eru notaðir til að meta orkubreytingar við aðsog CO sameinda sem og byggingar- og rafeindabreytingum sem því fylgir. Reiknaðar C–O-teygjutíðnir gefa mögulegar tilraunavísbendingar um bindingu margra CO-sameinda, og lágmarksorkuferlar fengnir með hnippta teygjubands (e. nudged elastic band) aðferðinni, lýsa sveimi CO sameinda yfir kopareyjar og meðfram þrepum.

Mismunandi eiginleikar koma fram eftir því hvaða hliðarmálmi íbótaratómið tilheyrir. Síðhliðarmálmar, svo sem Fe og Co, binda yfirleitt fyrstu CO-sameindina sterkt en bindingin er veikari eftir því sem fleiri CO sameindir bætast við. Íbótaratóm með sterkt segulvægi sýna hins vegar vaxandi mismunabindingarorku eftir því sem segulvægi þeirra minnkar samhliða CO-aðsogi. Snemmhliðarmálmar, svo sem Sc og Y, binda fyrstu CO-sameindina veikar en síðhliðarmálmar, en sýna minni breytileika í mismunabindingarorku við frekara aðsog og geta bundið allt að fjórar CO-sameindir sterkar en samsvarandi hreint koparyfirborð. Upphafleg bindingarorka CO ein og sér lýsir því ekki getu íbótaratóms til að binda margar CO-sameindir. Á hreinum koparyfirborðum binst CO helst á yfirborðsatóm sem hefur fáa nágranna, svo sem við þrep, og þetta lækkar reiknaða myndunarorku þrepa um helming. Reiknaðir orkuhólar fyrir færslu CO sameinda á yfirborðinu sýna að sameindir sem ná að tengjast þrepi eru líklegar til að sveima eftir jaðri þrepins, sem bendir til þess að CO-sameindir safnist þar saman jafnvel þótt heildarþekja CO á yfirborðinu sé lág. Karbónýl komplexarnir hafa yfirleitt lægri orku við þrep en á flötum yfrborðum, Ti and Zr eru undantekningarnar. Þetta sýnir að binding CO-sameinda á íbótaratómin lækkar myndunarorku þrepa enn frekar og komplexarnir geta hindrað sveiflukennda færslu þrepa sem verða á vegi þeirra.

Þessar niðurstöður sýna að binding margra CO-sameinda á íbótaratóm hvarfgjarnra hliðarmálmsatóma geta lækkað myndunarorku þrepa. Möguleg útskýring á mældri aukningu á hvatavirkni með íbótaratómum er því óbein áhrif vegna breytinga á formgerð yfirborðsins, þá einkum þrepamyndun. Þrep auka líkur á að tvær CO-sameindir sitji í aðliggjandi sætum og geta þar með myndað C–C-tengi. Til að ákvarða áhrif á hvatarvirkni og gerð myndefnanna þarf frekari rannsóknir á hvarfhraða og rafefnafræðilegum eiginleikum. Almennt undirstrika niðurstöðurnar mikilvægi þess að taka tillit til bæði bindingar fleri en einnar sameindar á íbótaratóm og áhrif þess á yfirborðsmyndgerð SAA hvata, einkum í tenglsum við rafafoxun CO_2.

Table of Contents

List of Figures xi

List of Tables xiii

List of Publications xv

Abbreviations xvii

Acknowledgements xix

1 Introduction 1

2 Theoretical Background and Computational Methods 5
2.1 Quantum-Mechanical Theory . . . 5
2.1.1 Schrödinger Equation . . . 5
2.1.2 The Molecular Many-body Hamiltonian . . . 5
2.1.3 Born–Oppenheimer Approximation . . . 6
2.1.4 The Electronic Many-body Problem . . . 7
2.2 Density Functional Theory . . . 8
2.2.1 From wavefunction to the electronic density . . . 8
2.2.2 Hohenberg-Kohn Theorems . . . 9
2.2.3 Kohn-Sham Density Functional Theory . . . 10
2.2.4 Exchange-Correlation Approximations . . . 11
2.3 Dispersion Interactions . . . 12
2.3.1 Origin of Dispersion Interactions . . . 12
2.3.2 Non-local van der Waals Density Functionals . . . 13
2.3.3 BEEF-vdW . . . 13
2.4 Periodic Systems and Plane-Wave DFT . . . 14
2.4.1 Periodic Boundary Conditions . . . 14
2.4.2 Bloch's Theorem . . . 14
2.4.3 Reciprocal Space . . . 15
2.4.4 Brillouin-Zone Sampling . . . 16
2.4.5 Plane-Wave Basis Sets . . . 17
2.4.6 Energy Cutoff and Basis-Set Convergence . . . 17
2.5 Projector Augmented-Wave Method . . . 18
2.6 Metallic Systems and Electronic Occupations . . . 19
2.7 Surface Models and Energetics . . . 20
2.7.1 Periodic Slab Representation . . . 21
2.7.2 Terraces, Steps, and Substitutional Impurities . . . 21
2.7.3 Adsorption and Relative Energies . . . 22
2.7.4 Vibrational Analysis and Thermochemical Corrections . . . 22

2.8 Minimum-Energy Paths and Transition States . . . 23
2.8.1 Potential-Energy Surfaces . . . 23
2.8.2 Nudged Elastic Band Method . . . 24
2.8.3 Harmonic Transition-State Theory . . . 26
2.9 Electrochemical Density Functional Theory Modeling . . . 27
2.9.1 The Electrochemical Interface . . . 28
2.9.2 Electrode Potential and the Electronic Chemical Potential . . . 29
2.9.3 The Computational Hydrogen Electrode . . . 31
2.9.4 Solvation and Electrolyte Models . . . 32
2.9.5 Constant-Charge and Constant-Potential DFT . . . 34
2.9.6 Grand-Canonical Density Functional Theory . . . 35

3 Electrochemical Reduction of Carbon Dioxide 39
3.1 Background and Historical Development . . . 39
3.2 Reaction Pathways and Product Selectivity . . . 41
3.2.1 Product Formation and Measures of Selectivity . . . 42
3.2.2 Initial Reduction to CO and Formate . . . 42
3.2.3 Further Reduction of CO and Carbon–Carbon Coupling . . . 43
3.2.4 Competition with Hydrogen Evolution and the Operating Environment 44
3.3 Copper Surface Structure and Reactivity . . . 46
3.3.1 Terrace Orientation and Product Selectivity . . . 46
3.3.2 Steps, Defects and Local Atomic Environments . . . 46
3.3.3 Nanostructure, Roughness, and the Reaction Environment . . . 48
3.3.4 Structural Evolution under Operating Conditions . . . 50
3.3.5 Implications for Atomistic Modeling . . . 51
3.4 CO Adsorption, Coverage, and Surface Mobility . . . 52
3.4.1 CO–Surface Bonding and Adsorption . . . 52
3.4.2 Adsorption Energetics, the Sabatier Principle, and Volcano Relationships 52
3.4.3 Coverage Effects and Lateral Interactions . . . 53
3.4.4 CO Diffusion on Terraces and Steps . . . 55
3.5 C–C Coupling and Multicarbon Products . . . 55
3.6 Substitutional Impurities and Copper-Based Single-Atom Alloys . . . 56
3.6.1 Local Electronic Structure and Adsorption . . . 57
3.6.2 Multiple CO Adsorption at an Isolated Impurity . . . 57
3.6.3 Adsorbate-Induced Redistribution and Structural Stability . . . 58
3.7 Open Questions and Connection to This Thesis . . . 59

4 Summary of Publications 61
4.1 Publication I . . . 61
4.2 Publication II . . . 66
4.3 Publication III . . . 71

5 Conclusion and Outlook 75

References 77

Appendix A: Publications 89

Publication I **91**

Publication II **97**

Publication III **107**

List of Figures

2.1 Schematic illustration of the nudged elastic band (NEB) method on a model potential-energy surface. Left: three-dimensional representation of the surface and paths connecting two minima. Right: corresponding contour representation, with circles denoting discrete images along the paths. Blue circles indicate the endpoint minima, and the green circle marks the saddle point along the minimum-energy path. The inset illustrates the perpendicular component of the physical force, $F_{\perp}^{r}$, and the parallel component of the spring force, $F_{\parallel}^{k}$, used to optimize the band. Source: RheoMan project website, Université de Lille [53]. 25

3.1 Two-descriptor map of metal-electrode selectivity. The horizontal axis represents the adsorption energy of an isolated CO molecule. The vertical axis represents the differential adsorption energy of an on-top H atom above one monolayer coverage. The colored region indicates competition between hydrogen evolution and hydrocarbon/alcohol formation, while the right-hand regions indicate CO and formate production. Reproduced from Hussain et al. [100]. 43

3.2 Proposed reaction network for CO_2 electroreduction on copper by Seger et al. Columns distinguish the number of carbon atoms, while rows indicate the cumulative number of electrons transferred from CO_2. The asterisk denotes an adsorbed intermediate. Line styles distinguish reaction-step types, and red arrows identify proposed rate- or selectivity-limiting steps. The formate branch differs from the direct hydrogen/electron-transfer pathway discussed in Section 3.2.2. Reproduced from Seger et al. [88]. 45

3.3 Facet-dependent product formation during CO electroreduction on copper single-crystal electrodes. Mass-spectrometric ion-current signals associated with ethylene ($m/z = 26$), methane ($m/z = 15$), and hydrogen ($m/z = 2$) are shown as a function of electrode potential versus RHE. The different potential dependencies illustrate the influence of surface orientation on CO-reduction pathways. Ion currents are shown in arbitrary units and do not directly represent Faradaic efficiencies. Adapted from Schouten et al. [103]. 47

3.4 (a–j) Low-temperature scanning tunneling microscopy images of pristine and stepped Cu(111), and pristine, intermediate, and stepped Cu(100) surfaces. The modified surfaces were obtained through successive CO_2 electroreduction cycles followed by sputtering and annealing under ultrahigh vacuum. (k–o) Corresponding step orientation distributions, weighted by step length; the insets illustrate prominent step geometries on Cu(100). (p–t) Faradaic efficiencies for gaseous products (colored bars, left axis) and step densities (gray bars, right axis). Electrocatalysis was performed at -1.1 V vs. RHE in 0.1 M $KHCO_3$ for 1 h. Increased step density is associated with greater hydrocarbon selectivity, while differences between the Cu(100) surfaces highlight the additional importance of step geometry. Reproduced from Cheng et al. [14]. 49

3.5 Activity map for CO dimerization 54

4.1 Minimum energy structures of (a) Sc, (b) Ti, (c) V, (d) Cr, (e) Mn, (f) Fe, (g) Co and (h) Ni on the Cu(100) surfaces with 0-4 CO molecules adsorbed to the substituent atom 62
4.2 Minimum energy structures of (a) Sc, (b) Ti, (c) V, (d) Cr, (e) Mn, (f) Fe, (g) Co and (h) Ni on the Cu(111) surfaces with 0-4 CO molecules adsorbed to the substituent atom 63
4.3 Left: The Cu(100) island and Cu(711) sawtooth structures, and the adsorption sites near the step that were compared. Right: differential adsorption energy of CO adsorbed at the step of a Cu(100) island, or at the equivalent locations on a Cu(711) sawtooth structure, with respect to the adsorption energy of CO on the Cu(100) surface. 72
4.4 Chemical contribution to the CO binding energy, $E_{\text{bind,chem}}$, for V, Cr, and Mn substitutional atoms at Cu(100) and Cu(111) island steps, plotted against $(\varepsilon_{d\uparrow} - \varepsilon_{d\downarrow})\mu$. Here, $\varepsilon_{d\uparrow}$ and $\varepsilon_{d\downarrow}$ are the spin-resolved d-band centers, and μ is the magnetic moment of the substitutional atom divided by its number of d electrons. Blue, orange, and green points represent configurations containing one, two, and three adsorbed CO molecules, respectively. 73
4.5 Potential dependence of the grand-canonical potential difference between step and terrace transition-metal carbonyl configurations containing substitutional 3d atoms in Cu(100). Negative values indicate a preference for the step configuration. Dark blue, light blue, and beige bars show results at 0.0, -0.6, and -1.0 V versus RHE, respectively. Calculations were performed using VASPsol++ for an aqueous electrolyte at pH 7. 74

List of Tables

4.1 Binding energy, outward displacement and magnetic moment in units of unpaired electrons for substituent atoms, M, on the Cu(100) surface with up to 4 CO molecules adsorbed. The change in partial Bader charges of the M atom, the first neighbouring Cu atoms in the surface layer and of the CO molecule. 64

4.2 Binding energy, outward displacement and magnetic moment in units of unpaired electrons for substituent atoms M on the Cu(111) surface with up to 4 CO molecules adsorbed. The change in partial Bader charges of the M atom, the first neighbouring Cu atoms in the surface layer and of the CO molecule. 65

4.3 Differential binding energy, vdW correction contribution, outward displacement, and magnetic moment (in unpaired electron units) for 3d transition metal substituent atoms (M) on the Cu(100) surface with up to 4 CO molecules adsorbed. 67

4.4 Differential binding energy, vdW correction contribution, outward displacement, and magnetic moment (in unpaired electron units) for 3d transition metal substituent atoms (M) on the Cu(111) surface with up to 4 CO molecules adsorbed. 68

4.5 Differential binding energy, vdW correction contribution, outward displacement, and magnetic moment (in unpaired electron units) for 4d transition metal substituent atoms (M) on the Cu(100) surface with up to 4 CO molecules adsorbed. 69

4.6 Differential binding energy, vdW correction contribution, outward displacement, and magnetic moment (in unpaired electron units) for 4d transition metal substituent atoms (M) on the Cu(111) surface with up to 4 CO molecules adsorbed. 70

List of Publications

This thesis is based on the following original main author publications:

Publication I:	**Magnus A. H. Christiansen**, Alejandro Peña-Torres, Elvar Ö. Jónsson, and Hannes Jónsson, "Single-Atom Substituents in Copper Surfaces May Adsorbed Multiple CO Molecules." *J. Phys. Chem. Lett.* 30 May 2024; 15 (21): 5654–5658. https://doi.org/10.1021/acs.jpclett.4c00899
Publication II:	**Magnus A. H. Christiansen**, Wei Wang, Elvar Ö. Jónsson, Giancarlo Cicero, and Hannes Jónsson, "Multiple Adsorption of CO Molecules on Transition Metal Substitutional Impurities in Copper Surfaces." *ChemCatChem* 17, no. 18 (2025): e00765. https://doi.org/10.1002/cctc.202500765
Publication III:	**Magnus A. H. Christiansen**, Elvar Ö. Jónsson, and Hannes Jónsson, "Adsorption of CO Molecules on Stepped Copper Surfaces With and Without Transition Metal Impurities." (submitted for review)

All main author publications are reprinted by kind permission of the publishers.

The following publications have been co-authored:

Publication IV:	Michele Re Fiorentin, Michele G. Bianchi, **Magnus A. H. Christiansen**, Anna Ciotti, Francesca Risplendi, Wei Wang, Elvar Ö. Jónsson, Hannes Jónsson, and Giancarlo Cicero, "Methodological Frameworks for Computational Electrocatalysis: From Theory to Practice." *Small Methods* 10, no. 5 (2026): e01542. https://doi.org/10.1002/smtd.202501542
Publication V:	Julian Beßner, Anoop A. K. Nair, **Magnus A. H. Christiansen**, Timo Jacob, Hannes Jónsson, and Elvar Ö. Jónsson, "Polarizable Embedding QM/MM for Periodic Systems." *arXiv* arXiv:2605.09752 (2026). (preprint)

Abbreviations

CO2RR CO_2 reduction reaction

DFT density functional theory

SCF self consistent field

HF Hartree–Fock

GGA generalized gradient approximation

LDA local density approximation

PBE Perdew–Burke–Ernzerhof

RPBE revised PBE

vdW-DF van der Waals density functional

BEEF-vdW Bayesian error estimation functional with van der Waals correlation

fcc face-centered cubic

hcp hexagonal close-packed

SAA single-atom alloy

NEB nudged elastic band

PAW projector augmented-wave

PES potential energy surface

IDPP image-dependent pair potential

HTST harmonic transition-state theory

SHE standard hydrogen electrode

RHE reversible hydrogen electrode

CHE computational hydrogen electrode

VASP Vienna Ab Initio Simulation Package

Acknowledgements

This work was funded by the EU's Horizon 2021 programme under the Marie Skłodowska-Curie Doctoral Networks (MSCA-DN) grant agreement No 101072830 (ECOMATES). Views and opinions expressed are those of the authors and do not necessarily reflect the official policy or position of the European Union or the Granting Authority, and neither can be held responsible for them.

1 Introduction

Reducing the use of fossil resources is an important part of addressing climate change. In the chemical industry, these resources are used both to power production and to supply the carbon needed to make fuels, chemicals, and materials. Replacing fossil energy with low-emission electricity therefore addresses only part of the problem. Alternative sources of carbon and production methods are also needed to reduce the industry's contribution to greenhouse-gas emissions [1].

Electrochemical CO_2 reduction offers a way to use CO_2 as a source of carbon for producing fuels and chemicals. Electricity supplies the energy needed for the conversion, allowing electrical energy to be stored in chemical products. When the electricity comes from sources with low emissions, this could reduce the use of fossil resources in chemical production [2, 3].

However, using CO_2 does not by itself make the process beneficial for the climate. The emissions associated with capturing CO_2, generating electricity, and separating the products must also be considered. The source of the CO_2 and the production process being replaced are important, as is the eventual use of the products. Fuels and many chemicals release their carbon again during use or disposal. CO_2 conversion therefore generally recycles carbon rather than permanently removing it from the atmosphere, but can still reduce emissions when it replaces a process with higher emissions [4, 5].

Several challenges must also be addressed before electrochemical CO_2 reduction can compete economically with existing production methods. Electricity consumption and price contribute to operating costs, while the current density determines how much electrode area is needed. Product selectivity and concentration affect the amount of separation required, and the electrodes must maintain their performance over long periods of operation. These requirements depend on the catalyst, electrolyte, membrane, and reactor design. Improvements in one part of the process must therefore be considered together with the others [2, 3, 6].

At the catalyst level, the aim is to promote the desired reactions while limiting competing pathways. Copper is particularly interesting because it can catalyze CO_2 reduction beyond CO to hydrocarbons and alcohols, including ethylene and ethanol. Several reactions compete on copper, and the product distribution depends on the applied potential, electrolyte, and surface structure. Hydrogen evolution also competes with CO_2 reduction. Understanding these effects requires knowledge of the adsorbed intermediates and the surface sites at which they bind and react [7, 8, 9].

Adsorbed CO is an important intermediate in CO_2 reduction on copper. Its interaction with the electrode influences whether it remains adsorbed, desorbs, or undergoes further reaction. Its local availability also matters for reactions involving two carbon-containing intermediates. Consequently, the adsorption energy of CO has frequently been used to characterize and compare candidate catalysts. The interpretation of this quantity, however, depends on the adsorption configuration and the surrounding surface.

One approach to modifying copper is to introduce a small concentration of another element. For example, adding 0.4% Co has been reported to increase the combined Faradaic efficiency for ethylene and ethanol formation by a factor of two [10]. When individual substitutional atoms remain atomically dispersed within the copper host, they form the chemically distinct sites characteristic of single-atom alloys (SAAs). These sites can modify adsorption while retaining a surrounding copper environment. Their properties depend on the identity of the minority element, its coordination to the host, and the molecules already bound to it [11]. Some of these substitutional atoms can adsorb several CO molecules, forming transition-metal-carbonyl complexes. Multiple CO adsorption has been observed experimentally at isolated Rh [12] and Co [13] atoms in copper surfaces.

These observations show that a single substitutional atom can provide an adsorption site for several CO molecules. Therefore, the binding energy of the first CO molecule alone in some cases does not provide an accurate descriptor. This motivates a systematic comparison of multiple CO adsorption across transition-metal atoms embedded in copper surfaces.

Copper surfaces contain terraces, steps, and other defects, whose relative energies can change in the presence of adsorbates and other reaction conditions. Step atoms have fewer neighboring metal atoms than terrace atoms and exhibit different adsorption and diffusion properties. Experimental results have identified undercoordinated step sites as important for CO_2 reduction on copper [14]. Preferential adsorption at these sites can, in turn, lower the energetic cost of forming them. Experimental observations of copper restructuring and the relationship between step density and CO2RR motivate treating surface structure as a property that responds to the chemical environment [15, 14, 16].

These observations raise the question of whether the propensity of substitutional transition-metal atoms for multiple CO adsorption can contribute to copper surface restructuring. Formation of surface carbonyl complexes could influence the energetic cost of forming steps, providing a possible indirect contribution of dilute alloying to catalytic behavior.

The aim of this thesis is to determine the propensity of substitutional transition-metal atoms to adsorb multiple CO molecules and the implications for copper surface restructuring. Three connected questions are addressed:

1. How many CO molecules can individual substitutional transition-metal atoms in Cu(100) and Cu(111) adsorb, and how do their differential binding energies depend on the element?
2. How do differences in CO adsorption and diffusion between copper terraces and steps contribute to the accumulation of CO at steps?
3. How does the formation of surface transition-metal-carbonyl complexes affect the energetic cost of forming copper steps, and what are the implications for surface morphology?

Answering these questions helps establish how substitutional atoms bind multiple CO molecules and whether their carbonyl complexes favor the formation of undercoordinated copper steps. This provides a basis for investigating how dilute alloying influences both adsorption and surface morphology. Establishing the consequences for catalytic rates and product selectivity requires further calculations of the competing reaction pathways and their kinetics.

This thesis uses spin-polarized density functional theory (DFT) calculations to investigate Cu(100) and Cu(111) terraces and islands containing substitutional transition-metal atoms. Structures with different numbers of adsorbed CO molecules are optimized, and differential

binding energies are calculated for each subsequent CO adsorption. These energies are compared with CO adsorption on the corresponding copper terrace surface to determine whether adsorption at the impurity is energetically preferred. Atomic displacements, magnetic moments, and charge distributions are also examined.

Publication I investigates first-row transition-metals, Sc–Ni, using the RPBE functional. Publication II extends the investigation to include second-row transition metals, Y–Pd, and uses BEEF-vdW to examine adsorption across both the 3d and 4d series and the contribution from dispersion interactions. Calculated C–O stretching frequencies provide possible experimental signatures of selected carbonyl configurations. Publication III examines copper islands with and without substitutional transition-metal atoms. Adsorption and step-formation energies are calculated, while minimum-energy paths describing the CO diffusion along the step and between the step and terrace are obtained using the nudged elastic band (NEB) method. Comparisons of the potential energies of configurations with substitutional atoms at steps and terraces establish the preferred locations of bare substitutional transition-metal atoms and their corresponding carbonyl complexes. Preliminary constant-potential calculations using VASPsol++, presented alongside Publication III, examine how applied potential affects this preference for selected Cu(100) configurations.

The rest of this thesis is organized as follows: Chapter 2 introduces the theoretical background and computational methods. Chapter 3 reviews CO_2 reduction on copper-based catalysts, focusing on CO adsorption, the copper surface structure, and SAAs. Chapter 4 summarizes the three original publications and presents additional calculations. Chapter 5 brings together the main findings and discusses their implications, limitations, and possible directions for future research.

2 Theoretical Background and Computational Methods

2.1 Quantum-Mechanical Theory

2.1.1 Schrödinger Equation

The basis of much of quantum mechanics is the Schrödinger equation, and the aim for most computational chemistry methods is to sufficiently approximate its solution [17]. The Schrödinger equation defines the evolution of a quantum mechanical state, and connects the total energy of a many-particle system to its wavefunction, Ψ. The many-particle wavefunction describes the state of the system, and its time evolution is governed by the time-dependent Schrödinger equation [18],

$$i\hbar\frac{\partial}{\partial t}\Psi(\mathbf{x},t) = \hat{H}\Psi(\mathbf{x},t). \tag{1}$$

Here $\hbar$ is the reduced Planck constant, $\hat{H}$ is the Hamiltonian operator representing the total energy. The variable x, collectively denotes the spatial and spin coordinates of the particles. In the case where the Hamiltonian has no direct time dependence, the wavefunction can then be decomposed into spatial and time-dependent components, with the spatial component called the stationary state. This provides the time-independent Schrödinger equation,

$$\hat{H}\Psi(\mathbf{x}) = E\Psi(\mathbf{x}), \tag{2}$$

where E is the total energy. Determining the wavefunction and calculating its energy is therefore an eigenvalue problem of the Hamiltonian [17, 18]. Multiplying the stationary state with a time-evolution operator

$$\Psi(\mathbf{x},t) = e^{-iEt/\hbar}\Psi(\mathbf{x},0), \tag{3}$$

restores the time dependence of the wavefunction.

2.1.2 The Molecular Many-body Hamiltonian

For a molecular system containing M atoms with an equivalent number of nuclei and N number of electrons, the Hamiltonian must describe the kinetic energies and all electrostatic interactions between the particles of the system. The Hamiltonian can then be expressed as,

$$\hat{H} = \hat{T}_n + \hat{T}_e + \hat{V}_{nn} + \hat{V}_{ee} + \hat{V}_{en}. \tag{4}$$

Here $\hat{T}_n$ and $\hat{T}_e$ are the kinetic operators of the nuclei and electrons, and they are written as

$$\hat{T}_n = -\sum_A^M \frac{\hbar^2}{2m_A}\nabla_A^2, \tag{5}$$

and

$$\hat{T}_e = -\sum_i^N \frac{\hbar^2}{2m_e}\nabla_i^2, \tag{6}$$

respectively. Here, m_A is the mass of nucleus A, m_e is the electron mass, and ∇^2 is the Laplacian operator. $\hat{V}_{nn}$, $\hat{V}_{ne}$, and $\hat{V}_{ee}$ are the interaction operators of nucleus–nucleus, nucleus–electron, and electron–electron interactions, respectively. They are each expressed as:

$$\hat{V}_{nn} = \sum_{A<B}^M \frac{Z_A Z_B e^2}{4\pi\varepsilon_0|\mathbf{R}_A - \mathbf{R}_B|}, \tag{7}$$

$$\hat{V}_{ee} = \sum_{i<j}^N \frac{e^2}{4\pi\varepsilon_0|\mathbf{r}_i - \mathbf{r}_j|}, \tag{8}$$

and

$$\hat{V}_{en} = -\sum_{A,i}^{M,N} \frac{Z_A e^2}{4\pi\varepsilon_0|\mathbf{r}_i - \mathbf{R}_A|}. \tag{9}$$

Here, e is the elementary charge, ε_0 is the vacuum permittivity, $\mathbf{R}_A$ and Z_A are the coordinate and nuclear charge number of nucleus A, and $\mathbf{r}_i$ is the coordinate of electron i [17]. In these terms the wavefunction of a molecular system is dependent on the coordinates of both the nuclei and electrons,

$$\Psi = \Psi(\mathbf{r}_1, \mathbf{r}_2, \ldots, \mathbf{r}_N, \mathbf{R}_1, \mathbf{R}_2, \ldots, \mathbf{R}_M). \tag{10}$$

The major difficulty when it comes to solving the time-independent Schrödinger equation is the coupled motion of the particles involved, especially that stemming from the electron–electron interaction. For general interacting many-particle systems, exact analytical solutions are unavailable, and numerical solutions become increasingly demanding as the system grows, and especially for an electrode systems that can contain up to hundreds of atoms and thousands of electrons.

This is the motivation for a series of approximations that I will go over in the following sections. The first is the Born–Oppenheimer, which separates the electron and nuclei wavefunctions.

2.1.3 Born–Oppenheimer Approximation

The Born–Oppenheimer approximation assumes that because of the great difference in the masses between the electrons and the nuclei, which are several thousand times heavier, that motion of the electrons occur at such a speed, that the electrons are able to instantaneously rearrange themselves according to changes in nuclear positions. This means that, under the Born–Oppenheimer approximation, the wavefunction of the total system can be expressed as the product of the electronic wavefunction, $\psi(\mathbf{r};\mathbf{R})$, and the nuclear wavefunction, $\chi(\mathbf{R})$,

$$\Psi(\mathbf{r},\mathbf{R}) \approx \psi(\mathbf{r};\mathbf{R})\chi(\mathbf{R}). \tag{11}$$

Here, $\mathbf{r}$ is the electronic coordinates and $\mathbf{R}$ is the nuclear coordinates. The nuclear coordinates, $\mathbf{R}$, are only included as a parameter in the electronic wavefunction, $\psi(\mathbf{r};\mathbf{R})$ [19, 17]. The nuclear positions are held fixed when solving the electronic problem. The electronic energy and nuclear repulsion then define the potential-energy surface for nuclear motion. Under this approximation the Hamiltonian is reduced to

$$\hat{H}_{\text{elec.}} = \hat{T}_e + \hat{V}_{ee} + \hat{V}_{en}, \tag{12}$$

also called the electronic Hamiltonian. The electronic Schrödinger equation is then

$$\hat{H}_{\text{elec.}}\,\psi(\mathbf{r};\mathbf{R}) = E_{\text{elec.}}\,\psi(\mathbf{r};\mathbf{R}). \tag{13}$$

This energy together with the nuclear repulsion defines the potential-energy surface, which the nuclei move on,

$$E_{\text{PES}}(\mathbf{R}) = E_{\text{elec}}(\mathbf{R}) + V_{\text{nn}}(\mathbf{R}), \tag{14}$$

In geometry optimizations E_{PES} is minimized with respect to the nuclear coordinates and stable structures correspond to local minima on the potential-energy surface. Reaction pathways and transition states can be identified by exploring the surface between these minima. The Born–Oppenheimer as such allows us to calculate the energy of the surfaces, reactants, products, etc. in the catalytic systems.

2.1.4 The Electronic Many-body Problem

Despite the Born–Oppenheimer approximation, the resulting electronic Schrödinger equation remains an imposing many-body problem. For a system containing N electrons, the electronic wavefunction depends on both the $3N$ spatial coordinates, in addition to the spin degrees of freedom of every electron,

$$\Psi = \Psi(\mathbf{x}_1, \mathbf{x}_2, \ldots, \mathbf{x}_n). \tag{15}$$

This means that the complexity of the system increases rapidly as the number of electrons increases.

The difficulty comes from the electron-electron interaction in the Hamiltonian, because the potential energy of one electron is dependent on the immediate positions of all other electrons. The motions of the electrons are in this way coupled, and cannot be separated into single electron wavefunctions. The many-electron Schrödinger equation can therefore not be solved exactly and analytically for general systems larger than a couple of electrons, and numerical treatment is prohibitively expensive as the number of electrons increases [20].

Electronic-structure methods therefore rely on approximations that treat the many-body electron systems in a more manageable way. One of the earliest approaches was introduced by Hartree through the self consistent field (SCF) method. Rather than treating the correlated motion of all electrons simultaneously, the Hartree method assumes that each electron moves independently in an effective potential of nuclei and the average distribution of the other electrons [21]. Under this approximation, the N-electron wavefunction is written as a product of single-electron orbitals,

$$\Psi(\mathbf{x}_1, \mathbf{x}_2, \ldots, \mathbf{x}_n) \approx \psi_1(\mathbf{x}_1)\psi_2(\mathbf{x}_2)\ldots\psi_n(\mathbf{x}_n). \tag{16}$$

The equation, however, must be solved iteratively, since the effective potential on a single electron is dependent on the densities obtained from the remaining orbitals. Starting from an initial set of orbitals, a new effective potential is constructed and the orbitals are recalculated. This process is iterated over until the self-consistency is reached for the orbitals, electron density, and total energy.

The Hartree product alone does not satisfy the antisymmetry required of electrons as fermions, i.e. the wavefunction must change sign when two electrons are exchanged

$$\Psi(\ldots, \mathbf{x}_i, \ldots, \mathbf{x}_j, \ldots) = -\Psi(\ldots, \mathbf{x}_j, \ldots, \mathbf{x}_i, \ldots). \tag{17}$$

This requirement is incorporated in Hartree-Fock theory by representing the many-electron wavefunction as a single Slater determinant [22, 23],

$$\Psi_{HF} = \frac{1}{\sqrt{N!}} \begin{vmatrix} \chi_1(\mathbf{x}_1) & \chi_2(\mathbf{x}_1) & \cdots & \chi_N(\mathbf{x}_1) \\ \chi_1(\mathbf{x}_2) & \chi_2(\mathbf{x}_2) & \cdots & \chi_N(\mathbf{x}_2) \\ \vdots & \vdots & \ddots & \vdots \\ \chi_1(\mathbf{x}_N) & \chi_2(\mathbf{x}_N) & \cdots & \chi_N(\mathbf{x}_N) \end{vmatrix}. \tag{18}$$

Exchanging two electrons swaps two rows of the determinant and changes its sign, ensuring that the wavefunction is antisymmetric and satisfies the Pauli exclusion principle.

The single-electron orbitals are obtained by minimizing the total electronic energy according to the variational principle. This gives the Hartree-Fock equations,

$$\hat{F}\psi_i = \varepsilon_i \psi_i, \tag{19}$$

where $\hat{F}$ is the Fock operator,

$$\hat{F} = \hat{h} + \sum_{j=1}^{N} (\hat{J}_j - \hat{K}_j). \tag{20}$$

Here, $\hat{h}$ contains the single-electron kinetic energy and interaction with the nuclei. The operators $\hat{J}_j$ and $\hat{K}_j$ describe the Coulomb and exchange contributions associated with occupied spin orbital j, respectively.

The Hartree–Fock equation is solved self-consistently, since the Fock operator is dependent on the occupied orbitals [20].

The problem of the many-electron system is thereby scaled down to a series of one-electron equations that account for exchange within the single-determinant approximation. It does not, however, describe the correlated motion of the electrons beyond their antisymmetry. The correlation energy is therefore the difference between the real ground-state and Hartree–Fock energies

$$E_{\text{corr.}} = E_{\text{exact}} - E_{\text{HF}} \tag{21}$$

Recovering the missing correlation energy using wavefunction-based methods generally becomes increasingly computationally demanding as the size of the system grows. This incentivizes an alternative description of the electronic many-body system as a functional of the much simpler electron density instead of the many-electron wavefunction. This is the motivation behind DFT.

2.2 Density Functional Theory

2.2.1 From wavefunction to the electronic density

In DFT the many-body electron problem is dealt with by realizing that the system can be described as a functional of the electron density, $n(r)$, which depends only on three spatial variables. The motivation behind this is that the many-electron wavefunction that describes an N-electron system, is dependent on the $3N$ spatial coordinates and N spin coordinates of all of the electrons. It therefore becomes prohibitively expensive to solve for larger systems, and using the density, $n(r)$, instead of the wavefunction Ψ would provide a great reduction of the problem [17].

The electron density can be obtained from the many-electron wavefunction by integrating over the coordinates of all but one electron,

$$n(\mathbf{r}_1) = N \sum_{\text{spin}} \int |\Psi(\mathbf{x}_1, \mathbf{x}_2, \ldots, \mathbf{x}_n)|^2 \, \mathrm{d}\mathbf{x}_2 \ldots \mathrm{d}\mathbf{x}_n. \tag{22}$$

The electron density $n(\mathbf{r})$ gives the expected number of electrons per unit volume and integrates to N. Describing the electron-system in terms of the density instead of the wavefunction is therefore a major reduction in complexity. The question then becomes whether the much simpler electron density contains sufficient information to determine the properties of the interacting electron-system [17].

2.2.2 Hohenberg-Kohn Theorems

In 1964 Hohenberg and Kohn established the theoretical basis on which all of DFT is based with their two theorems [24, 17]. Their two theorems justify using the density as the central variable instead of the many-electron wavefunction.

The first Hohenberg–Kohn theorem is based on their proof that two external potentials, which are different by more than a constant, cannot produce the same ground-state electron density $n(r)$. Based on this observation Hohenberg and Kohn state in their first theorem that *'the external potential* v_{ext} *is a unique functional of* $n(r)$*; since in turn* v_{ext} *fixes* $\hat{\mathrm{H}}$ *we see that the full many particle ground state is a unique functional of* $n(r)$*'* [24, 17]. The ground-state density therefore determines the external potential up to an additive constant.

The ground-state density therefore contains enough information to determine the Hamiltonian, $\hat{\mathrm{H}}$, and the ground-state energy, E_0, which can then be expressed as a functional of the density,

$$E_0[n_0] = \int n_0(\mathbf{r}) v_{\text{ext}}(\mathbf{r}) \, \mathrm{d}\mathbf{r} + F[n_0]. \tag{23}$$

The integral contains the contributions from the interaction between the electrons with the external potential, while $F[n]$, contains the universal terms

$$F[n] = T[n] + V_{\text{ee}}[n], \tag{24}$$

describing the kinetic energy, $T[n]$, and electron–electron interaction energy, $V_{\text{ee}}[n]$ [17].

The second Hohenberg–Kohn theorem confirms that the variational principle can also be applied to the density, $n(r)$, similar to the wavefunction like in the HF approximation. This means that for any physically admissible trial function density $\tilde{n}(r)$, the corresponding energy satisfies

$$E_0[n_0] \leq E[\tilde{n}], \tag{25}$$

The ground-state density can therefore be reached by iteratively minimizing the energy functional with respect to the electron density [17].

The Hohenberg–Kohn theorems establish the existence of an exact ground-state energy functional, but do not provide its explicit form. The Kohn–Sham formulation provides a practical approach to evaluating this functional [17].

2.2.3 Kohn-Sham Density Functional Theory

Although the Hohenberg-Kohn theorems show that the ground-state energy is a functional of the electron density, they do not conclude on the explicit form of this functional. In particular, the kinetic energy of the interacting electrons remains difficult to express directly in terms of the density. Kohn and Sham addressed this problem by introducing an auxiliary system of non-interacting electrons that is constructed to reproduce the same ground-state density as the interacting system [25].

The total energy is written as

$$E\left[n(r)\right] = T_s\left[n(r)\right] + \int v_{\text{ext}}(r)n(r)\mathrm{d}r + E_{\text{H}}\left[n(r)\right] + E_{xc}\left[n(r)\right], \tag{26}$$

where $T_s\left[n(r)\right]$ is the kinetic energy of the non-interacting reference system, $E_{\text{H}}\left[n(r)\right]$ is the classical electrostatic Hartree energy, and the $E_{xc}\left[n(r)\right]$ is the exchange-correlation energy. The Hartree contribution is given by

$$E_{\text{H}}\left[n(r)\right] = \frac{1}{2}\iint \frac{n(r)n(r')}{|r-r'|}\mathrm{d}r\mathrm{d}r'. \tag{27}$$

The exchange-correlation functional contains all many-body contributions not explicitly included in the remaining terms. This includes the difference between the true interacting kinetic energy and the non-interacting kinetic energy, as well as the non-classical part of the electron-electron interaction.

The non-interacting kinetic energy can be evaluated explicitly from a set of single-electron Kohn-Sham orbitals ψ_i,

$$T_s = -\frac{1}{2}\sum_i f_i \int \psi_i^*(r)\nabla^2\psi_i(r)\mathrm{d}r, \tag{28}$$

where f_i denotes the occupation of orbital i. This is, however, only an approximation to the kinetic energy of the true many-body system.

Minimization of the total energy with respect to the Kohn-Sham orbitals leads to the Kohn-Sham equations,

$$\left[-\frac{1}{2}\nabla^2 + v_{\text{eff}}(r)\right]\psi_i(r) = \varepsilon_i\psi_i(r), \tag{29}$$

where the effective potential is

$$v_{\text{eff}}(r) = v_{\text{ext}}(r) + v_{\text{H}}(r) + v_{xc}(r). \tag{30}$$

Here, the Hartree potential is

$$v_{\text{H}}(r) = \int \frac{n(r')}{|r-r'|}\mathrm{d}r', \tag{31}$$

while the exchange-correlation potential is obtained from the functional derivative of the exchange-correlation energy,

$$v_{xc}(r) = \frac{\delta E_{xc}\left[n(r)\right]}{\delta n(r)}. \tag{32}$$

From the occupied Kohn-Sham orbitals the electron density is acquired

$$n(r) = \sum_i f_i\left|\psi_i(r)\right|^2. \tag{33}$$

Since the effective potential is dependent on the electron density, while the density itself depends on the solutions of the Kohn-Sham equations, the equations must be solved self-consistently. An initial trial density is used to construct the effective potential. Solving the Kohn–Sham equations gives orbitals from which an updated density is calculated. This procedure is repeated until the density and total energy are converged.

The Kohn–Sham formulation is in principle exact, but in practice, the exchange–correlation functional is unknown and must be approximated, making its choice one of the central approximations in DFT calculations.

For systems with unpaired electrons, the Kohn–Sham formulation can be extended to separate spin-up and spin-down densities, with $n(\mathbf{r}) = n_{\uparrow}(\mathbf{r}) + n_{\downarrow}(\mathbf{r})$. The exchange–correlation energy then depends on both spin densities, giving spin-dependent effective potentials [26]. This extension allows local magnetic moments to be described, which can be relevant to transition-metal impurities in copper.

2.2.4 Exchange-Correlation Approximations

Practical Kohn–Sham calculations require an approximation for the exchange–correlation functional. Different approximations use different information about the electronic structure, and their accuracy depends on the system and property being studied.

The local density approximation (LDA) assigns each point the exchange–correlation energy per electron of a homogeneous electron gas with density equal to the local value $n(\mathbf{r})$,

$$E_{xc}^{\mathrm{LDA}}[n] = \int n(r)\varepsilon_{xc}(n(r))\mathrm{d}r, \tag{34}$$

where $\varepsilon_{xc}(n(r))$ is the exchange-correlation energy per electron of a homogeneous electron gas with density n [25].

The LDA is exact for the homogeneous electron gas when its exact exchange–correlation energy is used. It provides a useful approximation for many solids, although it commonly overestimates binding and underestimates equilibrium bond lengths. These tendencies are not universal and must be assessed for the property of interest.

The generalized gradient approximation (GGA) contains the spatial variation of the density. The exchange-correlation energy can therefore be written in the general form

$$E_{xc}^{\mathrm{GGA}}[n] = \int f(n(r), \nabla n(r))\mathrm{d}r. \tag{35}$$

By including the density gradient $\nabla n(r)$, GGA functionals can account for variations in the electron density that are neglected within LDA. This is particularly important in molecules, surfaces, and adsorption systems, where the density can vary substantially over short distances.

The Perdew–Burke–Ernzerhof (PBE) functional is a widely used GGA, which was constructed to satisfy a number of known physical constraints without extensive empirical fitting [27]. PBE generally improves molecular geometries and binding properties compared with LDA, although it may still predict adsorption energies that are too strong for some adsorbates on transition-metal surfaces.

The revised PBE (RPBE) functional adjusts the exchange enhancement factor while retaining PBE correlation. It was developed to improve molecular adsorption energetics and generally

predicts weaker adsorption than PBE for the systems considered in its original assessment [28]. This makes it relevant to surface chemistry, although it does not guarantee accurate adsorption energies or site preferences for every system.

Local and semilocal functionals do not reproduce the correct long-range dispersion interaction between separated, non-overlapping electron distributions. Describing this contribution requires an additional dispersion treatment or a nonlocal correlation functional [29]. The following section discusses these approaches and the BEEF-vdW functional used in this thesis.

2.3 Dispersion Interactions

Long-range dispersion is an important contribution to adsorption that is not captured by local and semilocal exchange–correlation approximations. Its treatment requires accounting for electronic correlation between spatially separated regions.

2.3.1 Origin of Dispersion Interactions

Dispersion interactions originate from correlated quantum-mechanical fluctuations in the electronic distribution. Even atoms and molecules with no permanent dipole moment, exhibit fluctuations that can couple to those in a neighboring species. These correlated fluctuations lower the energy of the combined system, giving rise to an attractive interaction known as London dispersion [30].

For two neutral, isotropic atoms or molecules separated by a sufficiently large distance, R, but within the non-retarded regime, the leading contribution to the dispersion energy is

$$E_{\mathrm{disp}}(R) \approx -\frac{C_6^{AB}}{R^6}, \tag{36}$$

where C_6^{AB} is a positive dispersion coefficient determined by the frequency-dependent polarizabilities of the interacting species A and B [30]. The negative sign indicates that the interaction is entirely attractive. Higher-order contributions arise from interactions involving fluctuating quadrupoles and other multipoles, and decay more rapidly with increasing separation.

Dispersion is a consequence of electron correlation and does not require overlap between the electron densities of the interacting species. It can therefore remain significant at separations where orbital overlap and chemical bonding are negligible. Local and semi-local exchange-correlation functionals cannot reproduce this asymptotic interaction, since they do not describe the coupling of fluctuations between spatially separated, non-overlapping electron distributions [29, 31]

Although dispersion is often associated with weakly bound systems, it also contributes to the interaction energy of molecules that are chemically bonded to a surface. In adsorption systems, dispersion can arise both between an adsorbate and the substrate and between neighboring adsorbates. Its contribution must therefore be considered alongside chemical bonding when evaluating adsorption energies and comparing different adsorbate configurations.

2.3.2 Non-local van der Waals Density Functionals

The description of dispersion interactions within DFT requires a treatment of electron correlation that couples spatially separated regions of the electron density. Non-local van der Waals density functionals introduce this coupling through an explicit non-local correlation contribution to the exchange-correlation energy. In the original van der Waals density functional (vdW-DF) proposed by Dion et al. [29], the functional takes the form

$$E_{\mathrm{xc}}[n] = E_{\mathrm{x}}^{\mathrm{GGA}}[n] + E_{\mathrm{c}}^{\mathrm{LDA}}[n] + E_{\mathrm{c}}^{\mathrm{nl}}[n], \tag{37}$$

where $E_{\mathrm{x}}^{\mathrm{GGA}}$ is the semi-local exchange energy, $E_{\mathrm{c}}^{\mathrm{LDA}}$ describes local correlation, and $E_{\mathrm{c}}^{\mathrm{nl}}$ introduces the non-local correlation needed to account for dispersion. The latter contribution is expressed as

$$E_{\mathrm{c}}^{\mathrm{nl}}[n] = \frac{1}{2}\iint n(\mathbf{r})\phi(\mathbf{r},\mathbf{r}')n(\mathbf{r}')\mathrm{d}\mathbf{r}\mathrm{d}\mathbf{r}', \tag{38}$$

where $\phi(\mathbf{r},\mathbf{r}')$ is a kernel that depends on the separation between the two positions and on the electron density and its gradient in their vicinity. The double integral couples distinct regions of the density, including regions with negligible overlap [29].

The non-local correlation energy is a functional of the electron density and therefore also contributes to the effective potential in the Kohn-Sham equations through its functional derivative,

$$v_{\mathrm{c}}^{\mathrm{nl}}(\mathbf{r}) = \frac{\delta E_{\mathrm{c}}^{\mathrm{nl}}[n]}{\delta n(\mathbf{r})}. \tag{39}$$

This allows non-local correlation to be included self-consistently in the electronic-structure calculation. Its contribution to the atomic forces can consequently be included during geometry optimization, allowing dispersion to influence both the calculated energies and equilibrium structures [31].

Different members of the van der Waals density-functional family employ different exchange approximations and formulations of the non-local correlation kernel. Their predictions therefore depend on the balance between these contributions, particularly at separations near equilibrium where the electron densities overlap. For example, the subsequent vdW-DF2 functional modifies both the exchange description and the construction of the non-local kernel to improve the treatment of non-covalently bound systems [32].

2.3.3 BEEF-vdW

The Bayesian error estimation functional with van der Waals correlation (BEEF-vdW) combines a fitted GGA exchange expansion with local, semilocal and nonlocal correlation [33],

$$E_{\mathrm{xc}} = \sum_m a_m E_{\mathrm{x},m}^{\mathrm{GGA}} + \alpha_c E_{\mathrm{c}}^{\mathrm{LDA}} + (1-\alpha_c)E_{\mathrm{c}}^{\mathrm{PBE}} + E_{\mathrm{c}}^{\mathrm{nl}}. \tag{40}$$

where the coefficients a_m determine the exchange expansion and α_c controls the mixing of LDA and PBE correlation. The parameters were optimized against reference data covering molecular energetics, non-covalent interactions, bulk properties, and adsorption energies, aiming for a balanced description of different bonding environments. The non-local correlation contribution employs the vdW-DF2 kernel described in the preceding subsection. BEEF-vdW therefore includes dispersion within the exchange-correlation functional and can be applied self-consistently to calculate energies and equilibrium geometries [33].

2.4 Periodic Systems and Plane-Wave DFT

The Kohn-Sham equations provide a practical framework for determining the electronic structure of interacting many-electron systems, but their numerical solution still requires a representation of the Kohn-Sham orbitals and the simulation cell. For crystalline solids, the periodic arrangement of the atoms can be exploited to reduce the description of an effectively infinite system to a finite unit cell. This forms the basis for the plane-wave implementations of DFT commonly used for calculations of bulk materials and surfaces.

2.4.1 Periodic Boundary Conditions

An ideal crystal consists of a repeating arrangement of atoms that extends throughout space. This translational symmetry means that the atomic arrangement is unchanged under translation by a lattice vector $\mathbf{R}$, and allows the system to be described using a unit cell, whose repetition generates the crystal. Any lattice translation vector can be expressed as

$$\mathbf{R} = n_1\mathbf{a}_1 + n_2\mathbf{a}_2 + n_3\mathbf{a}_3, \tag{41}$$

where $\mathbf{a}_1$, $\mathbf{a}_2$, and $\mathbf{a}_3$ are the lattice vectors defining the unit cell, and n_1, n_2, and n_3 are integers. Periodic boundary conditions reproduce the atomic configuration in every translated cell, allowing the properties of an extended crystal to be calculated without introducing external boundaries.

Because the positions of the nuclei repeat periodically, the external potential experienced by the electrons has the same periodicity

$$v_{\text{ext}}(\mathbf{r}+\mathbf{R}) = v_{\text{ext}}(\mathbf{r}). \tag{42}$$

Similarly, for an electronic state that preserves the periodicity of the chosen cell, the electron density satisfies

$$n(\mathbf{r}+\mathbf{R}) = n(\mathbf{r}). \tag{43}$$

The corresponding effective Kohn-Sham potential is also periodic,

$$v_{\text{eff}}(\mathbf{r}+\mathbf{R}) = v_{\text{eff}}(\mathbf{r}). \tag{44}$$

The orbitals transform under lattice translations as described by Bloch's theorem.

2.4.2 Bloch's Theorem

The periodicity of the crystal and effective Kohn-Sham potential imposes a particular structure on the electronic eigenstates. Bloch's theorem states that the orbitals can be chosen in the form[34]

$$\psi_{n\mathbf{k}}(\mathbf{r}) = e^{i\mathbf{k}\cdot\mathbf{r}}u_{n\mathbf{k}}(\mathbf{r}), \tag{45}$$

where n is the band index, $\mathbf{k}$ is a wave vector, and $u_{n\mathbf{k}}(\mathbf{r})$ is a function with the periodicity of the lattice,

$$u_{n\mathbf{k}}(\mathbf{r}+\mathbf{R}) = u_{n\mathbf{k}}(\mathbf{r}). \tag{46}$$

Each orbital is therefore expressed as a plane wave multiplied by a lattice-periodic function. Under translation by a lattice vector, the orbital satisfies

$$\psi_{n\mathbf{k}}(\mathbf{r}+\mathbf{R}) = e^{i\mathbf{k}\cdot\mathbf{R}}\psi_{n\mathbf{k}}(\mathbf{r}). \tag{47}$$

Thus, although the orbital itself need not be periodic, its probability density is unchanged by a lattice translation.

Substituting the Bloch form into the Kohn-Sham equations gives an equation for the periodic function,

$$\left[\frac{1}{2m_{\mathrm{e}}}\left(-i\hbar\nabla+\hbar\mathbf{k}\right)^2+v_{\mathrm{eff}}(\mathbf{r})\right]u_{n\mathbf{k}}(\mathbf{r})=\varepsilon_{n\mathbf{k}}u_{n\mathbf{k}}(\mathbf{r}), \tag{48}$$

where $\varepsilon_{n\mathbf{k}}$ is the energy eigenvalue associated with band n and wave vector $\mathbf{k}$. Bloch's theorem therefore transforms the electronic-structure problem of an extended crystal into a set of equations for periodic functions within a single unit cell, one set for each $\mathbf{k}$.

The dependence of the eigenvalues $\varepsilon_{n\mathbf{k}}$ on the wave vector $\mathbf{k}$ defines the electronic band structure. The distinct wave vectors needed to describe these states are identified using the reciprocal lattice.

2.4.3 Reciprocal Space

The translational symmetry of a crystal can be described in reciprocal space, where vectors have dimensions of inverse length. For a lattice defined by the real-space vectors $\mathbf{a}_1$, $\mathbf{a}_2$, and $\mathbf{a}_3$, the reciprocal lattice vectors $\mathbf{b}_1$, $\mathbf{b}_2$, and $\mathbf{b}_3$ are defined by

$$\mathbf{a}_i\cdot\mathbf{b}_j=2\pi\delta_{ij}, \tag{49}$$

where δ_{ij} is the Kronecker delta. These vectors can be constructed as

$$\mathbf{b}_1=2\pi\frac{\mathbf{a}_2\times\mathbf{a}_3}{\mathbf{a}_1\cdot(\mathbf{a}_2\times\mathbf{a}_3)}, \tag{50}$$

with $\mathbf{b}_2$ and $\mathbf{b}_3$ obtained by cyclic permutation of the indices. Any reciprocal lattice vector can then be written as

$$\mathbf{G}=m_1\mathbf{b}_1+m_2\mathbf{b}_2+m_3\mathbf{b}_3, \tag{51}$$

where m_1, m_2, and m_3 are integers.

For any real-space lattice translation $\mathbf{R}$, these definitions imply

$$\mathbf{G}\cdot\mathbf{R}=2\pi(m_1n_1+m_2n_2+m_3n_3), \tag{52}$$

It follows that plane waves with reciprocal lattice wave vectors have the periodicity of the crystal and can be used to expand lattice-periodic functions.

While $\mathbf{G}$ labels the discrete reciprocal lattice vectors, the Bloch wave vector $\mathbf{k}$ labels the translational phase of an electronic state. Wave vectors $\mathbf{k}$ and $\mathbf{k}+\mathbf{G}$ produce the same phase under lattice translations, so only one primitive cell of reciprocal space is needed to represent the distinct values of $\mathbf{k}$. The conventional choice is the first Brillouin zone, which consists of the points closer to the reciprocal lattice origin than to any other reciprocal lattice point. Its center, $\mathbf{k}=\mathbf{0}$, is called the Γ point.

The volume of the first Brillouin zone is inversely related to the real-space unit-cell volume by

$$\Omega_{\mathrm{BZ}}=\frac{(2\pi)^3}{\Omega}. \tag{53}$$

Increasing the real-space cell volume therefore decreases the Brillouin-zone volume. Integrals over this zone are evaluated numerically using the sampling methods described below.

2.4.4 Brillouin-Zone Sampling

In a periodic solid, quantities such as the electron density and total energy involve contributions from electronic states throughout the first Brillouin zone. For an infinite crystal, the Bloch wave vector $\mathbf{k}$ varies continuously, and these contributions are evaluated through integrals over reciprocal space. In practical calculations, the integrals are estimated using a weighted sum over a finite set of $\mathbf{k}$ points,

$$\frac{1}{\Omega_{\mathrm{BZ}}}\int_{\mathrm{BZ}} A(\mathbf{k})\,\mathrm{d}^3\mathbf{k} \approx \sum_{i=1}^{N_{\mathbf{k}}} w_i A(\mathbf{k}_i), \tag{54}$$

where $A(\mathbf{k})$ represents a wave-vector-dependent quantity, $N_{\mathbf{k}}$ is the number of sampled points, and the weights satisfy

$$\sum_{i=1}^{N_{\mathbf{k}}} w_i = 1. \tag{55}$$

How accurate this approximation is depends on how densely the Brillouin zone is sampled and on how quickly the integrand changes across it.

A common approach is to distribute the sampling points on a regular grid along the reciprocal lattice vectors. In the Monkhorst-Pack scheme, the fractional coordinate along each reciprocal lattice direction is

$$q_{j_\alpha}^{(\alpha)} = \frac{2j_\alpha - N_\alpha - 1}{2N_\alpha}, \qquad j_\alpha = 1,\ldots,N_\alpha, \qquad \alpha = 1,2,3. \tag{56}$$

where N_α is the number of grid points along the reciprocal lattice direction, and j_α indexes the points along that direction. The three-dimensional sampling points are constructed as

$$\mathbf{k}_{j_1 j_2 j_3} = \sum_{\alpha=1}^{3} q_{j_\alpha}^{(\alpha)} \mathbf{b}_\alpha. \tag{57}$$

where $\mathbf{b}_\alpha$ are the reciprocal lattice vectors [35].

An alternative is a Γ-centered grid, which includes the reciprocal-space origin. For identical grid dimensions, the two constructions coincide modulo reciprocal lattice translations when all dimensions are odd, but differ by half a grid spacing along directions with an even number of points. When the relevant symmetries are present, equivalent points can be grouped together and their weights combined, reducing the number of distinct $\mathbf{k}$ points that must be evaluated.

Brillouin-zone sampling requires particular care for metals, where electronic occupations change abruptly at the Fermi energy at zero electronic temperature. Smearing can improve numerical convergence by smoothing the occupation change. The different smearing methods are discussed in a later section.

The sampling grid must be converged for the quantities of interest, particularly adsorption energies and relative energies between configurations. Larger real-space dimensions correspond to shorter reciprocal lattice vectors and generally require fewer sampling points along those directions. For surface slabs separated by sufficient vacuum, a single point is usually adequate perpendicular to the surface, while a denser grid is needed within the surface plane.

2.4.5 Plane-Wave Basis Sets

Bloch's theorem expresses each Kohn-Sham orbital as a plane wave multiplied by a lattice-periodic function. The periodic part can be expanded in a Fourier series over reciprocal lattice vectors, giving

$$u_{n\mathbf{k}}(\mathbf{r}) = \frac{1}{\sqrt{\Omega}} \sum_{\mathbf{G}} c_{n\mathbf{k}}(\mathbf{G}) e^{i\mathbf{G}\cdot\mathbf{r}}, \tag{58}$$

where Ω is the unit-cell volume and $c_{n\mathbf{k}}(\mathbf{G})$ are the expansion coefficients. Substituting this expression into the Bloch form gives the plane-wave expansion of the orbital:

$$\psi_{n\mathbf{k}}(\mathbf{r}) = \frac{1}{\sqrt{\Omega}} \sum_{\mathbf{G}} c_{n\mathbf{k}}(\mathbf{G}) e^{i(\mathbf{k}+\mathbf{G})\cdot\mathbf{r}}. \tag{59}$$

Here, the normalization factor corresponds to orbitals normalized within the unit cell. For each sampled wave vector $\mathbf{k}$, the electronic-structure calculation determines the coefficients $c_{n\mathbf{k}}(\mathbf{G})$ [36].

At a fixed $\mathbf{k}$, the plane-wave basis functions are orthonormal over the unit cell and are eigenfunctions of the kinetic-energy operator. Consequently, the kinetic energy contribution is diagonal in this representation,

$$T_{\mathbf{G},\mathbf{G}'}(\mathbf{k}) = \frac{\hbar^2}{2m_\mathrm{e}} |\mathbf{k}+\mathbf{G}|^2 \, \delta_{\mathbf{G},\mathbf{G}'}, \tag{60}$$

where m_e is the electron mass and $\delta_{\mathbf{G},\mathbf{G}'}$ is the Kronecker delta. The local potential is conveniently applied through multiplication in real space, with fast Fourier transforms used to move between real-space and reciprocal-space representations. This combination enables efficient application of the Kohn-Sham Hamiltonian [36, 37].

2.4.6 Energy Cutoff and Basis-Set Convergence

The plane-wave expansion formally contains infinitely many reciprocal lattice vectors. To obtain a finite basis for numerical calculations, only plane waves with kinetic energies below a specified cutoff are retained. For each Bloch wave vector, the included reciprocal lattice vectors satisfy

$$\frac{\hbar^2}{2m_\mathrm{e}} |\mathbf{k}+\mathbf{G}|^2 \leq E_\mathrm{cut}, \tag{61}$$

where E_cut is the kinetic-energy cutoff. Increasing this cutoff introduces plane waves with shorter wavelengths, allowing finer spatial variations in the orbitals to be represented. The cutoff therefore provides a single parameter for systematically improving the completeness of the plane-wave basis[36].

The size of the basis set scales with the cutoff energy and with the volume of the simulation cell. Approximating the number of reciprocal lattice points within the cutoff sphere gives

$$N_\mathrm{PW} \approx \frac{\Omega}{6\pi^2} \left(\frac{2m_\mathrm{e}E_\mathrm{cut}}{\hbar^2} \right)^{3/2}, \tag{62}$$

where N_PW is the number of plane waves at a given $\mathbf{k}$ point and Ω is the unit-cell volume. Thus, increasing the cutoff enlarges the basis approximately in proportion to its three-halves power.

Increasing the cell volume also enlarges the basis, even when the additional volume consists of vacuum.

Basis-set convergence is assessed by repeating calculations at progressively higher cutoffs until the quantities of interest change by less than a chosen tolerance. For adsorption studies, this requires examining adsorption energies and relative energies between configurations, since convergence of individual total energies does not directly establish the accuracy of their differences. Forces must also be sufficiently converged when optimizing structures or locating transition states.

The required cutoff depends on the pseudopotentials or projector augmented-wave (PAW) datasets used, since these determine the spatial variation of the auxiliary orbitals [38, 39]. Calculations entering the same energy difference should use consistent datasets and a common cutoff sufficient for all species involved. Other numerical settings, including Brillouin-zone sampling and electronic convergence thresholds, must be sufficiently accurate to distinguish basis-set errors from other sources of numerical error.

2.5 Projector Augmented-Wave Method

The efficient representation of electronic orbitals in a plane-wave basis becomes difficult near atomic nuclei, where the attractive nuclear potential and orthogonality to core states produce rapid spatial variations in the valence orbitals. The PAW method, introduced by Blöchl, addresses this difficulty by expressing the all-electron valence orbitals through a transformation of smooth auxiliary orbitals. The auxiliary orbitals can be represented efficiently using plane waves, while the detailed behavior near the nuclei is recovered through atom-centered corrections [38].

The all-electron orbital is related to its auxiliary counterpart by a linear transformation,

$$|\psi_{n\mathbf{k}}\rangle = \hat{\mathscr{T}}\,|\tilde{\psi}_{n\mathbf{k}}\rangle\,, \tag{63}$$

where the tilde denotes a smooth auxiliary quantity. The transformation differs from the identity only within augmentation regions surrounding the atoms. Within each region, the orbital is represented using all-electron partial waves and corresponding smooth partial waves. These partial waves coincide outside the augmentation region, so their difference provides a localized correction. The transformation operator is written as

$$\hat{\mathscr{T}} = \hat{1} + \sum_a \sum_i \left(|\phi_i^a\rangle - |\tilde{\phi}_i^a\rangle\right)\langle \tilde{p}_i^a|\,, \tag{64}$$

where a labels the atoms and i labels the partial-wave channels, including their angular-momentum and reference-energy indices. The functions ϕ_i^a and $\tilde{\phi}_i^a$ are the all-electron and smooth partial waves, respectively, and $\tilde{p}_i^a$ are localized projector functions. The projectors are constructed to satisfy the duality relation

$$\langle \tilde{p}_i^a|\tilde{\phi}_j^a\rangle = \delta_{ij}. \tag{65}$$

Projecting an auxiliary orbital onto these functions determines the coefficients of its local partial-wave expansion. The transformation then subtracts the smooth expansion and adds the corresponding all-electron expansion. Outside the augmentation regions, the auxiliary and reconstructed orbitals coincide [38, 40].

The electron density is reconstructed in a similar manner, combining a smooth density with atom-centered corrections,

$$n(\mathbf{r}) = \tilde{n}(\mathbf{r}) + \sum_a \left[n^a(\mathbf{r}) - \tilde{n}^a(\mathbf{r}) \right]. \tag{66}$$

Here, $\tilde{n}$ is the smooth density, while n^a and $\tilde{n}^a$ are the all-electron and smooth on-site densities constructed from the partial waves, with core contributions included consistently. Subtracting the smooth on-site density avoids counting its contribution twice. A corresponding decomposition is used to evaluate the total energy. Localized compensation charges are introduced in the electrostatic treatment to reproduce the appropriate multipole moments and allow the smooth and on-site contributions to be combined consistently [38, 39].

Because the transformation is not generally unitary, the auxiliary orbitals satisfy a generalized Kohn-Sham eigenvalue equation,

$$\hat{\mathscr{T}}^\dagger \hat{H}_{\mathrm{KS}} \hat{\mathscr{T}} \, |\tilde{\psi}_{n\mathbf{k}}\rangle = \varepsilon_{n\mathbf{k}} \hat{\mathscr{T}}^\dagger \hat{\mathscr{T}} \, |\tilde{\psi}_{n\mathbf{k}}\rangle . \tag{67}$$

The operator $\hat{\mathscr{T}}^\dagger \hat{\mathscr{T}}$ defines the overlap metric that ensures orthonormality of the reconstructed all-electron orbitals [40].

In practical PAW calculations, the core states are commonly held fixed at their atomic reference configurations, while the valence states are optimized self-consistently. This frozen-core approximation reduces the computational effort but requires an appropriate division between core and valence states. Semi-core states may need to be treated explicitly when they contribute to bonding or respond appreciably to the chemical environment. The local expansion also contains a finite number of partial waves and projectors, so its accuracy depends on the construction and transferability of the PAW dataset. The formulation of Kresse and Joubert provides the basis for the PAW implementation used in Vienna Ab Initio Simulation Package (VASP), combining an efficient plane-wave representation with reconstruction of the electronic structure near the atomic cores [39].

2.6 Metallic Systems and Electronic Occupations

The evaluation of Brillouin-zone integrals, especially in metals, is complicated by the abrupt change in electronic occupation at the Fermi energy. At zero electronic temperature, the occupation of an individual spin state is described by a step function,

$$f_{n\mathbf{k}} = \Theta(\varepsilon_{\mathrm{F}} - \varepsilon_{n\mathbf{k}}), \tag{68}$$

where Θ is the Heaviside function and ε_{F} is the Fermi energy. With a finite set of k points, small changes in the eigenvalues near the Fermi energy can cause abrupt changes in occupation, slowing electronic convergence and making energies and forces sensitive to the sampling grid. Smearing methods replace the step function with a smooth approximation characterized by an energy width σ.

Different smearing methods have different interpretations. Fermi–Dirac smearing describes electronic occupations at a finite temperature, with $\sigma = k_{\mathrm{B}} T_{\mathrm{e}}$ [41]. Gaussian and Methfessel–Paxton smearing instead provide numerical approximations designed to facilitate integration. Their widths should therefore be treated as numerical parameters rather than physical temperatures.

The Methfessel–Paxton method constructs higher-order approximations to the occupation step by adding Hermite-polynomial corrections to Gaussian smearing. Defining the dimensionless energy variable

$$x = \frac{\varepsilon - \mu}{\sigma}, \tag{69}$$

where μ is the chemical potential, the occupation function of order N is

$$f_N(x) = \frac{1}{2}\operatorname{erfc}(x) + e^{-x^2} \sum_{m=1}^{N} A_m H_{2m-1}(x), \tag{70}$$

with coefficients

$$A_m = \frac{(-1)^m}{4^m m! \sqrt{\pi}}. \tag{71}$$

Here, erfc is the complementary error function and H_j denotes the *physicists' Hermite polynomial* of order j. The zeroth-order expression reduces to Gaussian smearing. The higher-order terms cancel successive low-order moments of the associated broadening kernel, reducing the integration error for sufficiently smooth energy-dependent quantities [42].

For first-order Methfessel–Paxton smearing, using $H_1(x) = 2x$, the occupation function becomes

$$f_1(x) = \frac{1}{2}\operatorname{erfc}(x) - \frac{x}{2\sqrt{\pi}} e^{-x^2}. \tag{72}$$

The correction improves the approximation to the sharp occupation step but introduces non-monotonic behavior. Consequently, resulting occupation weights can lie slightly below zero or above one and should not be interpreted as physical occupation probabilities. They serve as numerical integration weights.

Smearing also affects the energy functional used during electronic minimization. A generalized free-energy functional, containing a smearing-dependent correction, provides the variational quantity from which consistent forces are obtained [43]. For Fermi–Dirac occupations, this correction has the physical interpretation of electronic entropy. For Methfessel–Paxton smearing, it is a mathematical correction associated with the integration scheme. The generalized free energy and the estimated zero-smearing energy must therefore be distinguished, particularly when interpreting energies from geometry optimizations [42].

The smearing width must be converged together with the k-point grid. A small width requires dense sampling near the Fermi surface, whereas excessive broadening can alter the energies and forces. For the metallic copper-based systems considered here, Methfessel–Paxton smearing is relevant to structural relaxation, but convergence must be established for adsorption energies, relative energies, and forces.

2.7 Surface Models and Energetics

Periodic DFT calculations of surface processes require atomic models that represent the local environments under investigation. A crystalline surface is commonly modeled by a slab containing a chosen number of atomic layers, with periodic repetition parallel to the surface and separation between neighboring slabs. The slab geometry and lateral dimensions determine which surface features, adsorbate arrangements, and impurity concentrations can be represented.

For the copper-based systems considered here, these models provide a framework for comparing adsorption on terraces, at steps, and near substitutional transition-metal impurities. Their relative stability is evaluated using energy differences with consistent reference states [44]. Vibrational and thermal corrections can then extend the static energies to finite-temperature thermodynamic quantities.

2.7.1 Periodic Slab Representation

A slab contains a finite number of atomic layers repeated parallel to the surface and separated from neighboring slabs in the perpendicular direction. Vacuum calculations retain three-dimensional periodicity but approximate a surface extended in two dimensions. The lateral lattice parameter is normally taken from a consistent bulk calculation and held fixed during surface relaxation. Lower layers may be constrained to bulk-like positions, while the upper layers and adsorbates relax.

Slab thickness, the number of relaxed layers, and the separation between repeated slabs must be converged independently. Thin metallic slabs can exhibit non-monotonic convergence, and adsorption energies, work functions and structural parameters need not converge at the same rate [45]. Vacuum separation is measured between the outermost atoms of neighboring images, including adsorbates.

For a neutral asymmetric slab, a perpendicular dipole generates an artificial field under three-dimensional periodic boundary conditions. A dipole correction removes the leading spurious field and improves convergence with vacuum separation [46] Charged electrochemical interfaces additionally require appropriate countercharge and electrolyte boundary conditions, as discussed in Section 2.9.

2.7.2 Terraces, Steps, and Substitutional Impurities

Copper has a face-centered cubic (fcc) structure. Ideal unreconstructed Cu(111) and Cu(100) terraces have triangular and square surface arrangements, with nine and eight nearest neighbors per surface atom, respectively. Steps introduce lower-coordination step atoms and additional inequivalent adsorption environments. On fcc(111), closed-packed monoatomic A- and B-type steps expose local {100} and {111} microfacets, respectively [47].

A periodic stepped model can be constructed from a vicinal surface or by adding a stripe of atoms to a low-index slab. The terrace width, stripe width, and separation between repeated stripes control interactions between steps. The steps in one cell are not necessarily equivalent, so their geometry must be identified explicitly. An isolated-step approximation requires convergence with step separation.

Replacing a Cu atom introduces a substitutional impurity. One impurity per cell represents a periodic array, rather than an automatically isolated atom. Comparing terrace, step, and subsurface positions is most direct within models of identical composition. Relaxation is essential: adsorption can alter the impurity coordination and displace it substantially from its initial lattice position.

2.7.3 Adsorption and Relative Energies

Common starting sites include top, bridge, and hollow positions. Cu(100) has fourfold hollows, whereas Cu(111) has threefold fcc and hcp hollows. The hcp hollow lies above a second-layer atom and the fcc hollow above a third-layer atom. CO generally binds through carbon, but its preferred site, height and orientation must be determined by relaxation and comparison of competing configurations. Calculated site preferences can depend on the exchange–correlation approximation [48].

Energy differences quantify stability relative to specified reference states. Here, E_X denotes the DFT total energy of configuration X. All terms in an energy difference require consistent functionals, atomic datasets, and converged numerical settings. For a molecule A adsorbing on surface S, the binding energy is

$$E_b = E_S + E_A - E_{S+A}, \qquad \Delta E_{\text{ads}} = -E_b. \tag{73}$$

Positive binding energy and negative adsorption energy therefore indicate favorable adsorption relative to the specified isolated molecule. Writing $E_n = E_{S+nCO}$, the differential binding energy of multiple CO adsorption is characterized by

$$E_{b,n} = E_{n-1} + E_{\text{CO}} - E_n \tag{74}$$

2.7.4 Vibrational Analysis and Thermochemical Corrections

Within the harmonic approximation, the potential near a stationary configuration is expanded to second order,

$$E(\mathbf{R}_0 + \mathbf{u}) \approx E(\mathbf{R}_0) + \frac{1}{2}\mathbf{u}^{\mathrm{T}}\mathbf{H}\mathbf{u}, \tag{75}$$

where $\mathbf{u}$ is a displacement from the stationary configuration $\mathbf{R}_0$, and $\mathbf{H}$ is the Hessian matrix. The linear term vanishes because the energy gradient is zero. The Hessian can be obtained from the central differences of the forces

$$H_{ij} = \frac{\partial^2 E}{\partial R_i \partial R_j} \approx -\frac{F_i(\mathbf{R}_0 + \delta\mathbf{e}_j) - F_i(\mathbf{R}_0 - \delta\mathbf{e}_j)}{2\delta} \tag{76}$$

where R_i and R_j denote individual Cartesian coordinates, $\mathbf{e}_j$ is a unit vector along coordinate j, and δ is the displacement amplitude. At a non-degenerate local minimum, the Hessian is positive definite after constrained coordinates and symmetry-related zero modes have been excluded. Such minima represent locally stable configurations, including different adsorption sites or molecular arrangements on a surface [49]. The vibrational frequencies follow from diagonalization of the mass-weighted Hessian,

$$D_{ij} = \frac{H_{ij}}{\sqrt{m_i m_j}}, \qquad \mathbf{D}\mathbf{e}_\alpha = \omega_\alpha^2 \mathbf{e}_\alpha, \tag{77}$$

where m_i is the mass associated with Cartesian coordinate i, $\mathbf{e}_\alpha$ is a normal-mode eigenvector, and ω_α is an angular frequency. At the initial minimum, the vibrational eigenvalues are positive after removing any symmetry-related zero modes.

For stable harmonic modes, the vibrational free energy is

$$F_{\text{vib}}(T) = \sum_\alpha \left[\frac{h\nu_\alpha}{2} + k_{\text{B}} T \ln\left(1 - e^{-h\nu_\alpha/(k_{\text{B}}T)}\right) \right]. \tag{78}$$

The first term gives the zero-point energy. A fixed-cell surface free energy is approximated as $F_X(T) \approx E_X + F_{\mathrm{vib},X}(T)$, with surface pV contributions usually negligible. Gas-phase references also require translational and rotational contributions. For an ideal molecular gas,

$$\mu_A(T,p) = \mu_A^\circ(T) + k_\mathrm{B} T \ln(p/p^\circ), \tag{79}$$

where μ_A° includes the static molecular energy and its standard-state thermochemical corrections. The corresponding adsorption free energy is

$$\Delta G_\mathrm{ads}(T,p) \approx F_{S+A}(T) - F_s(T) - \mu_A(T,p). \tag{80}$$

Such combinations of DFT energies and molecular thermochemistry are widely used in surface reaction energetics [50, 44]. Strongly anharmonic or nearly free adsorbate motions may require treatments beyond harmonic oscillators. Configurational entropy is not included by optimizing a single arrangement. Electron exchange introduces a further reservoir contribution under electrochemical conditions, treated in Section 2.9.6.

2.8 Minimum-Energy Paths and Transition States

The energetics of stable configurations alone do not determine how readily a process occurs. Adsorption-site migration, structural rearrangements, and chemical reactions also depend on the energy barriers separating these configurations. Minimum-energy paths on the potential-energy surface connect local minima through saddle points and provide a basis for identifying activation barriers [51]. Together with the vibrational properties of the minima and saddle points, these barriers can be used to estimate transition rates within harmonic transition-state theory (HTST) [52].

2.8.1 Potential-Energy Surfaces

Within the Born–Oppenheimer approximation, the electronic problem is solved for fixed nuclear positions. The resulting electronic ground-state energy, together with the repulsion between the nuclei, defines the potential energy surface (PES),

$$E_\mathrm{PES}(\mathbf{R}) = E_\mathrm{el}(\mathbf{R}) + E_\mathrm{NN}(\mathbf{R}), \tag{81}$$

where $\mathbf{R}$ collectively denotes the nuclear coordinates. Here, E_el excludes the nuclear–nuclear repulsion, which is included explicitly through E_NN. For a system containing N atoms, the energy depends on $3N$ Cartesian coordinates, although constraints and symmetry can reduce the number of independent degrees of freedom. Each point on this surface corresponds to an atomic configuration.

The forces acting on the nuclei are given by the negative gradient of the potential energy,

$$\mathbf{F}_a = -\nabla_{\mathbf{R}_a} E_\mathrm{PES}(\mathbf{R}), \tag{82}$$

where $\mathbf{R}_a$ is the position of atom a. Stationary configurations have vanishing gradients with respect to all unconstrained coordinates. Their local character is determined by the Hessian matrix as explained in Eq. 76. in section 2.7.4. A first-order saddle point is a stationary configuration with exactly one negative Hessian eigenvalue, after excluding constrained coordinates and

symmetry-related zero modes. The energy decreases along the associated unstable direction and increases along the remaining directions. In a harmonic description, the mass-weighted Hessian consequently has one negative eigenvalue, corresponding to an imaginary vibrational frequency [49]. A saddle point connecting reactant and product minima provides the reference configuration for a transition-state dividing surface in HTST [52].

A minimum-energy path connects the minima along a route for which no component of the energy gradient is perpendicular to the path. In Cartesian coordinates, this condition can be expressed as

$$\nabla E_{\mathrm{PES}} - (\nabla E_{\mathrm{PES}} \cdot \hat{\tau})\,\hat{\tau} = \mathbf{0}, \tag{83}$$

where $\hat{\tau}$ is the local unit tangent. Away from stationary points, the gradient is therefore parallel to the path. For an elementary transition between adjacent minima, the path passes through a first-order saddle point and follows steepest-descent directions toward the two minima [51].

The forward potential-energy barrier is the energy difference between the saddle point and the initial minimum,

$$\Delta E^{\ddagger} = E_{\mathrm{PES}}(\mathbf{R}^{\ddagger}) - E_{\mathrm{PES}}(\mathbf{R}_{\mathrm{i}}), \tag{84}$$

where $\mathbf{R}^{\ddagger}$ and $\mathbf{R}_{\mathrm{i}}$ denote the saddle-point and initial configurations, respectively. This barrier is distinct from an activation free energy, which also includes thermal and entropic contributions. Multiple minimum-energy paths may connect the same states, each corresponding to a different mechanism and potentially a different barrier. For surface diffusion and reactions, these paths describe the collective motion of the adsorbates and the response of the unconstrained substrate atoms. Numerical methods such as the NEB method are used to determine these paths and their associated barriers.

2.8.2 Nudged Elastic Band Method

The NEB method determines a minimum-energy path between two known configurations, typically relaxed local minima on the potential-energy surface. The path is described by a sequence of atomic configurations, called images, connecting the initial and final states. Neighboring images are coupled by artificial spring forces that maintain their distribution along the path while the intermediate configurations are optimized [51].

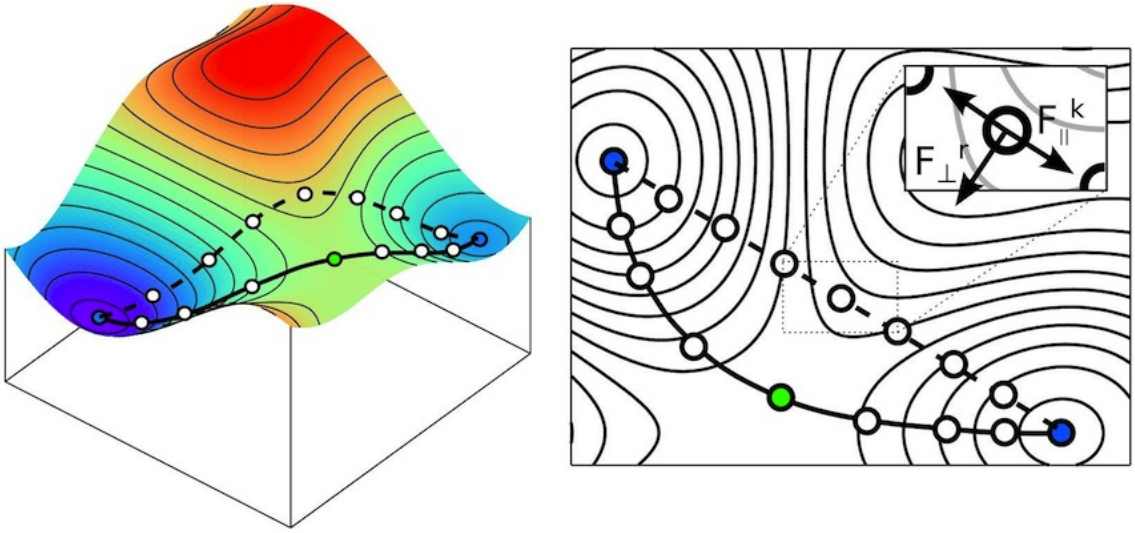

Figure 2.1. Schematic illustration of the NEB method on a model potential-energy surface. Left: three-dimensional representation of the surface and paths connecting two minima. Right: corresponding contour representation, with circles denoting discrete images along the paths. Blue circles indicate the endpoint minima, and the green circle marks the saddle point along the minimum-energy path. The inset illustrates the perpendicular component of the physical force, $F^r_\perp$, and the parallel component of the spring force, $F^k_\parallel$, used to optimize the band. Source: RheoMan project website, Université de Lille [53].

For a band containing M intermediate images, the configurations are denoted by $\mathbf{R}_0, \ldots, \mathbf{R}_{M+1}$, with the two endpoints held fixed. Each configuration contains the Cartesian coordinates of all unconstrained atoms. An initial path can be constructed by interpolating between the endpoints. Linear interpolation of Cartesian coordinates can produce excessively close atomic contacts. The image-dependent pair potential (IDPP) method provides an alternative by constructing an initial path from interpolated interatomic distances [54]. During optimization, the force acting on each intermediate image combines the component perpendicular to the path of the physical force with the spring force parallel to it,

$$\mathbf{F}_i^{\mathrm{NEB}} = -\left[\nabla E(\mathbf{R}_i)\right]_\perp + F^s_{i,\parallel}, \tag{85}$$

where

$$\left[\nabla E(\mathbf{R}_i)\right]_\perp = \nabla E(\mathbf{R}_i) - \left[\nabla E(\mathbf{R}_i)\cdot\hat{\boldsymbol{\tau}}_i\right]\hat{\boldsymbol{\tau}}_i \tag{86}$$

For a constant positive spring coefficient k_s, a commonly used parallel spring force is

$$\mathbf{F}^{\mathrm{s}}_{i,\parallel} = k_\mathrm{s}\left(|\mathbf{R}_{i+1}-\mathbf{R}_i| - |\mathbf{R}_i-\mathbf{R}_{i-1}|\right)\hat{\boldsymbol{\tau}}_i. \tag{87}$$

This projection of the forces is the essential feature of the nudging procedure. Removing the perpendicular spring force prevents the springs from pulling the band away from the minimum-energy path and cutting across curved portions of it. Removing the parallel physical force prevents images from sliding toward the endpoint minima. The remaining physical force relaxes the band toward the path, while the parallel spring force controls the spacing between images. Figure 2.1 illustrates how the discrete images represent a path across the potential-energy surface.

The tangent is estimated from neighboring configurations. Its definition affects the stability of the optimization, particularly near extrema in the energy profile. The improved tangent formulation

of Henkelman and Jónsson uses neighboring image energies to select or weight the forward and backward path directions, reducing the development of kinks in the band [55].

In conventional NEB, the highest-energy image generally lies near the saddle point but does not necessarily coincide with it. The climbing-image modification addresses this limitation by changing the force on a selected high-energy image after the band has approached the reaction path. The spring force is removed on this image and the component of the physical force parallel to the path is reversed,

$$\mathbf{F}_i^{\mathrm{CI}} = -\nabla E(\mathbf{R}_i) + 2\,[\nabla E(\mathbf{R}_i)\cdot\hat{\boldsymbol{\tau}}_i]\,\hat{\boldsymbol{\tau}}_i. \tag{88}$$

The image consequently moves uphill along the path while relaxing downhill in the perpendicular directions. With a sufficiently accurate tangent and a converged band, it approaches the saddle point, allowing the barrier to be determined directly from the saddle-point and initial-state energies [56].

The reliability of a NEB calculation depends on the initial path, the number of images, and the convergence of the projected forces. Sufficient images are needed to resolve curved pathways and any intermediate minima. Different initial paths can converge to different mechanisms, so a converged band does not establish that the lowest possible barrier has been found. The saddle-point configuration should also be checked for a single unstable vibrational mode corresponding to the intended transition. For adsorption site migration, the resulting path describes the motion of the adsorbate together with relaxation of the unconstrained substrate atoms.

2.8.3 Harmonic Transition-State Theory

A minimum-energy path identifies the potential-energy barrier separating two configurations, but the transition rate also depends on the temperature and the motion of the atoms around the initial state and saddle point. Transition state theory approximates the rate by the flux of systems, at equilibrium, passing through a surface that divides reactants from products. It assumes that the system equilibrates within the reactant regions before escape and that trajectories crossing the dividing surface toward the product do not subsequently recross it [57]. In HTST, the potential energy is approximated to second order around the initial minimum as explained in Section 2.7.4 and the first-order saddle point [52]. At the initial minimum, the vibrational eigenvalues are positive after removing any symmetry-related zero modes. At a first-order saddle point, one eigenvalue is negative, corresponding to the unstable mode along the transition direction. This mode is excluded from the saddle-point vibrational partition function because motion along it is accounted for by the flux through the dividing surface.

For a single transition pathway, the classical harmonic rate is given by the Vineyard expression,

$$k_{\mathrm{HTST}}(T) = \nu_0 \exp\left(-\frac{\Delta E^{\ddagger}}{k_{\mathrm{B}}T}\right), \tag{89}$$

with the prefactor

$$\nu_0 = \frac{\prod_{\alpha=1}^{d} \nu_\alpha^{\mathrm{i}}}{\prod_{\alpha=1}^{d-1} \nu_\alpha^{\ddagger}}. \tag{90}$$

Here, $\Delta E^{\ddagger}$ is the potential-energy barrier, and $\nu_\alpha = \omega_\alpha/(2\pi)$ denotes an ordinary frequency. The initial state has d stable modes, while the saddle point has $d-1$ stable modes after excluding the

unstable direction. Constraints and zero modes must be treated consistently in both configurations. The frequency ratio has units of inverse time and accounts for the different vibrational properties of the initial state and saddle point. Thus, processes with similar barriers can still have different rates because their prefactors differ [52].

The classical expression assumes that the relevant vibrational modes are thermally populated. Quantum harmonic statistics can instead be included through the vibrational partition functions,

$$k_{\mathrm{HTST}}^{\mathrm{qh}}(T) = \frac{k_{\mathrm{B}}T}{h}\frac{Q_{\mathrm{vib}}^{\ddagger}(T)}{Q_{\mathrm{vib}}^{\mathrm{i}}(T)}\exp\left(-\frac{\Delta E^{\ddagger}}{k_{\mathrm{B}}T}\right), \tag{91}$$

where each partition function is constructed from its stable harmonic modes,

$$Q_{\mathrm{vib}}(T) = \prod_{\alpha}\frac{\exp\left[-h\nu_{\alpha}/(2k_{\mathrm{B}}T)\right]}{1-\exp\left[-h\nu_{\alpha}/(k_{\mathrm{B}}T)\right]}. \tag{92}$$

This expression follows the statistical-mechanical formulation of transition-state theory, in which the rate depends on the relative statistical weights of the transition state and the initial state [58]. These partition functions include zero-point energies relative to the corresponding potential-energy stationary points. Accordingly $\Delta E^{\ddagger}$ in this expression is the uncorrected potential-energy barrier; adding a separate zero-point correction would count that contribution twice. In the high-temperature limit, the expression reduces to the classical Vineyard rate. Quantizing the stable vibrations in this way does not account for tunneling along the reaction coordinate [57].

For surface diffusion, HTST connects the saddle points obtained from NEB calculations to hopping rates between adsorption sites. Its accuracy depends on the validity of the harmonic approximation and the neglect of recrossing. Large-amplitude motion, strongly anharmonic low-frequency modes, and shallow barriers can reduce its reliability. If several equivalent pathways leave the same initial state, their individual rates must be summed to obtain the total escape rate.

2.9 Electrochemical Density Functional Theory Modeling

Electrochemical reactions take place at an electrode–electrolyte interface, where the energetics of adsorbed species depend on both the electronic structure of the electrode and its interaction with the surrounding solution. Solvent molecules and dissolved ions influence these energetics through hydrogen bonding, dielectric screening, and the formation of the electrical double layer. The applied electrode potential controls the electron electrochemical potential and affects the interfacial charge distribution, thereby influencing adsorption, reaction thermodynamics, and activation barriers. A computational description of electrochemical processes must therefore account for the coupled response of the electrode and electrolyte [59].

Several approaches have been developed to incorporate these effects into DFT calculations. They differ in how the solvent and ions are represented, how electrode potential is introduced or controlled, and how exchange with the surrounding reservoirs enters the thermodynamic description. This section introduces electrode-potential reference scales and the computational hydrogen electrode (CHE), followed by solvation models and constant-charge and constant-potential formulations. These concepts provide the basis for evaluating adsorption and reaction energetics under electrochemical conditions.

2.9.1 The Electrochemical Interface

When an electrode is brought into contact with an electrolyte, the distribution of electrons at its surface and the arrangement of nearby solvent molecules and ions adjust to their mutual interactions. The resulting interfacial region differs from both the bulk electrode and the bulk solution. In aqueous electrolytes, water molecules interact with the surface and form a hydrogen-bond network whose structure depends on the electrode material, adsorbate coverage, and applied potential. Experiments on platinum single-crystal electrodes demonstrate that the preferred orientation of interfacial water changes with electrode potential and surface orientation [60]. Dissolved ions also redistribute near the surface and may interact directly with adsorbed species. Together, these effects determine the local environment in which electrochemical reactions occur [59].

An excess charge on the electrode is screened by polarization of the solvent and redistribution of dissolved ions, producing an electrical double layer. In the Helmholtz model, the electrode charge and the compensating electrolyte charge are represented by two oppositely charged layers separated by a finite distance, analogous to a parallel-plate capacitor [61]. This compact-layer picture does not account for the thermal motion of ions. Gouy and Chapman introduced a diffuse-layer description in which the ionic distribution reflects the competition between electrostatic interactions and thermal motion [62, 63]. Stern combined these descriptions by distinguishing a compact region adjacent to the electrode from a diffuse region extending into the electrolyte [64].

The compact region contains interfacial solvent molecules and may include specifically adsorbed ions. In the description developed by Grahame, the inner Helmholtz plane represents the location of the centers of specifically adsorbed ions, whereas the outer Helmholtz plane is made up of the closest solvated ions that do not adsorb specifically. Beyond the outer Helmholtz plane, the diffuse ionic distributions gradually approach their bulk values [65]. These planes provide an idealized description of an interface that, at the molecular level, fluctuates and can exhibit substantial structural heterogeneity.

The interfacial charge distribution generates a spatially varying electrostatic potential. Far enough into a metallic electrode, the electric field is screened, while sufficiently far into an equilibrium bulk electrolyte the solution is approximately electroneutral and the mean electrostatic potential becomes uniform. The potential variation between these regions depends on the electrode charge, solvent polarization, ionic distributions, and interfacial dipoles [66]. Consequently, a change in applied potential can alter both the charge on the electrode and the structure of the surrounding electrolyte.

The response of the electrode charge to the applied potential is characterized by the differential interfacial capacitance per unit area,

$$C_{\mathrm{diff}} = \left(\frac{\partial \sigma}{\partial U} \right)_{T,\mu_j}, \tag{93}$$

where σ is the electrode charge density, U is the electrode potential relative to a specified reference, and the derivative is taken at fixed temperature and chemical potentials μ_j of the electrolyte reservoirs [66]. The capacitance need not be constant because solvent orientation, ion accumulation, and adsorption can change with potential. Measurements on Pt(111), for example, reveal a capacitance response that requires consideration of ion–surface interactions and the

potential-dependent response of interfacial water beyond the classical Gouy–Chapman–Stern description [67].

A useful reference is the potential of zero charge, at which the specified electrode surface charge vanishes. This does not imply the absence of interfacial structure or a potential variation: oriented water molecules and chemical bonding can produce interfacial dipoles even at zero net electrode charge. When specific adsorption occurs, the distinction between free electrode charge and total charge, including contributions associated with adsorption, must be made explicit when defining the potential of zero charge [66].

For computational modeling, these features require a description of both local chemical interactions and the longer-range electrostatic response of the electrolyte. The electrode charge, solvent structure, and ionic distributions are coupled, and their response to the applied potential influences adsorption and reaction energetics [59]. Establishing how electrode potential is defined and related to the electron electrochemical potential is therefore an essential step in connecting atomistic calculations to the electrochemical conditions.

2.9.2 Electrode Potential and the Electronic Chemical Potential

The electrode potential determines the electrochemical potential of electrons and therefore their tendency to participate in reduction or oxidation reactions. For an electron, the electrochemical potential can be expressed by

$$\tilde{\mu}_{\mathrm{e}} = \mu_{\mathrm{e}} - e\phi, \tag{94}$$

where μ_{e} is the chemical contribution, ϕ is the inner electrostatic potential, and e is the elementary charge. All chemical potentials here are expressed as energies per particle. The electrochemical potential includes both chemical and electrostatic contributions and, for a metallic electrode in electronic equilibrium, corresponds to its Fermi level when a consistent energy reference is used [66].

Experimentally, an electrode potential is measured relative to a reference electrode. When the electron electrochemical potentials are expressed on a common energy scale, the potential of the working electrode relative to the reference is

$$U_{\mathrm{vs,ref}} = -\frac{\tilde{\mu}_{\mathrm{e}} - \tilde{\mu}_{\mathrm{e}}^{\mathrm{ref}}}{e}. \tag{95}$$

Thus, making the electrode potential more negative raises the electron electrochemical potential, increasing the driving force for electron donation. A more positive potential lowers it. This sign convention is essential when relating applied potentials to electronic energies [68].

The standard hydrogen electrode (SHE) provides a conventional reference based on the equilibrium

$$\mathrm{H^+(aq)} + \mathrm{e^-} \rightleftharpoons \frac{1}{2}\mathrm{H_2(g)}. \tag{96}$$

Its standard potential is assigned a value of zero at unit proton activity and unit hydrogen fugacity relative to the standard state. This defines a relative electrochemical scale; it does not imply that the electron electrochemical potential of the SHE is zero relative to vacuum [66].

An absolute potential scale instead references the electron energy to an electron at rest in vacuum outside the solution [69, 68]. Taking this vacuum energy as zero gives

$$\tilde{\mu}_{\mathrm{e}} = -eU_{\mathrm{abs}}, \qquad U_{\mathrm{abs}} = U_{\mathrm{SHE}} + U_{\mathrm{SHE}}^{\mathrm{abs}}, \tag{97}$$

where U_{SHE} denotes the working-electrode potential measured versus SHE, and $U_{\mathrm{SHE}}^{\mathrm{abs}}$ is the absolute potential of the SHE. The commonly used IUPAC-recommended value is $U_{\mathrm{SHE}}^{\mathrm{abs}} = 4.44 \pm 0.02$ V at 298 K [68]. On this scale,

$$\tilde{\mu}_{\mathrm{e}} = -e\left(U_{\mathrm{SHE}} + U_{\mathrm{SHE}}^{\mathrm{abs}}\right). \tag{98}$$

In electronic-structure calculations, establishing this reference requires care because the zero of the electrostatic potential is arbitrary. For a slab with a well-defined vacuum region, the work function is

$$W = E_{\mathrm{vac}} - \varepsilon_{\mathrm{F}}, \tag{99}$$

where E_{vac} is the vacuum electron-energy level and ε_{F} is the Fermi energy. For an electrochemical interface, the reference must also account for the potential offsets associated with the electrode–solution and solution–vacuum interfaces. A Fermi level referenced to the bulk solution cannot therefore be identified directly with a vacuum-referenced electron electrochemical potential. Conversion to an experimental potential scale requires consistent potential alignment or calibration of the reference electrode within the computational model [70, 71]. Likewise, the work function of a clean surface in vacuum does not by itself determine the potential of that surface in contact with an electrolyte [70].

The reversible hydrogen electrode (RHE) uses the same hydrogen equilibrium but follows the proton activity of the solution. At unit hydrogen fugacity relative to the standard state, the Nernst equation gives its potential versus SHE as [72, 66]

$$U_{\mathrm{RHE\,vs\,SHE}} = -\frac{k_{\mathrm{B}}T\ln 10}{e}\mathrm{pH}, \tag{100}$$

where $\mathrm{pH} = -\log_{10} a_{\mathrm{H^+}}$, and $a_{\mathrm{H^+}}$ is the dimensionless proton activity. Consequently, the potential of a working electrode on the two scales is related by

$$U_{\mathrm{RHE}} = U_{\mathrm{SHE}} + \frac{k_{\mathrm{B}}T\ln 10}{e}\mathrm{pH}. \tag{101}$$

At 298.15 K, the conversion becomes

$$U_{\mathrm{RHE}} = U_{\mathrm{SHE}} + 0.05916\ \mathrm{V\,pH}. \tag{102}$$

The RHE scale therefore incorporates the pH-dependent shift of the hydrogen equilibrium and is particularly useful for discussing proton-coupled electron-transfer reactions [66, 59]. It does not remove other effects of pH on interfacial structure or reaction kinetics.

Combining the reference-scale relations yields

$$\tilde{\mu}_{\mathrm{e}} = -e\left[U_{\mathrm{RHE}} - \frac{k_{\mathrm{B}}T\ln 10}{e}\mathrm{pH} + U_{\mathrm{SHE}}^{\mathrm{abs}}\right]. \tag{103}$$

Specifying a potential vs. RHE therefore requires the pH to determine the corresponding vacuum-referenced electron electrochemical potential. These reference conventions also underpin the CHE, which uses the hydrogen equilibrium to relate proton-electron transfers to molecular hydrogen.

2.9.3 The Computational Hydrogen Electrode

The CHE provides a thermodynamic framework for evaluating electrochemical reaction energies without explicitly calculating the free energy of a solvated proton. Introduced by Nørskov and co-workers, the method uses the equilibrium between molecular hydrogen and a proton–electron pair to establish a reference for reactions involving proton and electron transfer [50]. Combined with DFT energies and thermochemical corrections, this reference allows reaction free-energy diagrams to be constructed as functions of electrode potential and pH.

At equilibrium with the SHE, the electrochemical potentials of a proton and an electron satisfy

$$\tilde{\mu}^{\circ}_{\mathrm{H^+}} + \tilde{\mu}^{\mathrm{SHE}}_{\mathrm{e}} = \frac{1}{2}\mu^{\circ}_{\mathrm{H_2}}, \tag{104}$$

where $\mu^{\circ}_{\mathrm{H_2}}$ is the chemical potential of $\mathrm{H_2(g)}$ at the temperature of interest and standard fugacity. Using the potential and activity conventions introduced in the preceding subsection, the combined chemical potential at an arbitrary potential and pH is

$$\tilde{\mu}_{\mathrm{H^+}} + \tilde{\mu}_{\mathrm{e}} = \frac{1}{2}\mu^{\circ}_{\mathrm{H_2}} - eU_{\mathrm{SHE}} - k_{\mathrm{B}}T\ln 10\,\mathrm{pH}. \tag{105}$$

The CHE therefore replaces the combined proton–electron reference with one-half of the chemical potential of molecular hydrogen and a potential-dependent correction [50, 59].

As an example, consider hydrogen adsorption through the reduction step

$$* + \mathrm{H^+} + \mathrm{e^-} \rightarrow \mathrm{H^*}, \tag{106}$$

where $*$ denotes an available surface site and $\mathrm{H^*}$ an adsorbed hydrogen atom. Its reaction free energy is

$$\Delta G_{\mathrm{H}} = G_{\mathrm{H^*}} - G_{*} - (\tilde{\mu}_{\mathrm{H^+}} + \tilde{\mu}_{\mathrm{e}}). \tag{107}$$

Substitution of the CHE reference gives

$$\Delta G_{\mathrm{H}}(U_{\mathrm{RHE}}) = \Delta G^{0}_{\mathrm{H}} + eU_{\mathrm{RHE}}, \tag{108}$$

with

$$\Delta G^{0}_{\mathrm{H}} = G_{\mathrm{H^*}} - G_{*} - \frac{1}{2}\mu^{\circ}_{\mathrm{H_2}}. \tag{109}$$

A more negative potential therefore makes this reduction step more favorable. Hydrogen adsorption free energies evaluated in this way have been used to rationalize trends in hydrogen-evolution activity across metal surfaces [73]. More generally, a reduction step consuming n proton–electron pairs has the CHE potential dependence

$$\Delta G(U_{\mathrm{RHE}}) = \Delta G^{0} + neU_{\mathrm{RHE}}, \tag{110}$$

provided that additional potential dependence of the other species is neglected. The sign reverses for the corresponding oxidation step.

The reference reaction free energies are obtained from electronic-structure calculations with appropriate thermochemical corrections. A commonly used approximation is

$$\Delta G^{0} \approx \Delta E_{\mathrm{DFT}} + \Delta E_{\mathrm{ZPE}} + \Delta H_{\mathrm{thermal}} - T\Delta S, \tag{111}$$

where ΔE_{ZPE} is the zero-point-energy correction, $\Delta H_{\mathrm{thermal}}$ is the additional thermal enthalpy contribution, and ΔS is the entropy change. Molecular reference species require appropriate translational, rotational, and vibrational contributions, while adsorbed species are commonly treated using their vibrational modes [50, 73]. Solvation contributions must also be included consistently when the underlying calculations do not already account for them [59].

Applying these expressions to successive reaction steps produces potential-dependent free-energy diagrams. For example, the CHE has been used to compare proposed pathways for CO_2 reduction on copper and identify thermodynamically unfavorable proton–electron transfer steps [74]. Such diagrams describe the relative free energies of intermediates; they do not provide activation barriers or, by themselves, establish the rate-determining step. Likewise, representing a transformation as the transfer of a proton–electron pair does not establish that proton and electron transfer occur concertedly [59].

The hydrogen-reference relation is a thermodynamic identity, whereas the simplest CHE implementation introduces further approximations. In particular, intermediate energies are usually calculated for selected surface configurations and then held fixed while the potential-dependent reservoir contribution is added. Changes in surface charging, interfacial electric fields, solvent structure, and adsorbate stabilization with potential are therefore not automatically captured. Likewise, a step without net proton–electron transfer receives no explicit CHE potential correction, although its energy and barrier may still depend on potential through changes in the interface. These limitations motivate combining thermochemical referencing with more detailed descriptions of solvation and electrode charging [59].

2.9.4 Solvation and Electrolyte Models

The surrounding electrolyte affects adsorption and reaction energetics through solvent polarization, hydrogen bonding, and the redistribution of dissolved ions. These effects can stabilize reaction intermediates and transition states differently, changing both reaction free energies and activation barriers. Their computational description requires a balance between the molecular detail retained at the interface and the cost of sampling the liquid environment [59].

In an explicit solvent model, individual solvent molecules and, where appropriate, dissolved ions are included in the atomic structure. This allows specific interactions, such as hydrogen bonding, ion coordination, and solvent-mediated proton transfer, to be described. However, a single optimized solvent configuration does not represent the thermal ensemble of a liquid. Reliable free energies generally require sampling many configurations, for example through molecular dynamics, together with sufficient system sizes to accommodate the interfacial structure and its fluctuations. Performing this sampling entirely at the DFT level can be computationally demanding [59].

Implicit solvation models reduce this cost by replacing the molecular solvent with a continuous medium characterized by its dielectric response. The electrode and adsorbates remain explicitly described by DFT, while the surrounding medium responds to their charge distribution. Dissolved ions can additionally be represented through continuous concentration fields. Dielectric polarization describes the response of the solvent, whereas ionic screening describes the redistribution of mobile charge in the electrolyte [75, 76].

A continuum model requires a boundary separating the explicitly treated system from the surrounding solvent. In density-based approaches, this boundary is defined using a smooth cavity

function constructed from the electronic density. For a local, linear dielectric model, the relative permittivity can be written as

$$\varepsilon_{\mathrm{r}}(\mathbf{r}) = 1 + (\varepsilon_{\mathrm{r}} - 1)\, s_{\mathrm{d}}(\mathbf{r}), \tag{112}$$

where ε_{r} is the bulk relative permittivity and s_{d} varies smoothly from zero inside the solvent-excluded region to unity in the bulk solvent. The dielectric response therefore develops gradually across the cavity boundary. Its coupling to the electronic density allows the solvent polarization and the electronic structure to be determined self-consistently [77, 75].

For this linear dielectric description, the electrostatic potential satisfies

$$-\nabla \cdot [\varepsilon_0 \varepsilon_{\mathrm{r}}(\mathbf{r}) \nabla \phi(\mathbf{r})] = \rho_{\mathrm{explicit}}(\mathbf{r}) + \rho_{\mathrm{ion}}(\mathbf{r}), \tag{113}$$

where ε_0 is the vacuum permittivity, ρ_{explicit} is the charge density of the explicitly treated nuclei and electrons, and ρ_{ion} is the charge density of the continuum ions. These equations are written in SI units. In the ideal point-ion Poisson–Boltzmann description,

$$\rho_{\mathrm{ion}}(\mathbf{r}) = \sum_{\alpha} z_\alpha e\, c_\alpha(\mathbf{r}), \tag{114}$$

with

$$c_\alpha(\mathbf{r}) = s_{\mathrm{ion}}(\mathbf{r}) c_\alpha^{\mathrm{b}} \exp\left[-\frac{z_\alpha e\,(\phi(\mathbf{r}) - \phi_{\mathrm{b}})}{k_{\mathrm{B}} T}\right]. \tag{115}$$

Here, z_α and c_α^{b} are the signed valence and bulk number density of ionic species α, ϕ_{b} is the bulk-solution potential, and s_{ion} specifies the region accessible to ions. The resulting ionic charge screens the electrode charge. Linearizing the Boltzmann factors gives the linearized Poisson–Boltzmann approximation, used in the electrolyte extension of VASPsol [76].

The nonlinear and nonlocal model implemented in VASPsol++ extends this description in ways that are particularly relevant near charged electrodes. Its nonlinear dielectric response accounts for the progressive alignment and eventual saturation of solvent dipoles in strong electric fields [78]. Its ionic response includes finite-size crowding, limiting the accumulation of counterions that would otherwise grow without bound in the ideal point-ion model. The physical basis for such concentration saturation is described by modified Poisson–Boltzmann theories that incorporate the finite volume occupied by ions [79, 78].

The finite size of solvent molecules also matters when defining the continuum boundary. Solvent-aware cavity constructions suppress unphysical continuum solvent pockets in regions too small to accommodate a solvent molecule [80]. VASPsol++ addresses this problem through a nonlocal cavity construction in which accessibility depends on the surrounding geometry, rather than purely on the electron density at a single point. Separate dielectric and ionic cavities account for the different effective sizes of solvent molecules and solvated ions, allowing solvent polarization and mobile-ion distributions to begin at different distances from the explicitly treated surface [78].

The continuum contribution includes both electrostatic and non-electrostatic terms. In VASPsol++, cavity formation is represented using an effective surface-tension contribution,

$$G_{\mathrm{cav}} = \tau A_{\mathrm{cav}}, \tag{116}$$

where τ is the effective surface tension and A_{cav} is the area of the chosen cavity boundary. The dielectric response, ionic screening, and cavity contribution are coupled to the electronic calculation, so the continuum environment affects energies and forces during structural optimization.

Relevant model parameters include the bulk permittivity, electrolyte concentration, effective species sizes, and cavity definition [78].

Despite these extensions, a continuum description does not resolve individual hydrogen bonds, discrete solvent arrangements, or the chemical coordination of specifically adsorbed ions. When these interactions are important, an explicit–implicit approach can be used: selected solvent molecules or ions are included in the DFT region, while the surrounding liquid is represented by the continuum. This provides local molecular detail while retaining an economical description of longer-range screening. The explicit configurations still require adequate sampling [59]. The continuum boundary must also exclude spaces already occupied by the explicit solvent, making solvent accessibility particularly important in these combined models [80, 78].

The electrolyte model and the treatment of electrode potential address related but distinct aspects of the calculation. The former determines how the environment responds to charge, while the latter determines whether the electron number or electron electrochemical potential is controlled. Their combination provides the basis for the constant-charge and constant-potential calculations discussed next.

2.9.5 Constant-Charge and Constant-Potential DFT

Conventional DFT calculations optimize the electronic density at a fixed number of electrons. In an electrochemical experiment performed at controlled electrode potential, however, the electrode can exchange electrons with an external circuit. Its charge therefore adjusts as the interfacial structure changes. Computational descriptions of these conditions differ in whether the electron number or the electron electrochemical potential is held fixed [81].

In a constant-charge calculation, the electron number N_e is specified. For a fixed atomic composition, the net charge of the explicitly treated system is

$$Q = -e\left(N_\mathrm{e} - N_\mathrm{e}^0\right), \tag{117}$$

where N_e^0 is the electron number of the corresponding neutral system and $e > 0$ is the elementary charge. Adding electrons therefore produces a negative charge. This constraint fixes the total charge of the explicit region, while allowing charge to redistribute between the electrode, adsorbates, and any explicitly included solvent molecules.

The electrode potential is an outcome of a constant-charge calculation. Changes in adsorption geometry, surface dipoles, or solvent orientation can shift the Fermi level relative to the electrolyte reference even when the electron number remains unchanged. Consequently, different configurations along a reaction path calculated at fixed charge generally correspond to different electrode potentials. This effect can be significant in small simulation cells, where a localized reaction represents a substantial perturbation of the interface [59].

Constant-potential calculations instead fix the electron electrochemical potential, $\tilde{\mu}_\mathrm{e}$, and allow the electron number to adjust. The target value is related to the applied electrode potential through the reference conventions introduced previously. At each atomic configuration, electronic equilibrium with the reservoir requires

$$\tilde{\mu}_\mathrm{e}^\mathrm{calc} = \tilde{\mu}_\mathrm{e}^\mathrm{target}. \tag{118}$$

The electron number can therefore change continuously during structural relaxation or along a

reaction path. This represents exchange with the external circuit and maintains the prescribed potential as the interfacial electronic structure evolves [81].

The thermodynamic distinction can be expressed through a Legendre transformation,

$$\Omega(\tilde{\mu}_\mathrm{e}, \mathbf{R}) = \min N_\mathrm{e} \left[\mathscr{F}(N_\mathrm{e}, \mathbf{R}) - \tilde{\mu}_\mathrm{e} N_\mathrm{e} \right], \tag{119}$$

where $\mathbf{R}$ denotes the explicitly treated nuclear coordinates. Here, $\mathscr{F}$ is the interfacial free-energy functional at fixed electron number, after equilibration of the electronic density and continuum electrolyte; temperature and electrolyte reservoir conditions are held fixed. The subtraction accounts for electron exchange with the reservoir. This defines an electronically grand-canonical description and provides the basis for comparing adsorption and reaction energetics at constant potential [81, 82].

Numerically, the target potential can be reached through iterative fixed-electron-number calculations, adjusting N_e until the calculated electron electrochemical potential matches the target. Alternatively, the electron number can be updated within the electronic optimization itself. In either approach, the electronic density, electrolyte response, and electron number must be converged consistently at each atomic configuration [81, 59].

VASPsol++ combines electron-number adjustment with the implicit electrolyte model described in the preceding subsection. Its continuum ionic distribution supplies the compensating charge as the explicit region gains or loses electrons, while solvent polarization contributes to the interfacial screening. This allows the electrode charge to respond to structural changes under a prescribed electron electrochemical potential [78]. The target must be expressed using the same energy reference as the calculated Fermi level. Conversion to an experimental scale therefore requires consistent potential alignment or calibration within the chosen electrolyte model; a bulk-solution reference should not be treated automatically as a vacuum reference [71, 59].

Constant-charge and constant-potential approaches are thermodynamically related. Constant-charge calculations can be used to reconstruct constant-potential energetics by sampling the charge dependence and applying the appropriate transformation [82]. For a localized process at a metallic interface, the potential change caused by a single event decreases as the lateral system size increases. Consistently formulated differential reaction free energies from the two approaches consequently agree in the appropriate infinite-system limit. At finite cell sizes, direct constant-potential calculations can reduce the associated potential shifts and simplify interpretation, although their accuracy still depends on the electrolyte model and potential reference [83].

For adsorption and reaction calculations, maintaining a common potential generally means comparing configurations with different electron numbers. Their raw DFT energies therefore do not alone provide the relevant thermodynamic differences. The electron-reservoir contribution must also be included, as developed in the following subsection on grand-canonical adsorption and reaction energetics.

2.9.6 Grand-Canonical Density Functional Theory

At constant electrode potential, adsorption and chemical reactions can be accompanied by electron exchange with the external circuit. The relevant thermodynamic differences must therefore include both the change in interfacial free energy and the contribution from the electron

reservoir. Using the electronically grand-canonical description introduced above, the difference between two configurations of identical atomic composition is

$$\Delta\Omega(U) = \mathscr{F}_{\mathrm{f}}(U) - \mathscr{F}_{\mathrm{i}}(U) - \tilde{\mu}_{\mathrm{e}}(U)\left[N_{\mathrm{e,f}}(U) - N_{\mathrm{e,i}}(U)\right], \tag{120}$$

where the initial, i, and final, f, states are equilibrated at the same electrode potential U, temperature, and electrolyte conditions. Their electron numbers can differ even when the process involves only a rearrangement of atoms [81, 82].

For adsorption, the atomic composition of the explicitly treated system changes, so the electrons brought by the adsorbing species must also be accounted for. Consider adsorption of a neutral molecule A,

$$* + A \rightarrow *A, \tag{121}$$

where $*$ denotes the surface before adsorption. The number of electrons supplied by the external circuit is

$$\Delta N_{\mathrm{res}} = N_{\mathrm{e},*A} - N_{\mathrm{e},*} - N^{0}_{\mathrm{e},A}, \tag{122}$$

where $N^{0}_{\mathrm{e},A}$ is the electron number of the neutral molecule. All electron counts must follow the same convention, including the same core–valence partition in PAW calculations. The adsorption free energy at constant potential is then

$$\Delta G_{\mathrm{ads}}(U) = \mathscr{F}_{*A}(U) - \mathscr{F}_{*}(U) - \mu_A - \tilde{\mu}_{\mathrm{e}}(U)\Delta N_{\mathrm{res}}(U). \tag{123}$$

Here, μ_A is the chemical potential of the neutral molecular reservoir. With this sign convention, negative values indicate thermodynamically favorable adsorption.

A convenient equivalent formulation uses the excess electron number relative to the neutral system of each composition,

$$\delta N_{\mathrm{e},X} = N_{\mathrm{e},X} - N^{0}_{\mathrm{e},X}. \tag{124}$$

Defining

$$\overline{\Omega}_X(U) = \mathscr{F}_X(U) - \tilde{\mu}_{\mathrm{e}}(U)\delta N_{\mathrm{e},X}(U) \tag{125}$$

gives

$$\Delta G_{\mathrm{ads}}(U) = \overline{\Omega}_{*A}(U) - \overline{\Omega}_{*}(U) - \mu_A. \tag{126}$$

The overbar distinguishes this neutral-reference convention from the grand potential defined using the total electron number. They differ by $\tilde{\mu}_{\mathrm{e}} N^{0}_{\mathrm{e},X}$, which cancels out between configurations of identical composition but must be handled consistently when molecules are added or removed. This bookkeeping ensures that only electrons exchanged with the external circuit enter the reservoir correction [84].

For multiple CO adsorption, the differential adsorption free energy becomes

$$\Delta G_{\mathrm{ads},n}(U) = \overline{\Omega}_{*\mathrm{CO}_n}(U) - \overline{\Omega}_{*\mathrm{CO}_{n-1}}(U) - \mu_{\mathrm{CO}}. \tag{127}$$

Each surface configuration is evaluated at the same potential, while its excess electron number and electrolyte response are allowed to adjust. The molecular chemical potential must correspond to the chosen reservoir, such as gaseous CO at a specified pressure or dissolved CO at a specified activity. Comparisons between adsorption sites at the same coverage do not require a molecular reference because their compositions are identical.

Even adsorption of a neutral molecule can depend on electrode potential. Adsorption changes the interfacial dipole, charge distribution, and charging response, so maintaining a fixed potential may require electron exchange with the reservoir. The resulting potential dependence need not follow the simple integer-*neU* form used for proton–electron transfer steps in the basic CHE approximation [82, 84].

The same reasoning applies to reaction barriers. For a transition that conserves the explicit atomic composition, the activation grand free energy is

$$\Delta\Omega^{\ddagger}(U) = \Omega^{\ddagger}(U) - \Omega_i(U). \tag{128}$$

The initial state and transition state must be evaluated at the same electron electrochemical potential. In a constant-potential NEB calculation, each image consequently has its own equilibrated electron number, and the path is optimized on the grand-potential surface [81, 59]. A path obtained at fixed charge generally samples changing electrode potentials and does not directly provide this barrier. Constant-potential barriers can nevertheless be reconstructed from sufficiently sampled constant-charge energy landscapes through a Legendre transformation [85].

A stationary-point calculation with an implicit electrolyte includes the free-energy contributions represented by that continuum model, but it does not automatically include all nuclear thermal contributions. Zero-point energies, vibrational corrections, and molecular reservoir contributions must therefore be included consistently when constructing adsorption or activation free energies. Likewise, a NEB barrier based on optimized structures does not by itself account for configurational sampling of explicitly included solvent molecules [59].

In practical calculations, the energy convention reported by the software must be identified before applying a reservoir correction. In its documented constant-potential mode, VASPsol++ already includes the term

$$-\tilde{\mu}_{\mathrm{e}}\delta N_{\mathrm{e}} \tag{129}$$

in the reported energies, including the extrapolated E_0 value. This contribution must therefore be included only once. Consistent electrolyte parameters, potential references, and energy conventions are required throughout each adsorption or reaction comparison [78].

3 Electrochemical Reduction of Carbon Dioxide

The electrochemical reduction of carbon dioxide offers a route for using electricity to produce carbon-containing fuels and chemical feedstocks. When coupled to low-carbon electricity, it has the potential to reduce reliance on fossil-derived production, although its practical benefits depend on the efficiency and integration of the overall process. At the electrode, the central challenge is to direct a network of competing reactions toward a desired product while maintaining sufficient activity and stability [86, 3].

Copper occupies a central position in this field because of its capability to form hydrocarbons and alcohols from CO_2 in aqueous electrolytes. Early studies established both its distinctive product distribution and the importance of adsorbed carbon monoxide as an intermediate in further reduction [87, 7]. Subsequent research has shown that copper's activity and selectivity depend on the combined effects of surface structure, composition, electrode potential, and the local electrolyte environment. Understanding these effects requires connecting the behavior of individual adsorbed intermediates to the reaction pathways available at the interface [9, 88].

CO adsorption provides a particular focus for this thesis. The strength and geometry of CO binding, the number of molecules accommodated near a site, and their ability to move across the surface help determine which adsorbed configurations are accessible for subsequent reactions. Terraces, steps, and substitutional impurities provide different local environments in which to examine these properties. Surface structure must also be considered as responsive to reaction conditions: changes in adsorbate populations and the surrounding electrolyte can accompany changes in the atomic arrangement of the catalyst [9, 89].

This chapter reviews the experimental and theoretical background relevant to CO adsorption on copper-based catalysts. It begins with the historical development of CO_2 electroreduction and the principal reaction pathways, before examining the influence of copper surface structure. Particular attention is then given to CO adsorption sites, coverage effects, lateral interactions, and diffusion, followed by their relevance to carbon–carbon coupling. The final discussion considers substitutional impurities and copper-based SAAs, focusing on multiple CO adsorption and the stability of different impurity environments. These topics establish the context for the research questions addressed by the original articles presented in Chapter 4.

3.1 Background and Historical Development

Research on the electrochemical reduction of carbon dioxide predates its present association with renewable energy and carbon recycling. Early investigations focused on establishing whether CO_2 could be reduced at an electrode, identifying the resulting products, and distinguishing the measured currents from competing processes such as hydrogen evolution. Polarographic studies by van Rysselberghe and co-workers in the 1940s examined the response of dissolved

CO_2 at dropping mercury electrodes and investigated the interpretation of the observed reduction waves [90]. In 1954, Teeter and van Rysselberghe combined polarization measurements with electrolysis experiments on mercury cathodes, identifying formic acid as the detectable reduction product and reporting "high" current efficiencies under their investigated conditions [91]. These studies provided an early experimental basis for examining CO_2 reduction as a process whose outcome depends on the electrode and electrolyte.

A major development in the understanding of metal-dependent selectivity came from the work of Hori and co-workers. In 1985, they analyzed both gaseous and dissolved products formed during CO_2 electrolysis on a series of metal electrodes in aqueous bicarbonate solution. Cadmium, indium, tin, and lead predominantly produced formate, while silver and gold primarily produced CO. Copper differed by producing an appreciable amount of methane [87]. Measuring both gas-phase and solution products was essential to this comparison, since analysis of only one phase could overlook important reaction channels. This work helped establish that the electrode material governs whether reduction ends at a two-electron product or proceeds towards further reduced products.

Subsequent investigations demonstrated that copper could produce several hydrocarbons and alcohols and clarified the importance of the reaction environment. Hori, Murata, and Takahashi reported in 1989 that the distribution of CO, methane, ethylene, and alcohols depended strongly on electrode potential and electrolyte composition. Their results supported a role for adsorbed CO as an intermediate that undergoes further reduction at sufficiently negative potentials. They also connected changes in product selectivity to the availability of hydrogen or protons near the surface and to the local pH, which can differ from that of the bulk solutions during electrolysis [7]. Thus, several questions that remain central to the field, like the fate of adsorbed CO, competition with hydrogen evolution, and the influence of the interfacial environment, were already appearing in these early copper studies.

The recognition that copper's atomic arrangement also influences its selectivity motivated investigations using single-crystal electrodes. Comparisons between crystallographic orientations and stepped surfaces showed that copper cannot be described by a single, structure-independent catalytic response. These experiments established a basis for relating product distributions to terrace orientation and step structure, and for using well-defined surfaces to investigate the local environments involved in CO_2 reduction [8]. Later assessments emphasized that surface structure and reaction conditions must be considered together when interpreting differences between measurements [92, 9].

Interest in CO_2 electroreduction subsequently broadened alongside the development of renewable electricity and the search for alternatives to fossil-derived chemical production. The process was increasingly considered as a means of storing electrical energy in chemical form and supplying carbon-containing feedstocks. This perspective also highlighted the need to improve catalysts, electrolytes, and reactor designs together, since product selectivity alone does not establish the efficiency or practicality of the overall conversion [86].

Theoretical studies provided a complementary explanation for metal-dependent selectivity by relating catalytic behavior to the adsorption energies of reaction intermediates. Density-functional calculations by Peterson and co-workers connected copper's ability to reduce CO_2 beyond CO to the energetics of successive proton–electron transfers [74]. Peterson and Nørskov subsequently developed an adsorption-energy-based activity volcano for methane formation, identifying the protonation of adsorbed CO as a key contributor to the required overpotential [93]. Copper

combines sufficient CO binding to retain this intermediate with relatively weak hydrogen binding, providing a favorable balance for further CO reduction in competition with hydrogen evolution. Silver and gold bind CO more weakly and tend to release it, whereas stronger-binding transition metals can face difficulties converting adsorbed CO and substantial competition from hydrogen evolution. This interpretation helps explain copper's distinctive production of hydrocarbons and alcohols, although CO and H adsorption energies alone do not determine multicarbon selectivity, which also depends on surface coverage, site geometry, and carbon–carbon coupling kinetics [9, 88].

Advances in product analysis further revealed the complexity of copper's reaction network. In 2012, Kuhl and co-workers identified 16 CO_2-reduction products across a range of electrode potentials, demonstrating the importance of sensitive analysis of both gaseous and dissolved products [94]. More recent research combines controlled surface studies with nanostructured and alloyed catalysts, increasingly detailed product analysis, and computational investigations of elementary reaction steps. Spectroscopic measurements and electronic-structure calculations provide complementary information about adsorbed intermediates and possible pathways, although a complete mechanistic description remains unresolved [9, 88]. In parallel, developments in flow cells and membrane-electrode assemblies have made transport, local reaction conditions, and device stability increasingly prominent considerations [95].

These developments have also emphasized the reciprocal relationship between the copper electrode and its operating environment. Electrode potential, electrolyte composition, and adsorbate populations influence both surface reactions and the structure and morphology of the catalyst. Huang and co-workers demonstrated potential-induced nanoclustering of copper nanocubes during CO_2 electroreduction, illustrating that the initially prepared morphology need not remain stable during operation [96]. Reconstruction, dissolution, and redeposition can change the distribution of adsorption environments and modify local transport, with consequences for selectivity, activity, energy efficiency, and long-term stability [89, 97]. Understanding copper-based catalysts therefore requires examining both the behavior of adsorbed intermediates and the evolution of the electrode under operating conditions. The following sections consider these coupled effects, providing the context for the studies of terraces, steps, and substitutional impurity sites in this thesis.

3.2 Reaction Pathways and Product Selectivity

The electrochemical reduction of CO_2 involves a network of reactions in which adsorption, electron transfer, proton transfer, bond cleavage, and carbon–carbon coupling compete at the electrode–electrolyte interface. The resulting products depend on the relative rates of these processes and on the populations of the participating intermediates. Overall reaction thermodynamics alone therefore cannot predict the product distribution. Copper can produce CO and formate, more extensively reduced single-carbon products such as methane, and multicarbon products including ethylene, ethanol, acetate, and propanol. Their relative yields depend on the catalyst structure and the conditions under which it operates [9, 88].

3.2.1 Product Formation and Measures of Selectivity

The products differ in the number of electrons required for their formation. Reduction of one CO_2 molecule to CO or formate requires two electrons, whereas methane formation requires eight. Formation of ethylene or ethanol from two CO_2 molecules requires twelve electrons. These electron counts describe the overall transformations without specifying their elementary steps. Although proton–electron pairs are often used to balance reaction equations, water or other proton donors can supply hydrogen in neutral and alkaline electrolytes [9].

Product selectivity is commonly expressed through the Faradaic efficiency,

$$\mathrm{FE}_i = \frac{n_i F N_i}{Q}, \tag{130}$$

where n_i is the number of electrons required per molecule of product i, F is the Faraday constant, N_i is the amount of that product in moles, and Q is the total charge passed. Under steady operating conditions, the corresponding partial current density is

$$|j_i| = \mathrm{FE}_i\,|j_{\mathrm{tot}}|. \tag{131}$$

Faradaic efficiency and partial current density describe different aspects of performance. A higher Faradaic efficiency can result from suppressing a competing reaction without increasing the formation rate of the desired product. Comparisons between catalysts should therefore consider both quantities. Neither alone determines energy efficiency, which also depends on the operating cell voltage and the overall reaction [95].

3.2.2 Initial Reduction to CO and Formate

Two major branches of CO_2 reduction lead to CO and formate. Pathways toward CO commonly involve a carboxyl intermediate, denoted *COOH, followed by removal of an oxygen-containing group and formation of adsorbed CO, *CO. The initial activation of CO_2 can involve charge transfer and stabilization by the surrounding electrolyte; consequently, a simplified sequence of intermediates should not be interpreted as establishing that every step is a concerted proton–electron transfer [9, 88].

Formate formation on copper can proceed by transfer of surface hydrogen to the carbon atom of CO_2, accompanied by electron transfer from the electrode. This amounts to hydride transfer and produces $HCOO^-$ directly, without an adsorbed *OCHO intermediate along the preferred reaction pathway. The negatively charged electrode then repels the formate anion [98]. The availability of adsorbed hydrogen therefore matters for this pathway. Calculations for silver electrodes show that low hydrogen coverage can suppress direct formate formation, while formation of adsorbed *OCHO through proton–electron transfer (as suggested by Figure 3.2) is kinetically hindered [99]. Under neutral and alkaline conditions, the released product is predominantly formate rather than formic acid. Formate is usually a terminal product under aqueous CO_2-reduction conditions, whereas CO can undergo further reduction on copper [88].

The fate of *CO is closely connected to its binding strength. On weak CO-binding metals such as silver and gold, desorption favors CO as a product. Copper can retain a substantial population of *CO while permitting its subsequent conversion. Stronger adsorption does not necessarily improve performance, however, since it can make further transformation difficult or block sites.

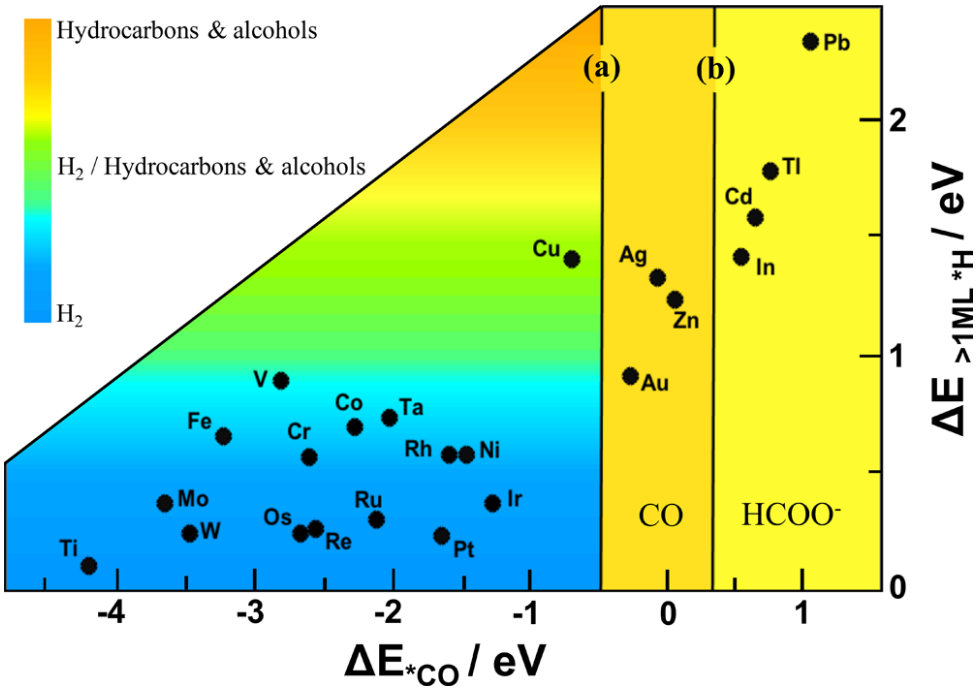

Figure 3.1. Two-descriptor map of metal-electrode selectivity. The horizontal axis represents the adsorption energy of an isolated CO molecule. The vertical axis represents the differential adsorption energy of an on-top H atom above one monolayer coverage. The colored region indicates competition between hydrogen evolution and hydrocarbon/alcohol formation, while the right-hand regions indicate CO and formate production. Reproduced from Hussain et al. [100].

The balance between CO retention, intermediate conversion, and competing hydrogen evolution provides a useful interpretation of metal-dependent selectivity [74, 93, 9].

Hussain and co-workers combined density-functional calculations with rate theory to relate product trends to CO binding and hydrogen adsorption. Their descriptor map in Figure 3.1 uses the adsorption energy of an isolated CO molecule and the differential adsorption energy of an on-top H atom above one monolayer coverage. Within this model, copper combines sufficient CO retention with unfavorable adsorption of the additional hydrogen species associated with hydrogen evolution. The map groups hydrocarbons and alcohols together, and it does not resolve the competition between individual C_1 and C_{2+} products [100].

3.2.3 Further Reduction of CO and Carbon–Carbon Coupling

Adsorbed CO forms a central branching point between pathways toward single-carbon and multicarbon products. Methane requires successive hydrogenation and eventual cleavage of the C–O bond. Proposed pathways include initial formation of *CHO or *COH, with their relative importance depending on surface structure and the treatment of the electrochemical environment. Theoretical studies have established plausible sequences, but the identification of short-lived intermediates and the assignment of rate-controlling steps remain challenging [74, 100, 9, 88].

Multicarbon formation requires a C–C bond to form between carbon-containing intermediates. Coupling of two adsorbed CO molecules to produce an *OCCO-type intermediate is a prominent pathway. Alternative proposals involve coupling CO with a partially hydrogenated species such as *CHO. The accessibility of these routes depends on the availability and arrangement of

neighboring intermediates, their stabilization by the interface, and the barriers to coupling. CO adsorption energies alone therefore cannot establish multicarbon selectivity [9, 88].

After the first C–C bond forms, further reduction can lead to several products. Branching among ethylene, ethanol, and acetate involves competition between hydrogenation, oxygen removal, desorption, and reaction in the adjacent solution. For example, proposed acetate pathways involve desorption of ketene followed by reaction with hydroxide, illustrating how product formation can depend on both surface chemistry and transport away from the electrode [88].

Figure 3.2 presents the reaction network proposed by Seger and co-workers, organizing intermediates according to their carbon content and the cumulative number of electrons transferred from CO_2. It illustrates the branching from adsorbed CO toward methane and multicarbon products and the subsequent competition between hydrocarbon and oxygenate formation. The pathways and rate-controlling steps represent the authors' mechanistic interpretation rather than a universally established sequence. In particular, the C_3 pathways are more speculative than those proposed for C_1 and C_2 products. The detailed coupling pathways and subsequent branching are discussed further in Section 3.5 [88].

3.2.4 Competition with Hydrogen Evolution and the Operating Environment

Hydrogen evolution competes with CO_2 reduction for electrons and, where the pathways share adsorption sites, for surface availability. Copper's hydrogen adsorption properties help explain its favorable position for carbon-containing product formation, but hydrogen evolution remains significant and responds to potential, proton-donor availability, and surface coverage. Adsorbed CO can suppress hydrogen evolution through site blocking and changes in the adsorption environment, linking the competition between these reactions to the evolving CO population [9].

The applied potential changes the driving forces and activation barriers of individual steps, but a more negative potential does not uniformly favor all reduction products. Different branches respond differently to potential, and changes in intermediate coverage can alter which pathways are accessible. Likewise, local pH affects proton-transfer kinetics and CO_2 availability, while electrolyte cations and interfacial water can stabilize intermediates and transition states. These effects extend beyond the pH-dependent shift of the hydrogen reference potential discussed in Chapter 2 [7, 9, 88].

Mass transport further couples operating conditions to selectivity. Consumption of CO_2 and changes in solution composition near the electrode can produce a local environment substantially different from the bulk electrolyte. CO electroreduction is therefore valuable for investigating reactions downstream of *CO, but it does not necessarily reproduce the product distribution of CO_2 electroreduction. Differences in carbonate formation, buffering, and local reactant availability can influence the observed branching even when CO is a shared intermediate [101].

Finally, the distribution of catalytic sites can itself change during operation. Reconstruction, dissolution, and redeposition can modify the exposed facets, defect populations, and electrode morphology, influencing both intrinsic reaction rates and the local transport environment. Product selectivity consequently reflects the interaction between reaction pathways, adsorbate populations, and an evolving catalyst structure [89, 97]. This relationship motivates the closer examination of copper surface structure in the next section.

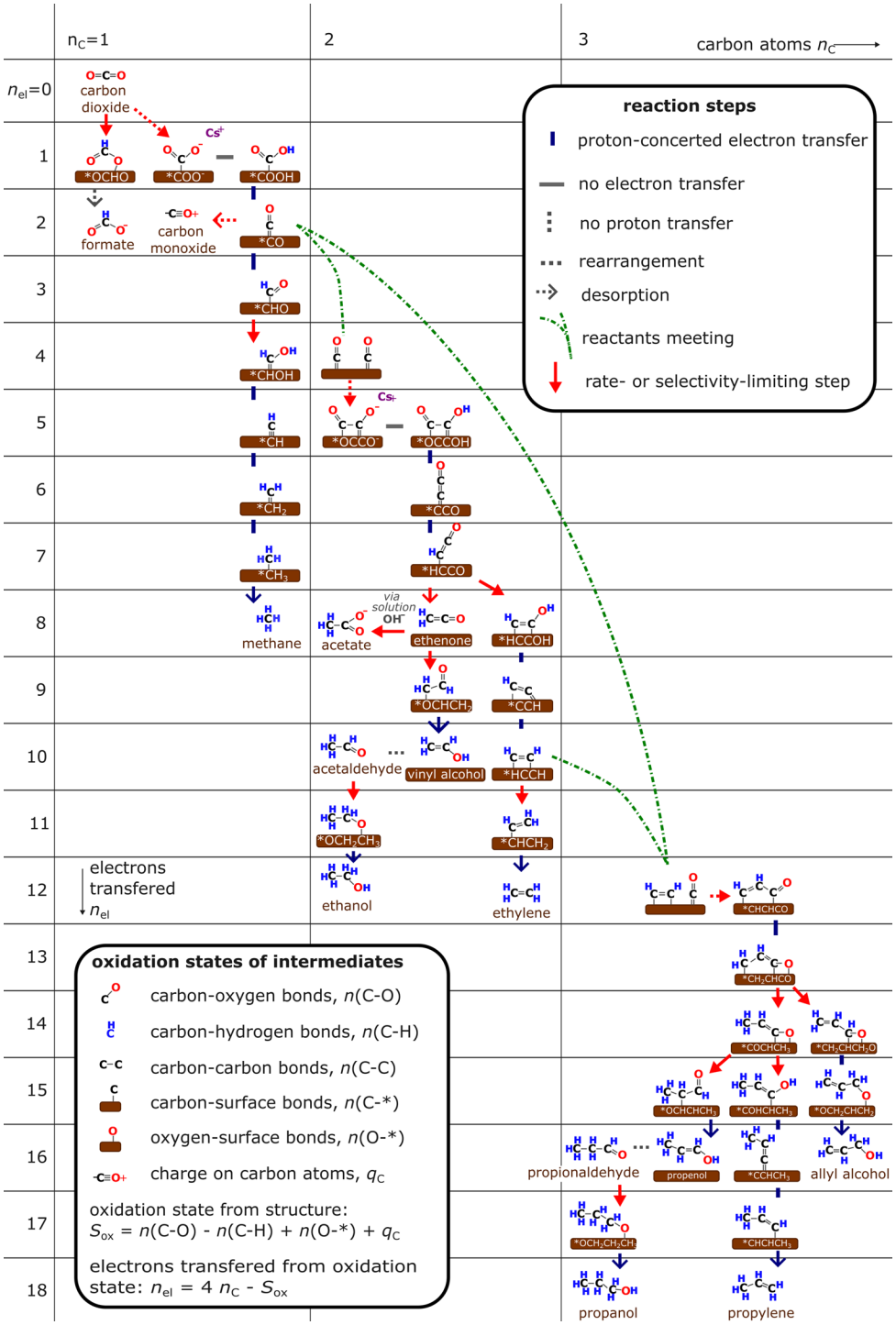

Figure 3.2. Proposed reaction network for CO_2 electroreduction on copper by Seger et al. Columns distinguish the number of carbon atoms, while rows indicate the cumulative number of electrons transferred from CO_2. The asterisk denotes an adsorbed intermediate. Line styles distinguish reaction-step types, and red arrows identify proposed rate- or selectivity-limiting steps. The formate branch differs from the direct hydrogen/electron-transfer pathway discussed in Section 3.2.2. Reproduced from Seger et al. [88].

3.3 Copper Surface Structure and Reactivity

The catalytic behavior of copper depends on the atomic environments exposed at its surface. Terraces, steps, kinks, and grain boundaries differ in their coordination and local geometry, affecting the adsorption of intermediates and the barriers for their conversion. Experiments on single-crystal electrodes demonstrate that these structural differences influence product distributions, while studies of nanostructured copper show that the surface can change substantially during electrocatalysis. Understanding copper's reactivity therefore requires considering both its initial structure and its evolution under operating conditions [8, 102, 14].

3.3.1 Terrace Orientation and Product Selectivity

Copper crystallizes in a fcc structure. Its low-index surfaces expose different atomic arrangements: Cu(111) has a close-packed triangular arrangement, Cu(100) has a square arrangement, and Cu(110) consists of more open atomic rows. These geometries provide different arrangements of neighboring adsorption sites and different local coordination environments. Consequently, intermediates can experience different binding strengths and geometrical constraints during reaction.

Single-crystal electrodes provide a way to investigate these effects experimentally. Hori and co-workers compared CO_2 reduction on several series of copper single crystals and found substantial differences in product distribution. Under their investigated conditions, Cu(100) favored ethylene formation relative to Cu(111), which showed a greater preference for methane. Measurements on stepped surfaces further demonstrated that selectivity depends on the arrangement of terraces and steps, rather than solely on the nominal low-index orientation [8].

The influence of surface orientation is also apparent when CO is supplied directly as the reactant. Schouten and co-workers investigated CO reduction on copper single crystals using online electrochemical mass spectrometry. As illustrated in Figure 3.3, the potential-dependent signals for ethylene and methane differ between the surfaces. On Cu(100), ethylene formation occurs in a potential region where methane formation remains limited, supporting a pathway to ethylene that is distinct from the pathway associated with methane formation. The authors interpreted their observation in terms of two routes to ethylene whose relative importance depends on surface orientation and potential [103].

These experiments connect facet-dependent reactivity to the further reduction of CO, but the association between Cu(100) and ethylene, or Cu(111) and methane, should not be interpreted as an exclusive assignment of a product to a facet. Selectivity also depends on potential, adsorbate coverage, electrolyte composition, and surface preparation. A nominally single-crystal electrode may contain defects or undergo reconstruction, so its measured response need not originate entirely from an ideal terrace [9, 14].

3.3.2 Steps, Defects and Local Atomic Environments

Steps interrupt a terrace and expose atoms with lower coordination than those within the terrace interior. Kinks, vacancies, and grain-boundary intersections introduce further variations. These environments can change the relative stability of adsorbates and transition states, allowing a small population of sites to contribute disproportionately to the overall reaction rate.

A step cannot be described completely by the coordination number of one atom. The terrace

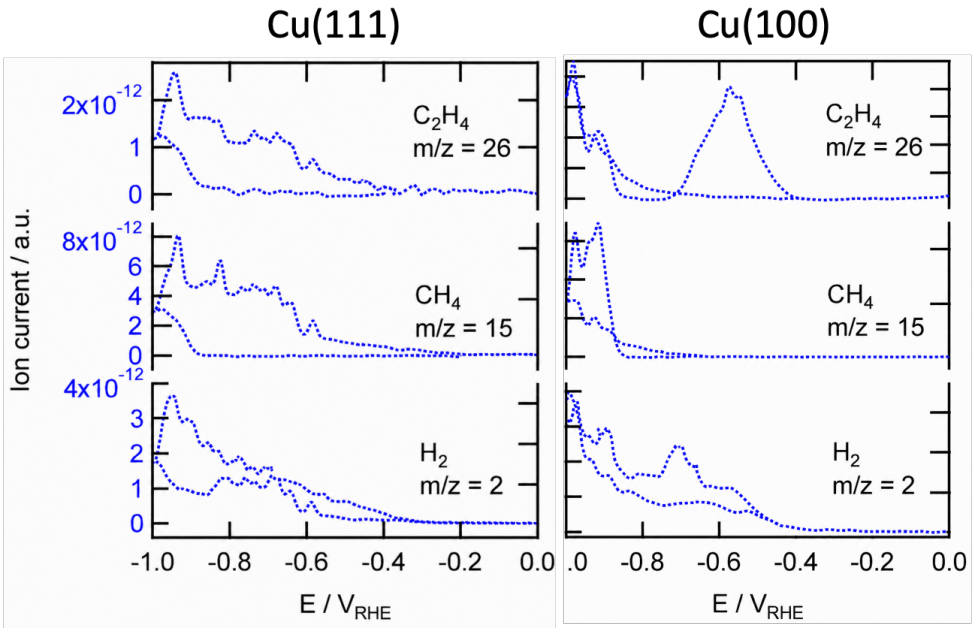

Figure 3.3. Facet-dependent product formation during CO electroreduction on copper single-crystal electrodes. Mass-spectrometric ion-current signals associated with ethylene ($m/z = 26$), methane ($m/z = 15$), and hydrogen ($m/z = 2$) are shown as a function of electrode potential versus RHE. The different potential dependencies illustrate the influence of surface orientation on CO-reduction pathways. Ion currents are shown in arbitrary units and do not directly represent Faradaic efficiencies. Adapted from Schouten et al. [103].

orientation, step direction, microfacet geometry, and step-density determine the surrounding arrangement of adsorption sites. These distinctions are particularly relevant to reactions involving more than one adsorbate, where the separation and orientation of neighboring species influence their ability to react.

Experimental studies establish that these structural differences affect product formation. Hori and co-workers found that product distributions varied across series of surfaces with different terrace widths and step structure [8]. Hahn and co-workers likewise measured differences in oxygenate and hydrocarbon selectivity on copper surfaces with controlled crystallographic orientation, including the high-index Cu(751) surface [104]. Such findings motivate the investigation of specific atomic environments rather than treating all undercoordinated sites as equivalent.

Cheng and co-workers examined this relationship by combining atomistic calculations with experiments on well-defined, UHV-prepared Cu(111) and Cu(100) surfaces. As shown in Figure 3.4, the pristine surfaces predominantly produced hydrogen, whereas stepped surfaces exhibited substantially greater CO2RR activity. The stepped Cu(100) surface favored ethylene more strongly than stepped Cu(111), which predominantly produced methane [14].

The comparison also demonstrates that step density alone is insufficient to explain the product distribution. Intermediate and stepped Cu(100) surfaces had similar step densities but different step arrangements and hydrocarbon selectivities. The accompanying calculations suggested complementary roles for undercoordinated sites, which facilitate CO_2 activation and CO accumulation, and neighboring square arrangements of copper atoms, which favor C–C coupling. Thus, catalytic performance depends on the local arrangement of terrace and defect sites as well

as their abundance [14].

Stronger adsorption at a defect does not automatically imply improved selectivity toward C_{2+} products. A site may retain CO but also favor its hydrogenation, bind another intermediate too strongly, or lack a suitable neighboring site for coupling. Assessing its catalytic role therefore requires considering the energetics of competing processes alongside adsorption strength. For the stepped surfaces examined in this thesis, this motivates comparing CO binding, neighboring adsorption configurations, and the mobility of CO between distinct local environments.

3.3.3 Nanostructure, Roughness, and the Reaction Environment

Nanostructured electrodes contain distributions of terraces, edges, corners, and grain boundaries. Changing particle size or shape alters these distributions, but it can also change the accessible surface area and the transport of reactants and products. Consequently, a difference in measured activity between two morphologies may reflect several effects simultaneously.

Experiments on copper nanoparticles illustrate why increasing the number of undercoordinated atoms is not a universal route to improved CO2RR activity. Reske and co-workers investigated particle-size effects and reported enhanced CO and hydrogen selectivity, together with suppressed hydrocarbon formation, for small copper nanoparticles relative to bulk-like copper [105]. These observations show that structural changes can favor reaction channels other than further CO reduction.

The spatial arrangement of nanoparticles also influences their catalytic response. Mistry and co-workers varied the separation between copper nanoparticles and measured changes in product selectivity, demonstrating that particle size alone is insufficient to characterize a nanoparticle electrode. They interpreted the results in terms of interparticle transport and the re-adsorption of reaction intermediates, connecting selectivity to the environment surrounding neighboring particles [106].

Surface pretreatment provides another means of modifying copper's catalytic behavior. Mistry and co-workers reported an ethylene Faradaic efficiency of approximately 60% on plasma-activated copper, demonstrating that oxidation and subsequent electrochemical treatment can produce surfaces with substantially different product distributions [107]. Such treatments can modify morphology, defect populations, and chemical state simultaneously. Their effects therefore require structural and spectroscopic characterization alongside product measurements.

Rough or porous electrodes also modify the local reaction environment. An increased surface area can raise the current per geometric area, increasing reactant consumption and the generation of local pH gradients. Restricted transport within a porous structure can further change the availability of CO_2 and CO. Apparent morphology-dependent selectivity may consequently contain contributions from both atomic-scale site chemistry and transport [106, 9].

This distinction matters when comparing experiments with calculations. A slab calculation probes a specified atomic environment, whereas an experimental electrode averages over many sites operating within a potentially nonuniform electrolyte. Surface-area normalization and characterization of the reaction conditions help establish which differences can reasonably be attributed to local site chemistry.

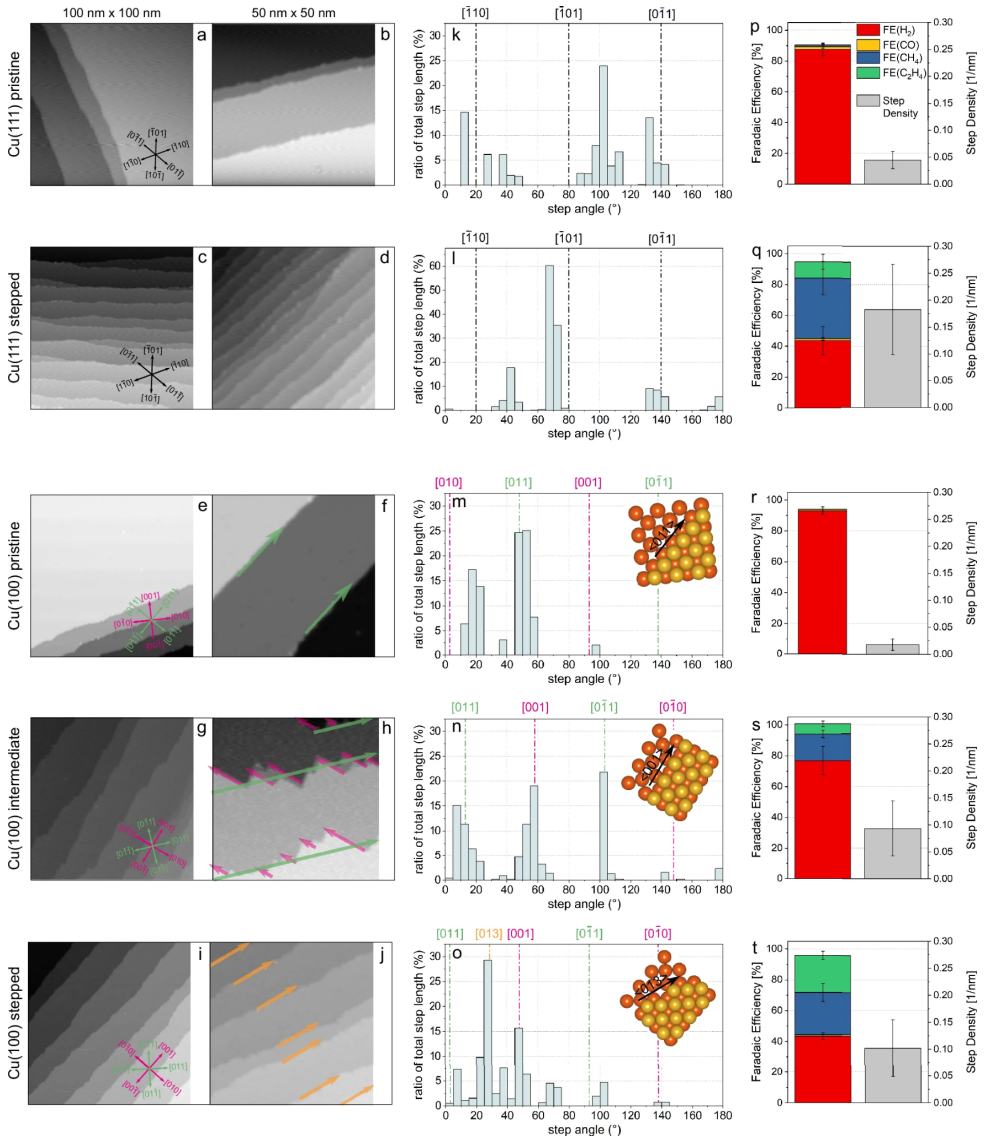

Figure 3.4. (a–j) Low-temperature scanning tunneling microscopy images of pristine and stepped Cu(111), and pristine, intermediate, and stepped Cu(100) surfaces. The modified surfaces were obtained through successive CO_2 electroreduction cycles followed by sputtering and annealing under ultrahigh vacuum. (k–o) Corresponding step orientation distributions, weighted by step length; the insets illustrate prominent step geometries on Cu(100). (p–t) Faradaic efficiencies for gaseous products (colored bars, left axis) and step densities (gray bars, right axis). Electrocatalysis was performed at -1.1 V vs. RHE in 0.1 M $KHCO_3$ for 1 h. Increased step density is associated with greater hydrocarbon selectivity, while differences between the Cu(100) surfaces highlight the additional importance of step geometry. Reproduced from Cheng et al. [14].

3.3.4 Structural Evolution under Operating Conditions

The structure present before electrolysis is not necessarily the structure responsible for the measured catalytic response. Applied potential, adsorbate coverage, and the electrolyte environment can change the relative stability of surface configurations and the pathways through which Cu atoms move. Restructuring can involve rearrangement within the surface, formation of adatoms and nanoclusters, or dissolution and redeposition through the electrolyte. The relative importance of these processes depends on the catalyst, reaction conditions, and potential history [15, 108, 109].

Atomic-scale measurements provide direct evidence of this evolution. Using electrochemical scanning tunneling microscopy, Kim and co-workers observed a sequence of surface transformations on polycrystalline copper at a fixed potential of -0.9 V vs. SHE, when exposed to CO_2. Within the first 30 minutes, the polycrystalline Cu underwent restructuring towards a Cu(111)-like surface structure and over the next 30 minutes towards a Cu(100)-like surface structure [16]. Their observations demonstrate that the exposed electrode surface arrangement evolves during CO2RR.

Changes in copper morphology have been connected experimentally to changes in catalytic performance. Grosse and co-workers followed copper nanocubes with different sizes and supports during CO_2 electroreduction, observing substantial changes in their structure, chemical state, and product selectivity, including loss of the initial cubic morphology [102]. Huang and co-workers identified nanocluster formation followed by aggregation and coalescence during extended electrocatalysis, with grand-potential DFT calculations supporting a role for the applied negative potential in driving the structural changes [96]. These observations show that a morphology selected during synthesis cannot be assumed to persist during operation.

CO can participate directly in this evolution. Amirbeigiarab and co-workers combined in situ scanning tunneling microscopy, surface X-ray diffraction, and Raman spectroscopy to investigate atomic-scale restructuring under CO2RR conditions. Their measurements indicated that the onset of CO formation induces Cu nanocluster formation on initially smooth terraces. The restructuring was kinetically limited and generated undercoordinated copper species that persisted over a wider potential range than that in which the cluster initially formed [15]. Thus, surface structures generated during the initial stages of polarization can influence the catalyst subsequently operating at more negative potentials.

A thermodynamic basis for adsorbate-induced restructuring was proposed by Cheng and co-workers. Their calculations showed that CO adsorption can stabilize stepped and kinked copper terminations relative to planar surfaces under the modeled electrochemical conditions. Strong CO binding at defective environments can therefore favor the creation of additional such environments. This provides a driving force for restructuring, although the structures reached experimentally also depend on the kinetic accessibility of Cu atom rearrangements [14].

Copper transport through the electrolyte provides an additional restructuring mechanism. Vavra and co-workers used online mass spectrometry and UV–visible absorption spectroscopy, including a trapping strategy for short-lived dissolved species, to obtain evidence consistent with transient Cu^+ species mediating dissolution and redeposition during CO_2 reduction. Their DFT calculations identified copper–carbonyl and copper–oxalate complexes as plausible reaction-specific species involved in this process [108]. The experimental evidence supports the participation of dissolved Cu^+, while the specific identities of the native coordination complexes remain

theoretical assignments requiring direct detection. The presence of transient dissolved Cu^{+} also does not, by itself, establish a persistent oxidized active phase on the electrode.

The role of adsorbates extends beyond CO alone. Wei and co-workers combined electrochemical atomic force microscopy, Raman spectroscopy, and grand-canonical modeling to investigate copper restructuring during CO electroreduction. They found that mixed coverage by adsorbed CO and hydroxyls promotes the lifting of surface copper atoms into metastable configurations, producing adatoms and nanoclusters at small cathodic potentials. These changes were accompanied by a more disordered interfacial water network [109].

The stability of the resulting structures depended on CO availability and the balance between CO and hydroxyl coverage. At more negative potentials, the nanoclusters could aggregate or dissolve, while maintaining the CO partial pressure suppressed the subsequent morphological changes. The study further showed that hydroxyl species could remain kinetically trapped on the roughened surface even where their presence would not be predicted from an equilibrium thermodynamic description alone [109]. Adsorbed hydroxyls must therefore be distinguished from dissolved hydroxide: their effects depend on surface occupation and persistence, as well as on the alkalinity of the electrolyte.

Together, these studies indicate that the working copper surface reflects both thermodynamic driving forces and kinetics. CO can stabilize defective environments, hydroxyl coadsorption can facilitate and preserve metastable structures, and dissolved copper complexes can transport material between different locations. These mechanisms need not be mutually exclusive, but their contributions should be established for the particular reaction conditions rather than assumed to be universal.

Structural evolution can consequently change the abundance of adsorption sites, the availability of neighboring sites for coupling, and the competition with hydrogen evolution. It may activate an initially less reactive surface or contribute to the loss of a favorable morphology. Structural stability should therefore be distinguished from performance stability: similar measured currents can be maintained even while the surface structure and distribution of active sites change.

3.3.5 Implications for Atomistic Modeling

Well-defined terrace and step models isolate local environments that are difficult to separate experimentally. Comparing these models can reveal how atomic coordination and neighboring-site geometry affect adsorption and reaction energetics. Their interpretation must account for the possibility that the abundance and accessibility of these environments change during operation.

The Cu(100), Cu(111), and various stepped surfaces considered in this thesis provide a basis for examining these local differences. Particular attention is given to how CO occupies and moves between sites, and how substitutional impurities modify the available adsorption environments. The following section therefore considers CO adsorption, coverage, and surface mobility, connecting the structural features discussed here to the distribution of a central reaction intermediate.

3.4 CO Adsorption, Coverage, and Surface Mobility

Adsorbed CO occupies a central position in the reaction network of CO_2 electroreduction on Cu. Its subsequent conversion depends on the strength and geometry of adsorption, the population of neighboring sites, and its ability to move between different surface environments. These properties connect the atomic structure of the electrode to the local availability of intermediates for hydrogenation and C–C coupling. In situ infrared measurements have directly followed surface-bound CO during CO_2 reduction, providing an experimental basis for examining its population under applied potential [110]

3.4.1 CO–Surface Bonding and Adsorption

The interaction of CO with a metal surface is commonly described using the Blyholder model. Electron donation from the occupied CO 5σ orbital to the metal is accompanied by back-donation from occupied metal states into the CO $2\pi^*$ antibonding orbitals. These interactions contribute to the metal–carbon bond, while occupation of the antibonding orbitals weakens the internal carbon–oxygen bond. This orbital picture provides a qualitative connection between adsorption and changes in the C–O stretching frequency [111].

On an extended metal surface, the molecular orbitals interact with bands of electronic states rather than discrete atomic orbitals. The energies and spatial overlap of these states influence the balance between bonding interactions and repulsion. Consequently, changes in the local electronic structure caused by surface coordination, strain, or alloying can modify CO adsorption even when the molecule retains a similar adsorption geometry [112].

The principal adsorption geometries on Cu include atop, bridge, and hollow sites. At an atop site the C atom binds primarily to one surface atom; bridge and hollow geometries involve coordination to two or more atoms. Terraces and step edges provide different arrangements of these sites, and the coordination of the underlying Cu atoms further modifies their binding properties. Undercoordinated sites can therefore support CO populations that differ from those on neighboring terraces [14].

3.4.2 Adsorption Energetics, the Sabatier Principle, and Volcano Relationships

Adsorption energies provide a useful association between the electronic structure of a catalyst and its reactivity. According to the Sabatier principle, effective catalysis requires an intermediate interaction strength between the surface and the reacting species [113]. If binding is too weak, reactants may not adsorb or become activated sufficiently readily. If binding is too strong, adsorbed intermediates may be difficult to convert or remove, limiting the regeneration of available sites. Catalytic activity therefore depends on balancing the stabilization of intermediates with their participation in subsequent reaction steps [114].

This balance can produce a volcano-shaped relationship when catalytic activity is plotted against an adsorption-energy descriptor. The maximum separates a weak-binding regime, where intermediate formation or surface occupation is unfavorable, from a strong-binding regime, where further conversion or product release is hindered. Quantitative volcano relationships require a reaction model connecting adsorption energetics to elementary rates and surface coverages. Brønsted–Evans–Polanyi relationships, which relate the activation energies to the reaction energies within related families of reactions, provide one route to constructing such models. The

position of the maximum consequently depends on the mechanism and reaction conditions [114].

A widely used electrochemical example is hydrogen evolution. Nørskov and co-workers related exchange-current trends across metal surfaces to the hydrogen adsorption free energy, ΔG_{H^*}. Their model predicts favorable activity near thermoneutral hydrogen adsorption, where the surface can accommodate hydrogen without stabilizing it excessively relative to molecular hydrogen. This illustrates how a calculated adsorption free energy can serve as a descriptor for comparing catalysts [73].

For CO2RR, the larger number of intermediates and competing pathways makes the choice of descriptor more demanding. Peterson and Nørskov used adsorption-energy relationships to analyze trends in CO2RR to methane on transition metals. Their analysis connects copper's favorable behavior to the balance between stabilizing intermediates and enabling their further reduction [93]. Scaling relationships between intermediate adsorption energies can constrain this balance: modifying the binding of one species generally also changes the energies of others. Thermodynamic volcano plots constructed from limiting potentials describe these energetic constraints, but they do not directly predict reaction rates. Activity and product selectivity additionally depend on activation barriers, coverages, and competition between pathways [115].

A kinetic example relevant to multicarbon formation is the CO-dimerization activity map shown in Figure 3.5. Kastlunger constructed this map using a simplified microkinetic model that assumes CO dimerization is the rate-limiting step. Its descriptors are the CO adsorption free energy, ΔG_{*CO}, and the formation free energy of adsorbed OCCO, ΔG_{*OCCO}. Weak CO adsorption limits the surface population available for coupling. On the strong-binding side, the scaling relationship between these descriptors increasingly favors two separate adsorbed CO molecules over the coupled intermediate, raising the dimerization barrier within the model. Copper lies near the favorable region along the transition-metal scaling line. The map therefore illustrates how CO availability and the energetics of C–C bond formation jointly influence the predicted activity [116].

These considerations are particularly relevant when applying CO adsorption energies to copper-based SAAs. The binding energy of the first CO molecule characterizes adsorption at an initially unoccupied impurity, whereas subsequent molecules encounter a site already modified by adsorption. Multiple adsorption can change the electronic properties of the impurity and displace it relative to the copper host [117, 118]. Consequently, the first-CO binding energy alone may not characterize the occupied site. Differential adsorption energies and the stability of the associated surface configurations provide additional information, while reaction-barrier calculations are needed to establish whether the adsorbed molecules can readily undergo C–C coupling.

3.4.3 Coverage Effects and Lateral Interactions

CO adsorption under reaction conditions cannot be described solely by the binding energy of an isolated molecule. The surface population reflects CO formation from CO_2, adsorption from the surrounding electrolyte, desorption, and consumption in subsequent reactions. Surface diffusion redistributes this population between sites. The resulting steady-state coverage need not correspond to adsorption equilibrium with a CO reservoir.

It is also necessary to distinguish average coverage from local occupation. An electrode with a modest average CO coverage may contain more densely populated step edges or other strongly

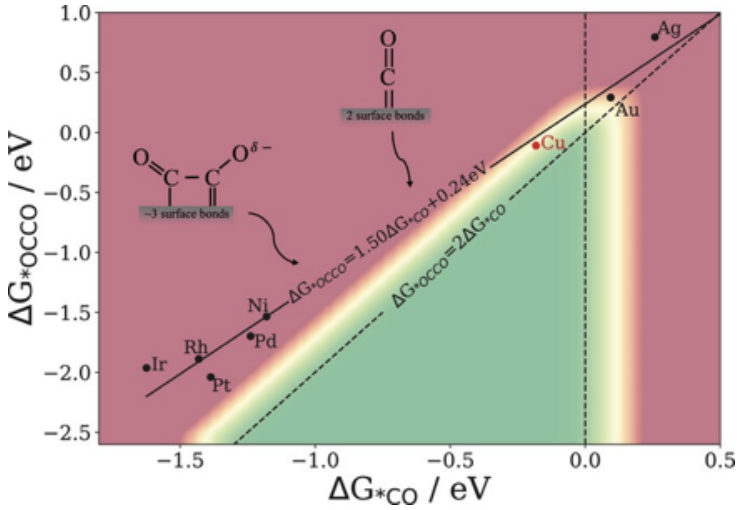

Figure 3.5. Calculated activity map for CO dimerization at $-1\,\mathrm{V}$ *vs. SHE, assuming dimerization is the rate-limiting step. The axes show the CO adsorption free energy,* $\Delta G_{*\mathrm{CO}}$*, and the formation free energy of adsorbed OCCO,* $\Delta G_{*\mathrm{OCCO}}$*. The solid line represents the scaling relationship for the investigated transition-metal (100) surfaces. The vertical dashed line marks thermoneutral CO adsorption, while the diagonal dashed line marks thermoneutral dimerization,* $\Delta G_{*\mathrm{OCCO}} = 2\Delta G_{*\mathrm{CO}}$*. The background shading indicates the activity predicted by the simplified microkinetic model. Reproduced from Kastlunger [116].*

binding regions. Conversely, two surfaces with the same average coverage may differ in the abundance and orientation of neighboring CO pairs. Spectroscopic measurements of surface-bound CO provide access to its response to reaction conditions, but relating an integrated signal to the occupation of specific atomic environments requires additional structural information [110].

As the surface population increases, adsorbed molecules interact with one another. These lateral interactions can include electrostatic contributions associated with adsorption-induced dipoles, changes transmitted through the substrate, and short-range interactions when molecules approach closely. Their net effect depends on separation, orientation, adsorption geometry, and the surrounding surface environment. A single coverage-independent interaction parameter may therefore be insufficient to describe all configurations.

Direct evidence for this complexity comes from time-resolved scanning tunneling microscopy of CO on Cu(111). Measurements showed that molecular mobility depended on both coverage and the positions of nearby molecules, including enhanced diffusion at particular local coverages and repulsion at short separations [119]. Later experiments identified a three-body contribution to diffusion that could not be represented solely by adding pairwise interactions [120]. These measurements were performed at low temperatures under surface-science conditions; they established the importance of local adsorbate configurations without directly determining the corresponding interactions at an electrochemical interface.

Coverage also affects the energetics of subsequent reactions. Sandberg et al. calculated CO–CO coupling on Cu(100), Cu(111), and Cu(211), examining the combined effects of coverage, strain, and interfacial fields. Within their models, increasing CO coverage lowered the coupling barrier, while the facet and cation-induced field also influenced its magnitude [121]. Coverage can therefore affect both the availability of neighboring reactants and the energy required for them to

react.

3.4.4 CO Diffusion on Terraces and Steps

Surface diffusion allows CO to move between adsorption sites and connects regions where it forms, accumulates, and reacts. The barrier for an individual hop is the energy difference between the occupied configuration and the transition state.

For terrace and step sites connected through the same transition state, stronger binding at the step produces a larger barrier for escape than for arrival. Motion along the step follows a different pathway and must be evaluated separately. Comparing these barriers helps establish whether CO can accumulate at steps while remaining mobile along them. The adsorption energies and minimum-energy paths presented in Publication III address this question.

3.5 C–C Coupling and Multicarbon Products

The formation of C_{2+} products requires the formation of a C–C bond between intermediates derived from CO_2. On Cu, adsorbed CO provides a starting point for several proposed coupling pathways. Its local availability is therefore important, but the presence of neighboring CO molecules alone does not establish whether coupling is kinetically accessible. The relative arrangement of adsorption sites and the stabilization of the coupling transition state must also be considered. Furthermore, forming the first C–C bond does not uniquely determine the final product, which depends on subsequent hydrogenation, deoxygenation, and desorption steps.

A widely investigated pathway begins with the coupling of two adsorbed CO molecules to form an OCCO intermediate. This mechanism connects the CO populations discussed in the preceding section to the formation of a two-carbon reaction intermediate. Calculations by Montoya et al. identified a CO dimer configuration stabilized by a charged interfacial water layer on Cu(100) and Cu(111). Without that environment, dimer formation was substantially less favorable within their model. Their results demonstrated that the feasibility of coupling cannot be assessed solely from the interaction of CO with an uncharged surface in vacuum [122].

Experimental support for a dimer-derived pathway was provided by Pérez-Gallent et al., who observed infrared bands assigned to a hydrogenated CO dimer, OCCOH, during CO reduction on Cu(100) in LiOH electrolyte at low overpotentials. This assignment supports the involvement of a coupled intermediate under the investigated conditions, it does not, by itself, establish the complete sequence of preceding elementary steps or demonstrate that the same pathway dominates on every copper surface [123].

Alternative mechanisms involve hydrogenation before C–C bond formation. For example, adsorbed CO can react with a formyl intermediate, CHO, rather than with a second unhydrogenated CO molecule. Goodpaster et al. examined competing pathways on Cu(100) using a computational model incorporating electrode potential, solvent, and electrolyte effects. Their results identified conditions favoring CO dimerization and others favoring coupling between CO and CHO, illustrating that the preferred route can change with the electrochemical environment [124]. CO hydrogenation can consequently contribute either to continued one-carbon reduction or to the formation of a reactant for C-C coupling.

The competition between these routes depends on both their activation barriers and the popula-

tions of the participating intermediates. A low coupling barrier has limited catalytic significance if one of its reactants is rarely present. Conversely, a substantial CO population may promote coupling by increasing the availability of neighboring molecules and modifying their reaction energetics. Calculations comparing Cu(100), Cu(111), and Cu(211) have shown that coverage and cation-induced electric fields influence CO dimerization barriers, alongside the geometry of the Cu surface [121]. These findings connect coupling to the local adsorption environment without establishing a universal relationship between stronger CO binding and greater C_{2+} selectivity.

After the first C–C bond forms, several competing sequences of hydrogenation and oxygen removal become possible. Pathways leading to ethylene ultimately remove both oxygen atoms inherited from the two CO molecules, whereas ethanol formation retains one oxygen atom. The selectivity between these products therefore involves the relative rates of later elementary steps as well as the initial coupling event. A catalyst that facilitates C–C bond formation need not favor all C_2 products equally.

Experiments on oxide-derived copper provide evidence for intermediates downstream of coupling. Bertheussen et al. identified acetaldehyde during CO electroreduction and presented evidence supporting its role as an intermediate in ethanol formation [125]. This result connects the measured formation of a soluble product to a proposed reaction sequence and illustrates how product analysis can complement spectroscopy of adsorbed species.

Acetate formation further demonstrates that selectivity can depend on reactions beyond the electrode surface. Heenen et al. developed a mechanism in which ketene leaves the surface and reacts with hydroxide in solution to form acetate. Competition between this solution reaction and ketene readsorption links acetate selectivity to local pH, transport, and catalyst roughness [126]. In this description, product branching cannot be understood from surface reaction barriers alone.

Formation of products containing three or more carbon atoms requires additional C–C bond formation. Proposed routes include coupling between a single-carbon intermediate and an already formed C_2 species. Their feasibility depends on the simultaneous availability of both reactants and on whether the larger intermediate can remain adsorbed in a suitable configuration. The detailed pathways remain less firmly established than the principal C_2 routes and should therefore be presented as proposed mechanisms rather than as a unique sequence [88].

For the systems considered in this thesis, these mechanisms motivate examining whether terraces, steps, and substitutional impurities provide suitable environments for multiple CO adsorption and subsequent reaction. Stabilizing several CO molecules near one another is a relevant starting point, but adsorption energies alone cannot establish catalytic activity. The arrangement of the adsorbates, their mobility, and the barriers for coupling and competing reactions determine whether that local population can contribute to C_{2+} production. The following section considers how substitutional impurities modify these properties in copper-based SAAs.

3.6 Substitutional Impurities and Copper-Based Single-Atom Alloys

Introducing a second metal into Cu provides a means of modifying its local adsorption and reaction properties. In a SAA, atoms of a minority element are dispersed individually within a

metallic host, creating chemically distinct sites surrounded by host atoms. For Cu-based SAAs, this arrangement allows the properties of an impurity to be combined with those of neighboring Cu sites. Recent reviews identify this approach as a route for tuning intermediate binding and reaction selectivity in CO_2RR [11, 127, 128].

An early experimental demonstration of complementary impurity and host functions was provided by Kyriakou et al. Isolated Pd atoms in a Cu surface facilitated hydrogen dissociation, while the surrounding Cu accommodated the resulting hydrogen more weakly, enabling selective hydrogenation [129]. Although this example concerns thermal catalysis, it illustrates how different elementary steps can occur at different parts of an alloy surface. Extending this concept to electrocatalysis requires considering how electrode potential, solvent, and adsorbate populations influence both reactivity and the structure of the alloy [130].

3.6.1 Local Electronic Structure and Adsorption

Replacing a Cu atom with another transition metal changes the electronic states available for bonding and the geometry of the surrounding adsorption environment. The effect depends on the impurity's identity, its coordination to Cu, and its interaction with adsorbates. Alloying can therefore modify intermediate binding directly at the impurity and at nearby host sites, influencing the competition between CO_2RR pathways and hydrogen evolution [131, 128].

The electronic structure of an isolated impurity can differ substantially from that of the corresponding pure metal. Greiner et al. demonstrated that dilute Cu atoms in an Ag host can exhibit narrow, free-atom-like d-states when coupling to the host is sufficiently weak [132]. Although that study concerns a silver host, it establishes why adsorption descriptors derived from extended metal surfaces need not transfer directly to isolated alloy sites. The extent of electronic localization depends on the particular impurity–host combination.

For CO, these changes affect the donation and back-donation interactions discussed in the preceding section. Local structural relaxation also modifies orbital overlap and the accessible adsorption geometries. The same impurity can consequently display different adsorption properties on Cu(100), Cu(111), and a step edge, where its coordination and geometric freedom to relax differ.

Atomic isolation of the impurity does not restrict a reaction to that atom alone. An intermediate may bind to the impurity while another occupies a neighboring Cu site, allowing the surrounding host to participate in the reaction. The relevant catalytic environment therefore includes both the isolated atom and the local arrangement of Cu atoms. This distinction is particularly useful when considering C–C coupling, which requires two C-species to approach in a suitable geometry.

3.6.2 Multiple CO Adsorption at an Isolated Impurity

An isolated impurity is not necessarily limited to binding one CO molecule. Direct experimental evidence was provided by Wang et al., who identified dicarbonyl species at isolated Rh sites on a RhCu(100) SAA. Their combined surface-science and DFT study distinguished configurations containing one and two CO molecules bound to the same Rh atom and demonstrated that their populations could be changed by varying temperature and CO pressure [12]. This establishes multiple adsorption at a metallic alloy site, although the measurements were performed under controlled CO exposure rather than electrochemical reaction conditions.

Broader computational support was provided by Berger et al., who examined coadsorption at

impurity sites in several SAAs, including Cu hosts with Cu(111) terraces and Cu(211) steps. They found that adsorption of two species at the same impurity can be more favorable than separating them between impurity and host sites. Their results show that local coadsorption can be favored across a range of adsorbates and alloy compositions, rather than being restricted to the RhCu dicarbonyl example [133].

The calculations presented in this thesis similarly showed that several CO molecules can bind to first-row transition-metal substituents in copper [117]. Subsequent work extended the investigation of multiple adsorption using BEEF-vdW and compared additional impurity elements and surface environments [118]. Together with the experimental and theoretical studies above, these findings motivate treating the occupation of an impurity as a variable when characterizing its adsorption properties.

The binding of additional CO molecules rarely resemble that of the first CO. Differential adsorption energies quantify the binding of each additional molecule, while comparisons between occupation states require a consistent CO reference. These quantities help establish how many molecules an impurity can accommodate and whether they preferentially bind there rather than on the surrounding copper.

3.6.3 Adsorbate-Induced Redistribution and Structural Stability

The structure of a SAA can change when adsorbates alter the relative stability of impurity environments. Relevant transformations include segregation between the bulk and surface, redistribution between terraces and steps, aggregation of isolated impurities, and displacement of an impurity from its original substitutional position. Each changes the local coordination in a different way, so evidence for one transformation should not automatically be taken as evidence for the others.

Experimental evidence for CO-induced redistribution in a Cu-based SAA was reported by Simonovis et al. Using ambient-pressure X-ray photoelectron spectroscopy on Pt/Cu(111), they observed a small increase in Pt surface segregation upon CO exposure at room temperature [134]. This demonstrates that CO can influence the location of the minority metal. It does not, by itself, establish extensive surface roughening or aggregation.

Darby et al. examined the distinction between segregation and aggregation computationally for dilute alloys with Cu, Ag, and Au hosts. CO favored impurity segregation into the surface layer in the systems studied, whereas its effect on aggregation depended on alloy composition and coverage [135]. Thus, stronger adsorption at an impurity may help retain that element at the surface without necessarily preserving its atomic isolation.

For an impurity on stepped copper, adsorption introduces a competition between the energy required to relocate the atom and the binding energy gained in the new environment. If CO binds more favorably at an edge impurity, increasing its occupation may shift the relative stability of terrace and step configurations. Conversely, an unfavorable relocation energy may outweigh the adsorption benefit. Establishing a preference therefore requires comparing the complete adsorbate–alloy structures at consistent composition and electrochemical conditions.

Thermodynamic preference must also be distinguished from the rate at which a structural change occurs. Migration and aggregation require accessible atomic pathways, and a configuration may persist because the barriers to redistribution are large. Adsorption can modify both the relative

energies of configurations and the barriers connecting them. The structure observed during operation can consequently depend on electrode preparation and reaction history as well as the instantaneous conditions.

These considerations connect local adsorption chemistry to the persistence of the proposed catalytic site. An impurity selected for its CO binding properties must also be assessed at the occupations and coordination environments it can adopt. This motivates the comparisons of pure Cu, substitutional impurities, and step-edge environments developed in this thesis, with the detailed findings presented in the following chapter.

3.7 Open Questions and Connection to This Thesis

The preceding sections identify a close connection between CO adsorption, the atomic structure of copper, and the reaction environment. Understanding this connection requires determining both the properties of individual adsorption sites and the conditions under which those sites are populated and structurally stable. These considerations motivate the investigations of copper terraces, steps, and substitutional impurities presented in this thesis.

A first question concerns the propensity of individual substitutional atoms to adsorb multiple CO molecules. Experimental identification of dicarbonyls on RhCu(100) and computational predictions of coadsorption show that an isolated impurity can accommodate more than one molecule [12, 133]. How many CO molecules can individual transition-metal atoms in Cu(100) and Cu(111) adsorb more strongly than the surrounding copper, and how do their differential binding energies depend on the element? Addressing this question requires comparing consecutive adsorption across different impurity elements, together with the associated structures and magnetic properties. The sensitivity of these trends to the treatment of exchange and correlation, including dispersion interactions, must also be considered.

A second question concerns the occupation of isolated impurity sites. Experimental identification of dicarbonyls on RhCu(100) and computational predictions of co-adsorption show that a single substitutional transition-metal atom can accommodate more than one CO molecule [12, 133]. This raises the question of how multiple adsorption changes local bonding and geometry across different impurity elements. It also motivates examining the sensitivity of these trends to the treatment of exchange and correlation, including dispersion interactions.

A third question is whether the preferred location of an impurity remains unchanged as CO adsorbs. The stability of an impurity on a terrace or at a step reflects a balance between its interaction with the copper host and the stabilization provided by the adsorbates. Comparing these environments at different CO occupations can reveal whether adsorption favors redistribution and whether trends obtained for clean alloy surfaces remain applicable to adsorbate-covered structures.

The studies collected in this thesis address these questions through atomistic calculations of adsorption, structural energetics, and selected migration pathways. Pure copper provides a reference for separating the influence of surface geometry from the additional effects introduced by substitutional impurities. Comparisons across impurity elements and CO occupations then establish how composition and local coordination jointly affect the available adsorption environments.

These investigations provide a basis for interpreting the accumulation and redistribution of CO on copper-based catalysts. Connecting these properties quantitatively to product selectivity additionally requires reaction barriers, competing adsorbate populations, and the kinetics of the wider reaction network. The following chapter summarizes the original articles and explains how their findings contribute to the questions outlined here.

4 Summary of Publications

4.1 Publication I

"Single-Atom Substituents in Copper Surfaces May Adsorb Multiple CO Molecules"

J. Phys. Chem. Lett. 30 May 2024; 15 (21): 5654–5658.

The first publication was a letter addressing the possibility of multiple CO adsorption to substitutional transition-metal atoms in copper surfaces. The motivation was the common use of the binding energy of a single CO molecule as a descriptor in computational searches for improved CO_2 catalysts [136], despite experimental observations of more than one CO molecule adsorbing to isolated Rh [12] and Co [13] atoms in copper surfaces.

We examined the capacity of substitutional 3d transition-metal atoms in Cu(100) and Cu(111) to adsorb multiple CO molecules, comparing the differential binding energies and the structural and electronic properties of the resulting transition-metal multi-carbonyl configurations. Spin-polarized DFT calculations were carried out using the RPBE functional [28], the PAW method [38], and a plane-wave basis in VASP [137, 138]. Cu atoms in the surface layer of Cu(100) and Cu(111) were replaced by 3d transition-metal atoms (Sc–Ni), and structures with different numbers of adsorbed CO molecules were optimized to determine the maximum number of adsorbed CO molecules for each substitutional atom. Differential binding energies were calculated for each additional molecule and compared with CO adsorption on the corresponding pure copper surface to determine whether adsorption at the impurity was energetically preferred. The outward displacement of the substitutional atom, the total magnetic moment, and the redistribution of electrons estimated by Bader analysis were also presented.

Publication I establishes that several CO molecules can bind to an individual substitutional transition-metal atom more strongly than to the surrounding copper surface. The differential binding energy generally decreases with subsequent CO adsorption, but can increase when adsorption is accompanied by a reduction in magnetic moment. The optimized carbonyl configurations also show outward displacement of the substitutional atom. These results establish the need to consider multiple CO adsorption and the resulting carbonyl configurations when characterizing substitutional sites [117].

Further information about the calculations, not presented in the article, is given below. The optimized structures and tabulated results provide a more detailed comparison of multiple CO adsorption across the substitutional elements.

Figures 4.1 and 4.2 present the optimized structures of the Cu(100) and Cu(111) slabs as 1–4 CO molecules adsorb to the transition-metal atoms of the SAAs. Tables 4.1 and 4.2 present the exact numbers of the differential binding energies, outward displacements, magnetic moments, and Bader charges.

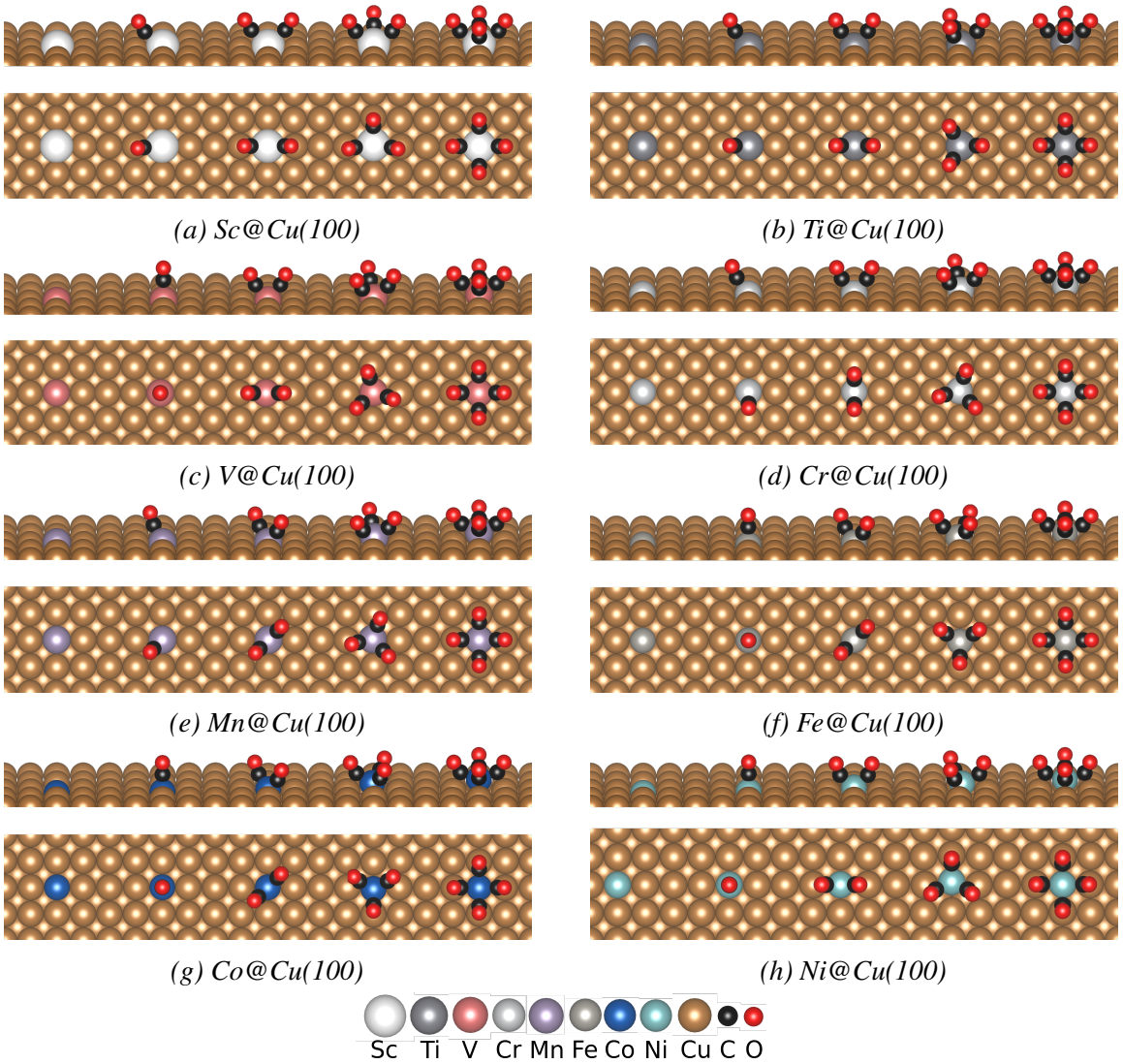

Figure 4.1. Minimum energy structures of (a) Sc, (b) Ti, (c) V, (d) Cr, (e) Mn, (f) Fe, (g) Co and (h) Ni on the Cu(100) surfaces with 0-4 CO molecules adsorbed to the substituent atom

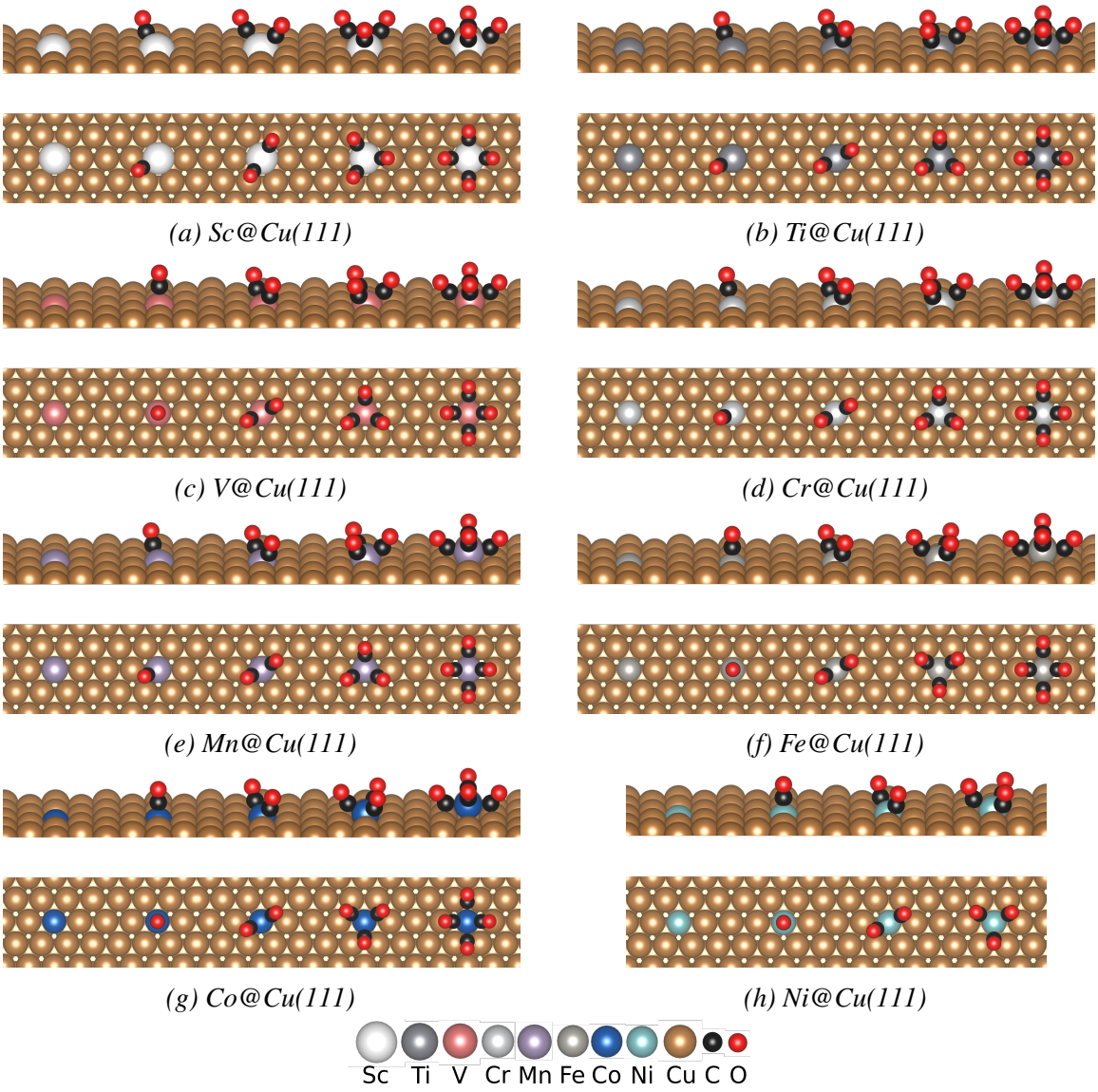

Figure 4.2. Minimum energy structures of (a) Sc, (b) Ti, (c) V, (d) Cr, (e) Mn, (f) Fe, (g) Co and (h) Ni on the Cu(111) surfaces with 0-4 CO molecules adsorbed to the substituent atom

M	#CO	$E_{\text{b-n}^{\text{th}}\text{CO/M@Cu(100)}}$	z_M	magmom	Δq_M	$\Delta q_{\text{Cu,1st}}$	Δq_{CO}
Sc	0	–	0.414 Å	0.000	1.297 e	-0.861 e	–
	1	0.779 eV	0.496 Å	0.000	1.361 e	-0.604 e	-0.406 e
	2	0.747 eV	0.486 Å	0.000	1.386 e	-0.513 e	-0.697 e
	3	0.814 eV	0.565 Å	0.000	1.393 e	-0.167 e	-1.023 e
	4	0.770 eV	0.679 Å	0.000	1.402 e	0.098 e	-1.296 e
Ti	0	–	0.190 Å	1.261	1.025 e	-0.702 e	–
	1	1.154 eV	0.276 Å	1.130	1.162 e	-0.474 e	-0.448 e
	2	1.255 eV	0.272 Å	0.000	1.184 e	-0.221 e	-0.776 e
	3	1.163 eV	0.444 Å	0.000	1.242 e	-0.005 e	-1.178 e
	4	0.691 eV	0.740 Å	0.000	1.206 e	0.177 e	-1.387 e
V	0	–	0.189 Å	3.368	0.762 e	-0.551 e	–
	1	1.273 eV	0.233 Å	3.482	0.899 e	-0.394 e	-0.314 e
	2	1.347 eV	0.285 Å	1.608	0.957 e	-0.085 e	-0.805 e
	3	1.378 eV	0.460 Å	0.000	1.052 e	0.111 e	-1.292 e
	4	0.615 eV	0.894 Å	0.000	1.036 e	0.169 e	-1.422 e
Cr	0	–	0.225 Å	4.579	0.591 e	-0.434 e	–
	1	0.916 eV	0.241 Å	3.822	0.746 e	-0.229 e	-0.377 e
	2	1.144 eV	0.274 Å	1.783	0.756 e	0.024 e	-0.766 e
	3	1.370 eV	0.545 Å	0.000	0.842 e	0.237 e	-1.261 e
	4	0.525 eV	1.064 Å	0.000	0.850 e	0.200 e	-1.346 e
Mn	0	–	0.188 Å	4.530	0.576 e	-0.433 e	–
	1	0.773 eV	0.196 Å	3.452	0.631 e	-0.125 e	-0.471 e
	2	1.203 eV	0.213 Å	0.725	0.550 e	0.197 e	-0.911 e
	3	1.276 eV	0.674 Å	0.000	0.651 e	0.265 e	-1.170 e
	4	0.238 eV	1.210 Å	0.000	0.663 e	0.421 e	-1.201 e
Fe	0	–	0.035 Å	3.406	0.307 e	-0.289 e	–
	1	1.477 eV	0.051 Å	1.607	0.337 e	-0.035 e	-0.369 e
	2	1.305 eV	0.235 Å	0.003	0.377 e	0.270 e	-0.863 e
	3	1.123 eV	0.801 Å	0.000	0.489 e	0.237 e	-1.046 e
	4	-0.220 eV	1.310 Å	0.000	0.578 e	0.466 e	-1.100 e
Co	0	–	-0.120 Å	0.002	-0.086 e	-0.138 e	–
	1	2.134 eV	-0.002 Å	0.001	0.164 e	0.060 e	-0.376 e
	2	1.193 eV	0.274 Å	0.000	0.262 e	0.305 e	-0.793 e
	3	0.774 eV	0.887 Å	0.000	0.401 e	0.274 e	-0.926 e
	4	-0.483 eV	1.256 Å	0.000	0.505 e	0.406 e	-1.102 e
Ni	0	–	-0.097 Å	0.000	-0.133 e	-0.076 e	–
	1	1.500 eV	0.078 Å	0.000	0.121 e	0.065 e	-0.286 e
	2	0.745 eV	0.459 Å	0.000	0.246 e	0.232 e	-0.588 e
	3	0.340 eV	0.891 Å	0.000	0.397 e	0.315 e	-0.848 e
	4	-0.236 eV	1.311 Å	0.000	0.465 e	0.465 e	-1.068 e

Table 4.1. Binding energy, outward displacement and magnetic moment in units of unpaired electrons for substituent atoms, M, on the Cu(100) surface with up to 4 CO molecules adsorbed. The change in partial Bader charges of the M atom, the first neighbouring Cu atoms in the surface layer and of the CO molecule.

M	#CO	$E_{\text{b-n}^{\text{th}}\text{CO/M@Cu(111)}}$	z_M	magmom	Δq_M	$\Delta q_{\text{Cu,1st}}$	Δq_{CO}
Sc	0	–	0.399 Å	0.000	1.301 e	-1.167 e	–
	1	0.722 eV	0.371 Å	0.000	1.342 e	-0.723 e	-0.495 e
	2	0.638 eV	0.430 Å	0.000	1.370 e	-0.615 e	-0.648 e
	3	0.743 eV	0.494 Å	0.000	1.355 e	-0.374 e	-0.966 e
	4	0.392 eV	0.661 Å	0.000	1.383 e	-0.013 e	-1.383 e
Ti	0	–	0.108 Å	1.041	1.037 e	-0.953 e	–
	1	1.146 eV	0.164 Å	0.000	1.160 e	-0.585 e	-0.516 e
	2	1.177 eV	0.158 Å	0.000	1.203 e	-0.310 e	-0.874 e
	3	1.094 eV	0.322 Å	0.000	1.205 e	0.021 e	-1.235 e
	4	0.386 eV	0.721 Å	0.000	1.297 e	0.106 e	-1.557 e
V	0	–	0.108 Å	3.022	0.737 e	-0.758 e	–
	1	1.228 eV	0.152 Å	2.842	0.830 e	-0.589 e	-0.260 e
	2	1.394 eV	0.127 Å	0.251	0.973 e	-0.049 e	-0.962 e
	3	1.375 eV	0.390 Å	0.000	1.017 e	0.162 e	-1.303 e
	4	0.304 eV	0.883 Å	0.000	1.107 e	0.229 e	-1.595 e
Cr	0	–	0.152 Å	4.109	0.578 e	-0.634 e	–
	1	0.928 eV	0.153 Å	3.476	0.709 e	-0.390 e	-0.372 e
	2	1.208 eV	0.171 Å	1.275	0.755 e	0.111 e	-0.938 e
	3	1.354 eV	0.483 Å	0.000	0.818 e	0.258 e	-1.280 e
	4	0.126 eV	1.089 Å	0.000	0.922 e	0.275 e	-1.514 e
Mn	0	–	0.150 Å	4.273	0.547 e	-0.606 e	–
	1	0.809 eV	0.134 Å	3.160	0.592 e	-0.220 e	-0.472 e
	2	1.197 eV	0.203 Å	0.492	0.527 e	0.261 e	-0.907 e
	3	1.243 eV	0.603 Å	0.000	0.603 e	0.309 e	-1.177 e
	4	-0.085 eV	1.319 Å	0.000	0.718 e	0.468 e	-1.376 e
Fe	0	–	-0.025 Å	2.895	0.278 e	-0.341 e	–
	1	1.423 eV	0.003 Å	1.552	0.308 e	-0.121 e	-0.369 e
	2	1.299 eV	0.252 Å	0.000	0.357 e	0.331 e	-0.845 e
	3	1.002 eV	0.681 Å	0.000	0.485 e	0.370 e	-1.121 e
	4	-0.346 eV	1.457 Å	0.000	0.567 e	0.531 e	-1.264 e
Co	0	–	-0.119 Å	0.000	-0.061 e	-0.088 e	–
	1	1.962 eV	0.024 Å	0.000	0.118 e	0.145 e	-0.332 e
	2	1.110 eV	0.328 Å	0.000	0.256 e	0.361 e	-0.773 e
	3	0.629 eV	0.736 Å	0.000	0.399 e	0.496 e	-1.027 e
	4	-0.568 eV	1.538 Å	0.000	0.526 e	0.561 e	-1.212 e
Ni	0	–	-0.092 Å	0.000	-0.114 e	-0.028 e	–
	1	1.381 eV	0.069 Å	0.000	0.002 e	-0.057 e	-0.190 e
	2	0.673 eV	0.320 Å	0.000	0.239 e	0.369 e	-0.737 e
	3	0.268 eV	0.612 Å	0.000	0.368 e	0.628 e	-1.067 e

Table 4.2. Binding energy, outward displacement and magnetic moment in units of unpaired electrons for substituent atoms M on the Cu(111) surface with up to 4 CO molecules adsorbed. The change in partial Bader charges of the M atom, the first neighbouring Cu atoms in the surface layer and of the CO molecule.

4.2 Publication II

"Multiple Adsorption of CO Molecules on Transition Metal Substitutional Impurities in Copper Surfaces"

ChemCatChem 17, no. 18 (2025): e00765.

Publication II extends the investigation to second-row transition-metal atoms and examines the importance of dispersion interactions for multiple CO adsorption. The aim was to establish how broadly the adsorption patterns identified in Publication I apply and whether calculated C–O stretching frequencies could help identify the resulting carbonyl configurations experimentally.

Spin-polarized DFT calculations were performed using the BEEF-vdW functional [33], together with the PAW method [38, 39] and a plane-wave basis in VASP [137, 138]. First-row (Sc–Ni) and second-row (Y–Pd) transition-metal atoms were substituted for a single Cu atom in Cu(100) and Cu(111) surface layer, and structures with different numbers of adsorbed CO molecules were optimized to determine the maximum number of CO molecules adsorbed by each substitutional atom. The paper presents the differential binding energies for multiple CO adsorption, together with the impurity displacements, and magnetic moments. The binding energy is compared to the CO adsorption on the corresponding pure copper surface and is used to establish whether additional CO admolecules preferentially bind to the substitutional atom. Harmonic C–O stretching frequencies were also calculated for selected substitutional atoms and compared with available experimental measurements to assess possible signatures of multiple adsorption.

Publication II shows that multiple CO adsorption is relevant across both rows of transition metals and that dispersion contributes significantly to the binding of additional adsorbed CO molecules. For some minimum-energy configurations, the transition-metal atom is displaced from its lattice site, forming a carbonyl complex on the copper surface and leaving a vacancy. These structures suggest a possible degradation mechanism, although they are higher in potential energy than configurations in which CO adsorbs on the surrounding copper surface. The calculated C–O stretching frequencies provide possible experimental signatures, although similar configurations can be difficult to distinguish. Together, these results extend the description of adsorption capacity and motivate examining the preferred locations of carbonyl complexes beyond flat terraces [118].

Further information about the calculations, not presented in the article, is given below. The optimized structures and tabulated results provide a more detailed comparison of multiple CO adsorption across the substitutional elements.

Tables 4.3–4.6 report the differential binding energies, dispersion contributions, outward displacements, and magnetic moments for the investigated carbonyl configurations on Cu(100) and Cu(111).

M	#CO	$E_{\text{b-n}^{\text{th}}\text{CO/M@Cu(100)}}$	E_{vdW}	z_M	magmom
Sc	0	–	–	0.353 Å	0.000
	1	0.905 eV	0.349 eV	0.421 Å	0.000
	2	0.897 eV	0.355 eV	0.418 Å	0.000
	3	0.933 eV	0.512 eV	0.482 Å	0.000
	4	0.908 eV	0.546 eV	0.624 Å	0.000
Ti	0	–	–	0.112 Å	0.010
	1	1.304 eV	0.414 eV	0.209 Å	0.000
	2	1.377 eV	0.412 eV	0.223 Å	0.000
	3	1.307 eV	0.522 eV	0.402 Å	0.000
	4	0.856 eV	0.561 eV	0.673 Å	0.000
V	0	–	–	0.186 Å	2.850
	1	1.326 eV	0.317 eV	0.218 Å	2.560
	2	1.397 eV	0.615 eV	0.254 Å	1.550
	3	1.518 eV	0.614 eV	0.412 Å	0.000
	4	0.716 eV	0.454 eV	0.812 Å	0.000
Cr	0	–	–	0.222 Å	3.970
	1	0.957 eV	0.434 eV	0.221 Å	3.480
	2	1.175 eV	0.570 eV	0.242 Å	2.090
	3	1.545 eV	0.619 eV	0.473 Å	0.000
	4	0.572 eV	0.364 eV	0.960 Å	0.000
Mn	0	–	–	0.166 Å	4.080
	1	0.867 eV	0.450 eV	0.168 Å	3.240
	2	1.300 eV	0.607 eV	0.180 Å	0.980
	3	1.397 eV	0.534 eV	0.560 Å	0.000
	4	0.535 eV	-0.024 eV	1.861 Å	0.000
Fe	0	–	–	0.017 Å	2.950
	1	1.547 eV	0.391 eV	0.021 Å	1.870
	2	1.405 eV	0.717 eV	0.188 Å	0.000
	3	1.209 eV	0.416 eV	0.677 Å	0.000
	4	0.480 eV	0.026 eV	1.966 Å	0.000
Co	0	–	–	-0.037 Å	1.790
	1	1.767 eV	0.445 eV	-0.020 Å	0.000
	2	1.277 eV	0.668 eV	0.232 Å	0.000
	3	0.851 eV	0.339 eV	0.798 Å	0.000
	4	0.174 eV	0.072 eV	2.052 Å	0.000
Ni	0	–	–	-0.117 Å	0.000
	1	1.521 eV	0.382 eV	0.055 Å	0.000
	2	0.812 eV	0.570 eV	0.376 Å	0.000
	3	0.411 eV	0.419 eV	0.776 Å	0.000
	4	-0.036 eV	0.329 eV	1.221 Å	0.000

Table 4.3. Differential binding energy, vdW correction contribution, outward displacement, and magnetic moment (in unpaired electron units) for 3d transition metal substituent atoms (M) on the Cu(100) surface with up to 4 CO molecules adsorbed.

M	#CO	$E_{\text{b-n}^{\text{th}}\text{CO/M@Cu(111)}}$	E_{vdW}	z_M	magmom
Sc	0	–	–	0.395 Å	0.000
	1	0.806 eV	0.396 eV	0.409 Å	0.000
	2	0.808 eV	0.357 eV	0.438 Å	0.000
	3	0.828 eV	0.611 eV	0.498 Å	0.000
	4	0.541 eV	0.520 eV	0.729 Å	0.000
Ti	0	–	–	0.115 Å	0.890
	1	1.250 eV	0.441 eV	0.176 Å	0.000
	2	1.279 eV	0.487 eV	0.163 Å	0.000
	3	1.176 eV	0.617 eV	0.323 Å	0.000
	4	0.537 eV	0.476 eV	0.745 Å	0.000
V	0	–	–	0.110 Å	2.660
	1	1.310 eV	0.374 eV	0.124 Å	2.230
	2	1.469 eV	0.701 eV	0.122 Å	0.560
	3	1.434 eV	0.598 eV	0.381 Å	0.000
	4	0.431 eV	0.394 eV	0.901 Å	0.000
Cr	0	–	–	0.166 Å	3.830
	1	0.980 eV	0.429 eV	0.157 Å	3.170
	2	1.261 eV	0.686 eV	0.159 Å	1.340
	3	1.458 eV	0.592 eV	0.470 Å	0.000
	4	0.252 eV	0.301 eV	1.086 Å	0.000
Mn	0	–	–	0.153 Å	3.980
	1	0.889 eV	0.471 eV	0.104 Å	3.030
	2	1.264 eV	0.653 eV	0.189 Å	0.780
	3	1.347 eV	0.537 eV	0.576 Å	0.000
	4	0.021 eV	0.209 eV	1.296 Å	0.000
Fe	0	–	–	-0.033 Å	2.880
	1	1.481 eV	0.426 eV	-0.006 Å	1.790
	2	1.353 eV	0.672 eV	0.245 Å	0.000
	3	1.087 eV	0.483 eV	0.681 Å	0.000
	4	0.086 eV	-0.205 eV	2.145 Å	0.000
Co	0	–	–	-0.089 Å	1.630
	1	1.827 eV	0.447 eV	0.014 Å	0.000
	2	1.138 eV	0.655 eV	0.292 Å	0.000
	3	0.705 eV	0.478 eV	0.743 Å	0.000
	4	-0.177 eV	-0.210 eV	2.274 Å	0.000
Ni	0	–	–	-0.091 Å	0.000
	1	1.427 eV	0.451 eV	0.053 Å	0.000
	2	0.676 eV	0.655 eV	0.284 Å	0.000
	3	0.348 eV	0.537 eV	0.625 Å	0.000

Table 4.4. Differential binding energy, vdW correction contribution, outward displacement, and magnetic moment (in unpaired electron units) for 3d transition metal substituent atoms (M) on the Cu(111) surface with up to 4 CO molecules adsorbed.

M	#CO	$E_{\text{b-n}^{\text{th}}\text{CO/M@Cu(100)}}$	E_{vdW}	z_M	magmom
Y	0	–	–	0.645 Å	0.000
	1	0.804 eV	0.335 eV	0.701 Å	0.000
	2	0.766 eV	0.410 eV	0.777 Å	0.000
	3	0.808 eV	0.281 eV	0.743 Å	0.000
	4	0.900 eV	0.612 eV	0.771 Å	0.000
Zr	0	–	–	0.330 Å	0.000
	1	1.262 eV	0.349 eV	0.427 Å	0.000
	2	1.229 eV	0.360 eV	0.423 Å	0.000
	3	1.328 eV	0.468 eV	0.554 Å	0.000
	4	0.954 eV	0.625 eV	0.695 Å	0.000
Nb	0	–	–	0.211 Å	1.284
	1	1.625 eV	0.392 eV	0.261 Å	0.000
	2	1.745 eV	0.439 eV	0.293 Å	0.000
	3	1.661 eV	0.537 eV	0.500 Å	0.000
	4	0.763 eV	0.549 eV	0.776 Å	0.000
Mo	0	–	–	0.211 Å	2.749
	1	1.872 eV	0.370 eV	0.054 Å	0.000
	2	1.925 eV	0.547 eV	0.283 Å	0.000
	3	1.663 eV	0.548 eV	0.545 Å	0.000
	4	0.529 eV	0.465 eV	0.908 Å	0.000
Tc	0	–	–	0.123 Å	2.512
	1	2.227 eV	0.386 eV	0.054 Å	0.000
	2	1.885 eV	0.568 eV	0.319 Å	0.000
	3	1.423 eV	0.543 eV	0.623 Å	0.000
	4	0.234 eV	0.371 eV	1.134 Å	0.000
Ru	0	–	–	0.017 Å	0.994
	1	2.334 eV	0.382 eV	0.094 Å	0.000
	2	1.555 eV	0.584 eV	0.361 Å	0.000
	3	1.045 eV	0.514 eV	0.692 Å	0.000
	4	-0.167 eV	0.232 eV	1.249 Å	0.000
Rh	0	–	–	0.042 Å	0.000
	1	1.869 eV	0.351 eV	0.186 Å	0.000
	2	1.111 eV	0.592 eV	0.436 Å	0.000
	3	0.522 eV	0.498 eV	0.735 Å	0.000
Pd	0	–	–	0.141 Å	0.000
	1	0.940 eV	0.362 eV	0.294 Å	0.000
	2	0.682 eV	0.593 eV	0.411 Å	0.000
	3	0.331 eV	0.606 eV	0.438 Å	0.000

Table 4.5. Differential binding energy, vdW correction contribution, outward displacement, and magnetic moment (in unpaired electron units) for 4d transition metal substituent atoms (M) on the Cu(100) surface with up to 4 CO molecules adsorbed.

M	#CO	$E_{\text{b-n}^{\text{th}}\text{CO/M@Cu(111)}}$	E_{vdW}	z_M	magmom
Y	0	–	–	0.792 Å	0.000
	1	0.690 eV	0.293 eV	0.844 Å	0.000
	2	0.712 eV	0.254 eV	0.885 Å	0.000
	3	0.736 eV	0.393 eV	0.925 Å	0.000
	4	0.596 eV	0.500 eV	1.103 Å	0.000
Zr	0	–	–	0.338 Å	0.000
	1	1.192 eV	0.384 eV	0.400 Å	0.000
	2	1.140 eV	0.397 eV	0.411 Å	0.000
	3	1.172 eV	0.559 eV	0.483 Å	0.000
	4	0.708 eV	0.509 eV	0.835 Å	0.000
Nb	0	–	–	0.098 Å	0.360
	1	1.609 eV	0.335 eV	0.078 Å	0.000
	2	1.612 eV	0.599 eV	0.298 Å	0.000
	3	1.529 eV	0.595 eV	0.453 Å	0.000
	4	0.569 eV	0.432 eV	0.915 Å	0.000
Mo	0	–	–	0.110 Å	2.200
	1	1.945 eV	0.378 eV	0.020 Å	0.000
	2	1.769 eV	0.636 eV	0.239 Å	0.000
	3	1.546 eV	0.574 eV	0.519 Å	0.000
	4	0.328 eV	0.314 eV	1.092 Å	0.000
Tc	0	–	–	0.034 Å	1.960
	1	2.190 eV	0.393 eV	0.041 Å	0.000
	2	1.749 eV	0.636 eV	0.301 Å	0.000
	3	1.276 eV	0.547 eV	0.620 Å	0.000
	4	0.051 eV	0.197 eV	1.315 Å	0.000
Ru	0	–	–	-0.029 Å	0.100
	1	2.239 eV	0.418 eV	0.100 Å	0.000
	2	1.381 eV	0.642 eV	0.361 Å	0.000
	3	0.876 eV	0.500 eV	0.727 Å	0.000
	4	-0.242 eV	0.187 eV	1.434 Å	0.000
Rh	0	–	–	-0.001 Å	0.000
	1	1.797 eV	0.414 eV	0.176 Å	0.000
	2	0.825 eV	0.644 eV	0.403 Å	0.000
	3	0.448 eV	0.541 eV	0.711 Å	0.000
Pd	0	–	–	0.089 Å	0.000
	1	0.877 eV	0.392 eV	0.276 Å	0.000
	2	0.471 eV	0.699 eV	0.318 Å	0.000
	3	0.339 eV	0.587 eV	0.450 Å	0.000

Table 4.6. Differential binding energy, vdW correction contribution, outward displacement, and magnetic moment (in unpaired electron units) for 4d transition metal substituent atoms (M) on the Cu(111) surface with up to 4 CO molecules adsorbed.

4.3 Publication III

"Adsorption of CO on Copper Surface Islands With and Without Substitutional Atoms of More Reactive Transition Metals"

Submitted for review

Publication III connects the capability of multiple CO adsorption established in Publications I and II with the formation of steps and the preferred location of the transition-metal-carbonyl complexes. Motivated by experimental evidence linking copper restructuring and step density to CO_2 reduction activity [14], the study examines CO adsorption and diffusion on copper islands, the energetic cost of step formation, and the energetic preference of bare impurities and their carbonyl complexes for step or terrace configurations.

Calculations were carried out using the same level of theory as in Publication II, i.e. spin-polarized DFT calculations using the BEEF-vdW functional [33], the PAW method [38], and plane-wave method in VASP [137, 138]. Steps were modeled using striped island structures on Cu(100) and Cu(111). The paper presents CO adsorption energies and minimum-energy paths for migration across an island and along its step, calculated using the NEB method. Step formation energies were calculated with and without CO to quantify the stabilization associated with preferential adsorption at the steps. We also compared the energies of the 3d (Sc–Ni) and 4d (Y–Pd) substitutional atoms, when located at terrace, subsurface, and step sites. Differential binding energies were calculated for multiple CO adsorption at substitutional atoms located at steps. To determine whether the carbonyl complexes favor steps or terraces, the lowest-energy configurations at steps were compared with the corresponding terrace configurations.

The results show stronger CO binding at steps and lower barriers for diffusion along the step than for escape to the terrace. These findings support local CO accumulation at the undercoordinated step sites even when the overall coverage is low. CO adsorption also lowers the calculated step formation energy, while transition-metal-carbonyl complexes generally favor step sites over terraces. These energetic preferences suggest a possible indirect role of dilute alloying in catalysis through the formation of stable undercoordinated copper steps. Relocation of carbonyl complexes toward steps and pinning of fluctuating steps are possible mechanisms, but their pathways and rates remain to be established. The study therefore connects multiple adsorption with copper restructuring without establishing the consequences for catalytic activity or product selectivity.

Further information about the calculations, together with preliminary results not presented in Publication III, is given below. These results examine the dependence of CO adsorption on the surface model and adsorption site, the relationship between binding and magnetic properties, and the effect of applied potential on the preference for step and terrace configurations.

Figure 4.3 compares the Cu(100) island model with the conventional stepped Cu(711) sawtooth model, showing the structures, adsorption sites, and corresponding CO adsorption energies near the step. CO binds consistently more strongly at the investigated sites on the Cu(100) island than at the corresponding sites on Cu(711). Compressive strain can weaken CO adsorption [121], and the differences may partly reflect the different constraints on relaxation in the two models. The Cu(100) island has more freedom to relax laterally, whereas the periodically repeated steps in the Cu(711) model may produce a different strain distribution. This comparison illustrates that the choice of stepped surface model can affect the calculated adsorption energies.

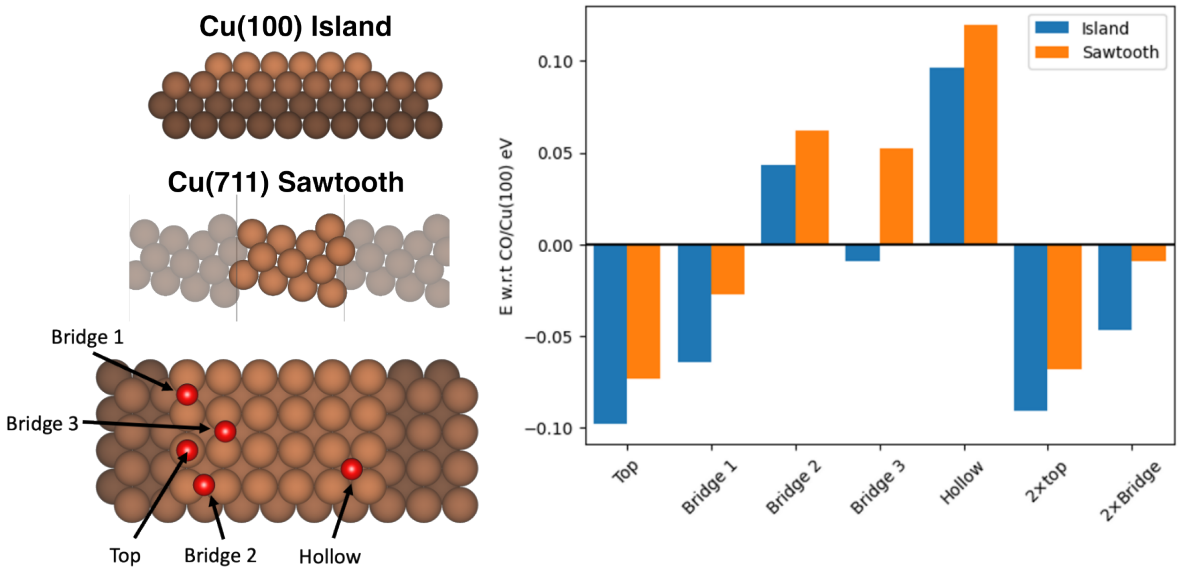

Figure 4.3. Left: The Cu(100) island and Cu(711) sawtooth structures, and the adsorption sites near the step that were compared. Right: differential adsorption energy of CO adsorbed at the step of a Cu(100) island, or at the equivalent locations on a Cu(711) sawtooth structure, with respect to the adsorption energy of CO on the Cu(100) surface.

In Figure 4.4, the chemical contribution to the differential binding energy is plotted against $(\varepsilon_{d\uparrow} - \varepsilon_{d\downarrow})\mu$ for V, Cr, and Mn substitutional atoms at Cu(100) and Cu(111) island steps. The results indicate an approximately linear relationship for configurations with one adsorbed CO molecule, and across the plotted configurations, CO binding generally becomes stronger as this quantity approaches zero. As the number of adsorbed CO molecules increases, deviations from this relationship become more pronounced. Interactions between the coadsorbed molecules may contribute to these deviations. The correlation is consistent with the adsorption trends discussed in Publications I and II, where stronger differential binding can accompany a reduction in magnetic moment. It suggests that the magnetic properties of the substitutional atom contribute to understanding why differential binding energies do not always decrease with consecutive CO adsorption.

Figure 4.5 presents preliminary results for the effect of applied potential on the relative energies of step and terrace configurations containing 3d substitutional atoms in Cu(100). The potential-dependent calculations were performed using VASPsol++ with parameters representing an aqueous electrolyte at pH 7 [78]. The number of favorably adsorbed CO molecules for each element remains unchanged over the investigated potential range compared with that found at the potential of zero charge. The plotted quantity is the grand-canonical potential difference between the step and terrace configurations. More negative values indicate a stronger preference for the step configuration. For all the elements shown, the energy difference becomes more negative as the potential changes from 0.0 to -1.0 V vs. RHE. The Sc and Ti configurations change from positive to negative values, indicating a change in preference from terrace to step sites, while the remaining configurations already favor steps at 0.0 V. These calculations suggest that cathodic potential can strengthen the energetic preference for carbonyl complexes at steps and, in some cases, reverse an initial preference for terraces.

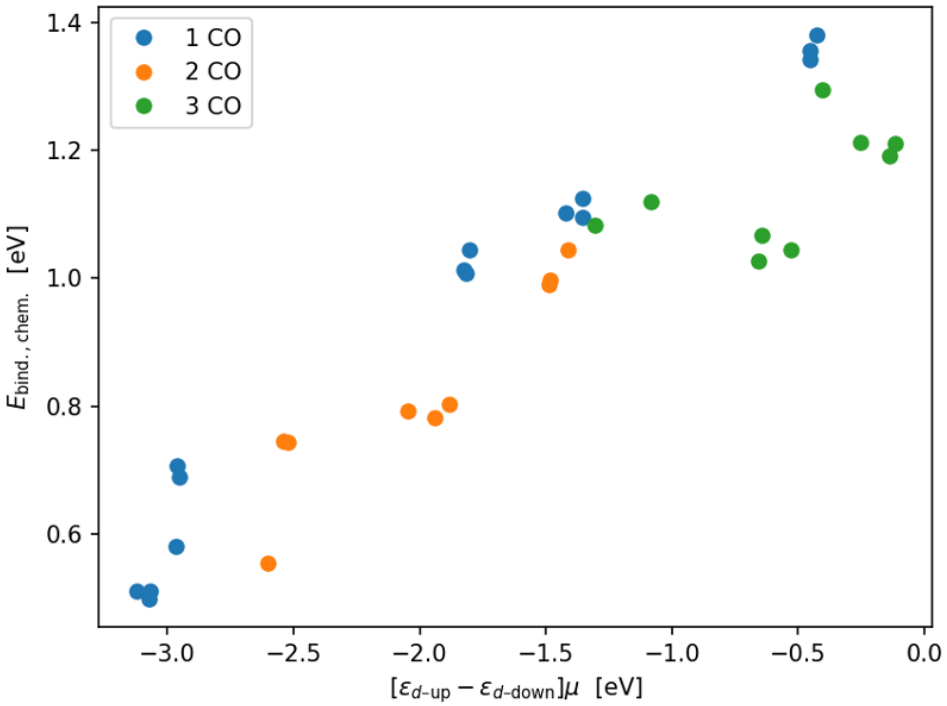

Figure 4.4. Chemical contribution to the CO binding energy, $E_{\text{bind,chem}}$, for V, Cr, and Mn substitutional atoms at Cu(100) and Cu(111) island steps, plotted against $(\varepsilon_{d\uparrow} - \varepsilon_{d\downarrow})\mu$. Here, $\varepsilon_{d\uparrow}$ and $\varepsilon_{d\downarrow}$ are the spin-resolved d-band centers, and μ is the magnetic moment of the substitutional atom divided by its number of d electrons. Blue, orange, and green points represent configurations containing one, two, and three adsorbed CO molecules, respectively.

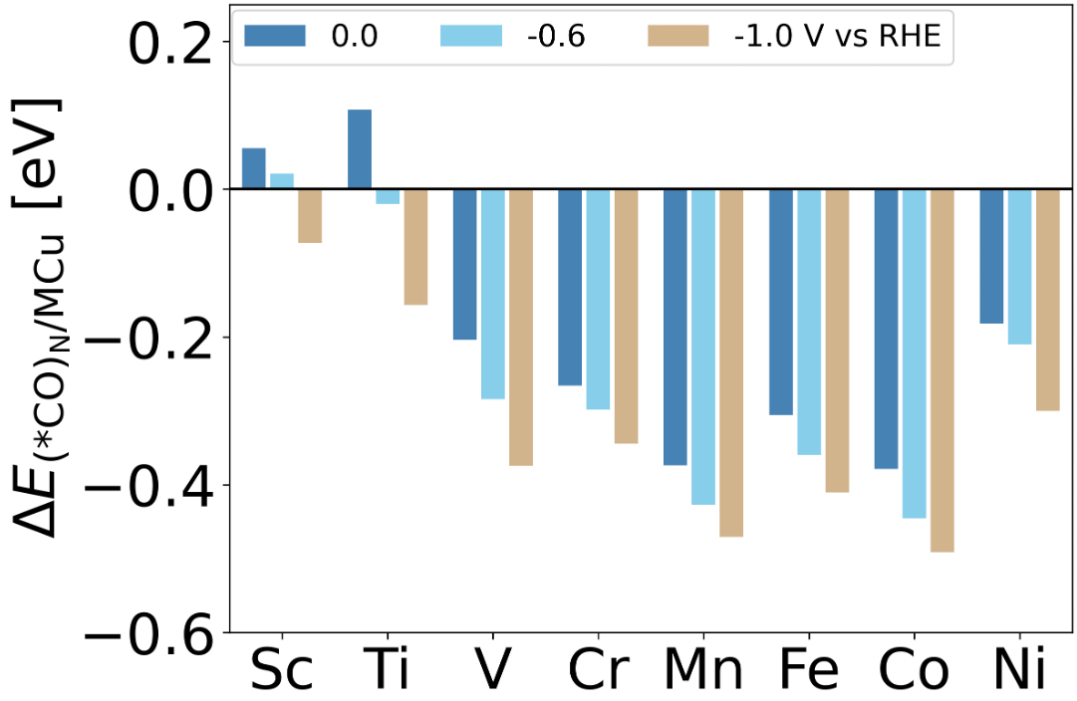

Figure 4.5. Potential dependence of the grand-canonical potential difference between step and terrace transition-metal carbonyl configurations containing substitutional 3d atoms in Cu(100). Negative values indicate a preference for the step configuration. Dark blue, light blue, and beige bars show results at 0.0, −0.6, and −1.0 V versus RHE, respectively. Calculations were performed using VASPsol++ for an aqueous electrolyte at pH 7.

5 Conclusion and Outlook

This thesis applies DFT to investigate how CO adsorption affects the structure and stability of copper surfaces containing substitutional transition-metal atoms. Adsorption of multiple CO molecules to substitutional transition-metal atoms is examined on Cu(100) and Cu(111) terraces and steps, together with the accompanying structural and electronic changes. Calculations using RPBE and BEEF-vdW characterize the adsorption energies, including the contribution from dispersion interactions in the latter. C–O stretching frequencies provide possible experimental signatures of multiple adsorption, while minimum-energy paths obtained using the NEB method describe CO migration on copper islands and along their steps. The goal has been to establish how substitutional transition-metal atoms bind multiple CO molecules and how the resulting carbonyl complexes affect surface stability, providing a basis for understanding their possible role in further CO reduction and surface restructuring.

From the calculations presented in Publications I and II, distinct CO adsorption patterns emerge across the transition metals studied. The later transition metals generally show strong initial CO adsorption that weakens with subsequent CO adsorption, while some atoms with substantial magnetic moments show increasing differential binding energies as the magnetic moment decreases. The earlier transition metals show more consistent differential binding energies and can adsorb up to four CO molecules more strongly than the corresponding copper surfaces. These results show that the binding energy of the first CO molecule alone does not necessarily provide a reliable descriptor for substitutional atoms [117, 118].

Publication III extends the work of Publications I and II to steps on Cu(100) and Cu(111) island surfaces. The adsorption calculations show that CO binds more strongly to the undercoordinated Cu step atoms than to terrace sites, reducing the calculated step formation energy by roughly 50%. The calculated minimum-energy paths also show a larger barrier for CO diffusion from the step back to the terrace than for diffusion along the step. CO molecules are therefore likely to collect at steps and diffuse mainly along them, increasing the probability of two molecules occupying adjacent sites where C–C bond formation may occur. While the bare substitutional atoms generally show small energetic preferences between stepped and terrace structures, their carbonyl complexes in most cases have a stronger preference for steps. This suggests that CO adsorption can provide a driving force for bringing the complexes to steps. Alternatively, fluctuating copper steps might encounter the carbonyl complexes and become locally stabilized, inhibiting the reformation of the terrace structure. Both processes could contribute to increased or more persistent step densities, although their mechanisms and rates are not established. Additional preliminary calculations for selected Cu(100) configurations further indicate that cathodic potential strengthens the preference for transition-metal carbonyl complexes at steps and can reverse an initial preference for terraces.

Together, these studies establish multiple CO adsorption as an important characteristic of substitutional transition-metal sites that is not captured by the first CO binding energy alone. Their broader contribution is to connect this capacity for carbonyl formation with the structure and

restructuring of the copper host. This provides an energetic basis for a possible indirect role of dilute alloying in catalysis: substitutional atoms may help stabilize the copper step structures where CO molecules can accumulate at neighboring sites, providing opportunities for C–C bond formation. The work therefore identifies surface stabilization as an additional factor to consider when interpreting the catalytic effects of more reactive substitutional atoms.

For computational screening in general, these findings support evaluating multiple adsorption of reactants at isolated and atomically distinct sites, such as those found in single-atom alloys and single-atom catalysts. Experimentally, comparing impurity locations and surface morphology before and during reactant exposure would help test whether carbonyl formation contributes to surface restructuring.

A main limitation of the present work is that most calculations were performed without solvent, electrolyte, or an applied electrode potential. The preliminary potential-dependent calculations examine selected Cu(100) configurations, but do not establish how the electrochemical conditions affect the adsorption patterns across all elements, CO occupations, and surface structures. A broader treatment is therefore needed to assess the relative energies of carbonyl complexes at steps and terraces under reaction conditions. Furthermore, soluble copper-carbonyls have been suggested by computational work as intermediates in dissolution and redeposition [108], motivating consideration of whether solvation could favor detachment of the transition-metal carbonyls studied here.

Hydrogen and hydroxyl coverages were also omitted because including these adsorbates alongside CO greatly increases the number of possible configurations at the substitutional atom and surrounding copper surface. Their combined presence on copper-based SAAs could promote copper restructuring [129, 109, 139], influence competition for adsorption sites, transition-metal carbonyl formation, and the stability of undercoordinated surface sites.

Finally, the calculations do not establish the exact mechanisms for the migration of transition-metal-carbonyl complexes, step formation, or step pinning. Although CO accumulation at steps provides opportunities for neighboring molecules to react, evaluating its exact effects on activity and selectivity requires calculating the barriers for C–C bond formation and for competing reactions.

Future work should extend the preliminary potential-dependent calculations to additional elements and CO occupations and examine the effects of solvation, electrolyte, and selected hydrogen and hydroxyl coverages. Kinetic Monte Carlo simulations using the calculated CO diffusion barriers, supplemented by calculations of lateral CO interactions, would be a natural next step to examine local CO accumulation at steps and terraces and the frequency of encounters between adsorbed molecules. These simulations could subsequently include reaction pathways to assess the consequences for C–C bond formation.

This thesis establishes the capacity of substitutional transition-metal atoms in copper to bind multiple CO molecules and shows that the resulting carbonyl complexes generally favor undercoordinated sites such as steps. The preference for steps provides an energetic basis for a possible indirect role of dilute alloying in catalysis through stabilization of the copper surface structures where CO accumulates. Understanding copper-based SAAs therefore requires considering the adsorption capacity of the substitutional atoms together with the response of the copper host. These findings provide a foundation for investigating how alloy composition and adsorbate-induced restructuring influence catalysis, including CO_2 reduction.

References

[1] Katherine Calvin, Dipak Dasgupta, Gerhard Krinner, Aditi Mukherji, Peter W. Thorne, Christopher Trisos, José Romero, Paulina Aldunce, Ko Barrett, Gabriel Blanco, William W.L. Cheung, Sarah Connors, Fatima Denton, Aïda Diongue-Niang, David Dodman, Matthias Garschagen, Oliver Geden, Bronwyn Hayward, Christopher Jones, Frank Jotzo, Thelma Krug, Rodel Lasco, Yune-Yi Lee, Valérie Masson-Delmotte, Malte Meinshausen, Katja Mintenbeck, Abdalah Mokssit, Friederike E.L. Otto, Minal Pathak, Anna Pirani, Elvira Poloczanska, Hans-Otto Pörtner, Aromar Revi, Debra C. Roberts, Joyashree Roy, Alex C. Ruane, Jim Skea, Priyadarshi R. Shukla, Raphael Slade, Aimée Slangen, Youba Sokona, Anna A. Sörensson, Melinda Tignor, Detlef Van Vuuren, Yi-Ming Wei, Harald Winkler, Panmao Zhai, Zinta Zommers, Jean-Charles Hourcade, Francis X. Johnson, Shonali Pachauri, Nicholas P. Simpson, Chandni Singh, Adelle Thomas, Edmond Totin, Andrés Alegría, Kyle Armour, Birgit Bednar-Friedl, Kornelis Blok, Guéladio Cissé, Frank Dentener, Siri Eriksen, Erich Fischer, Gregory Garner, Céline Guivarch, Marjolijn Haasnoot, Gerrit Hansen, Mathias Hauser, Ed Hawkins, Tim Hermans, Robert Kopp, Noëmie Leprince-Ringuet, Jared Lewis, Debora Ley, Chloé Ludden, Leila Niamir, Zebedee Nicholls, Shreya Some, Sophie Szopa, Blair Trewin, Kaj-Ivar Van Der Wijst, Gundula Winter, Maximilian Witting, Arlene Birt, and Meeyoung Ha. *IPCC, 2023: Climate Change 2023: Synthesis Report. Contribution of Working Groups I, II and III to the Sixth Assessment Report of the Intergovernmental Panel on Climate Change [Core Writing Team, H. Lee and J. Romero (eds.)]. IPCC, Geneva, Switzerland.* en. Tech. rep. Edition: First. Intergovernmental Panel on Climate Change (IPCC), July 2023. DOI: 10.59327/IPCC/AR6-9789291691647. (Visited on 09/25/2026).

[2] Phil De Luna, Christopher Hahn, Drew Higgins, Shaffiq A. Jaffer, Thomas F. Jaramillo, and Edward H. Sargent. "What would it take for renewably powered electrosynthesis to displace petrochemical processes?" *Science* 364.6438 (Apr. 2019), eaav3506. DOI: 10.1126/science.aav3506. (Visited on 09/24/2026).

[3] Omar J. Guerra, Hussain M. Almajed, Wilson A. Smith, Ana Somoza-Tornos, and Bri-Mathias S. Hodge. "Barriers and opportunities for the deployment of CO2 electrolysis in net-zero emissions energy systems." *Joule* 7.6 (June 2023), pp. 1111–1133. DOI: 10.1016/j.joule.2023.05.002. (Visited on 09/20/2026).

[4] Cameron Hepburn, Ella Adlen, John Beddington, Emily A. Carter, Sabine Fuss, Niall Mac Dowell, Jan C. Minx, Pete Smith, and Charlotte K. Williams. "The technological and economic prospects for CO2 utilization and removal." en. *Nature* 575.7781 (Nov. 2019), pp. 87–97. DOI: 10.1038/s41586-019-1681-6. (Visited on 09/24/2026).

[5] Jens Artz, Thomas E. Müller, Katharina Thenert, Johanna Kleinekorte, Raoul Meys, André Sternberg, André Bardow, and Walter Leitner. "Sustainable Conversion of Carbon Dioxide: An Integrated Review of Catalysis and Life Cycle Assessment." *Chemical Reviews* 118.2 (Jan. 2018), pp. 434–504. DOI: 10.1021/acs.chemrev.7b00435. (Visited on 09/24/2026).

[6] Wanyu Deng, Ahryeon Lee, Wentao Dai, Luke Cherniack, Bradie S. Crandall, Hefei Li, and Feng Jiao. “Techno-economics of polymer-membrane-based CO2 electrolysers.” en. *Nature Reviews Clean Technology* 1.4 (Apr. 2025), pp. 255–268. DOI: 10.1038/s44359-025-00045-1. (Visited on 09/24/2026).

[7] Yoshio Hori, Akira Murata, and Ryutaro Takahashi. “Formation of hydrocarbons in the electrochemical reduction of carbon dioxide at a copper electrode in aqueous solution.” *Journal of the Chemical Society, Faraday Transactions 1: Physical Chemistry in Condensed Phases* 85.8 (Jan. 1989), pp. 2309–2326. DOI: 10.1039/F19898502309. (Visited on 09/19/2026).

[8] Y. Hori, I. Takahashi, O. Koga, and N. Hoshi. “Electrochemical reduction of carbon dioxide at various series of copper single crystal electrodes.” *Journal of Molecular Catalysis A: Chemical*. Special Issue dedicated to Professor Juro Horiuti in commemoration of his centennial birthday and his contribution to science. 199.1 (May 2003), pp. 39–47. DOI: 10.1016/S1381-1169(03)00016-5. (Visited on 09/20/2026).

[9] Stephanie Nitopi, Erlend Bertheussen, Soren B. Scott, Xinyan Liu, Albert K. Engstfeld, Sebastian Horch, Brian Seger, Ifan E. L. Stephens, Karen Chan, Christopher Hahn, Jens K. Nørskov, Thomas F. Jaramillo, and Ib Chorkendorff. “Progress and Perspectives of Electrochemical CO2 Reduction on Copper in Aqueous Electrolyte.” en. *Chemical Reviews* 119.12 (June 2019), pp. 7610–7672. DOI: 10.1021/acs.chemrev.8b00705. (Visited on 09/19/2026).

[10] Sanaz Soodi, Jun-Jun Zhang, Jie Zhang, Yuefeng Liu, Mohsen Lashgari, Spyridon Zafeiratos, Andreas Züttel, Kun Zhao, and Wen Luo. “Selective electroreduction of CO2 to C2+ products on cobalt decorated copper catalysts.” en. *Chemical Synthesis* 4.3 (Aug. 2024), N/A–N/A. DOI: 10.20517/cs.2024.11. (Visited on 10/08/2026).

[11] Georgios Giannakakis, Maria Flytzani-Stephanopoulos, and E. Charles H. Sykes. “Single-Atom Alloys as a Reductionist Approach to the Rational Design of Heterogeneous Catalysts.” en. *Accounts of Chemical Research* 52.1 (Jan. 2019), pp. 237–247. DOI: 10.1021/acs.accounts.8b00490. (Visited on 09/23/2026).

[12] Yicheng Wang, Julia Schumann, Elizabeth E. Happel, Volkan Çınar, E. Charles H. Sykes, Michail Stamatakis, Angelos Michaelides, and Ryan T. Hannagan. “Observation and Characterization of Dicarbonyls on a RhCu Single-Atom Alloy.” eng (July 2022). DOI: 10.17863/CAM.87822. (Visited on 09/23/2026).

[13] Baran Eren, Daniel Torres, Osman Karslıoğlu, Zongyuan Liu, Cheng Hao Wu, Dario Stacchiola, Hendrik Bluhm, Gabor A. Somorjai, and Miquel Salmeron. “Structure of Copper–Cobalt Surface Alloys in Equilibrium with Carbon Monoxide Gas.” *J. Am. Chem. Soc.* 140.21 (2018), pp. 6575–6581. DOI: 10.1021/jacs.7b13621.

[14] Dongfang Cheng, Khanh-Ly C. Nguyen, Vaidish Sumaria, Ziyang Wei, Zisheng Zhang, Winston Gee, Yichen Li, Carlos G. Morales-Guio, Markus Heyde, Beatriz Roldan Cuenya, Anastassia N. Alexandrova, and Philippe Sautet. “Structure Sensitivity and Catalyst Restructuring for CO2 Electro-reduction on Copper.” en. *Nature Communications* 16.1 (Apr. 2025), p. 4064. DOI: 10.1038/s41467-025-59267-3. (Visited on 09/09/2026).

[15] Reihaneh Amirbeigiarab, Jing Tian, Antonia Herzog, Canrong Qiu, Arno Bergmann, Beatriz Roldan Cuenya, and Olaf M. Magnussen. “Atomic-scale surface restructuring of copper electrodes under CO2 electroreduction conditions.” en. *Nature Catalysis* 6.9 (Sept. 2023), pp. 837–846. DOI: 10.1038/s41929-023-01009-z. (Visited on 09/22/2026).

[16] Youn-Geun Kim, Jack Hess Baricuatro, Alnald Javier, John Mathew Gregoire, and Manuel P. Soriaga. "The Evolution of the Polycrystalline Copper Surface, First to Cu(111) and Then to Cu(100), at a Fixed CO2RR Potential: A Study by Operando EC-STM." *Langmuir* 30.50 (Dec. 2014), pp. 15053–15056. DOI: 10.1021/la504445g. (Visited on 09/22/2026).

[17] Wolfram Koch and Max C. Holthausen. *A Chemist's Guide to Density Functional Theory*. en. 1st ed. Wiley, July 2001. ISBN: 978-3-527-30372-4 978-3-527-60004-5. DOI: 10.1002/3527600043. (Visited on 10/09/2026).

[18] E. Schrödinger. "Quantisierung als Eigenwertproblem." en. *Annalen der Physik* 384.4 (Jan. 1926), pp. 361–376. DOI: 10.1002/andp.19263840404. (Visited on 09/25/2026).

[19] M. Born and R. Oppenheimer. "Zur Quantentheorie der Molekeln." en. *Annalen der Physik* 389.20 (1927), pp. 457–484. DOI: 10.1002/andp.19273892002. (Visited on 09/25/2026).

[20] Trygve Helgaker, Poul Jørgensen, and Jeppe Olsen. "Molecular Integral Evaluation." en. *Molecular Electronic-Structure Theory*. Section: 9. John Wiley & Sons, Ltd, 2000, pp. 336–432. ISBN: 978-1-119-01957-2. DOI: 10.1002/9781119019572.ch9. (Visited on 09/25/2026).

[21] D. R. Hartree. "The Wave Mechanics of an Atom with a Non-Coulomb Central Field. Part I. Theory and Methods." en. *Mathematical Proceedings of the Cambridge Philosophical Society* 24.1 (Jan. 1928), pp. 89–110. DOI: 10.1017/S0305004100011919. (Visited on 09/25/2026).

[22] J. C. Slater. "The Theory of Complex Spectra." *Physical Review* 34.10 (Nov. 1929), pp. 1293–1322. DOI: 10.1103/PhysRev.34.1293. (Visited on 09/25/2026).

[23] V. Fock. "Näherungsmethode zur Lösung des quantenmechanischen Mehrkörperproblems." de. *Zeitschrift für Physik* 61.1 (Jan. 1930), pp. 126–148. DOI: 10.1007/BF01340294. (Visited on 09/25/2026).

[24] P. Hohenberg and W. Kohn. "Inhomogeneous Electron Gas." *Physical Review* 136.3B (Nov. 1964), B864–B871. DOI: 10.1103/PhysRev.136.B864. (Visited on 09/25/2026).

[25] W. Kohn and L. J. Sham. "Self-Consistent Equations Including Exchange and Correlation Effects." *Physical Review* 140.4A (Nov. 1965), A1133–A1138. DOI: 10.1103/PhysRev.140.A1133. (Visited on 09/25/2026).

[26] U. von Barth and L. Hedin. "A local exchange-correlation potential for the spin polarized case. i." en. *Journal of Physics C: Solid State Physics* 5.13 (July 1972), p. 1629. DOI: 10.1088/0022-3719/5/13/012. (Visited on 09/25/2026).

[27] John P. Perdew, Kieron Burke, and Matthias Ernzerhof. "Generalized Gradient Approximation Made Simple." *Physical Review Letters* 77.18 (Oct. 1996), pp. 3865–3868. DOI: 10.1103/PhysRevLett.77.3865. (Visited on 09/25/2026).

[28] B. Hammer, L. B. Hansen, and J. K. Nørskov. "Improved adsorption energetics within density-functional theory using revised Perdew-Burke-Ernzerhof functionals." *Physical Review B* 59.11 (Mar. 1999), pp. 7413–7421. DOI: 10.1103/PhysRevB.59.7413. (Visited on 09/25/2026).

[29] M. Dion, H. Rydberg, E. Schröder, D. C. Langreth, and B. I. Lundqvist. "Van der Waals Density Functional for General Geometries." en. *Physical Review Letters* 92.24 (June 2004), p. 246401. DOI: 10.1103/PhysRevLett.92.246401. (Visited on 09/10/2026).

[30] F. London. “Zur Theorie und Systematik der Molekularkräfte.” de. *Zeitschrift für Physik* 63.3 (Mar. 1930), pp. 245–279. DOI: 10.1007/BF01421741. (Visited on 09/10/2026).

[31] T. Thonhauser, Valentino R. Cooper, Shen Li, Aaron Puzder, Per Hyldgaard, and David C. Langreth. “Van der Waals density functional: Self-consistent potential and the nature of the van der Waals bond.” en. *Physical Review B* 76.12 (Sept. 2007), p. 125112. DOI: 10.1103/PhysRevB.76.125112. (Visited on 09/10/2026).

[32] Kyuho Lee, Éamonn D. Murray, Lingzhu Kong, Bengt I. Lundqvist, and David C. Langreth. “Higher-accuracy van der Waals density functional.” *Physical Review B* 82.8 (Aug. 2010), p. 081101. DOI: 10.1103/PhysRevB.82.081101. (Visited on 09/10/2026).

[33] Jess Wellendorff, Keld T. Lundgaard, Andreas Møgelhøj, Vivien Petzold, David D. Landis, Jens K. Nørskov, Thomas Bligaard, and Karsten W. Jacobsen. “Density functionals for surface science: Exchange-correlation model development with Bayesian error estimation.” en. *Physical Review B* 85.23 (June 2012), p. 235149. DOI: 10.1103/PhysRevB.85.235149. (Visited on 09/10/2026).

[34] Felix Bloch. “Über die Quantenmechanik der Elektronen in Kristallgittern.” de. *Zeitschrift für Physik* 52.7 (July 1929), pp. 555–600. DOI: 10.1007/BF01339455. (Visited on 09/11/2026).

[35] Hendrik J. Monkhorst and James D. Pack. “Special points for Brillouin-zone integrations.” en. *Physical Review B* 13.12 (June 1976), pp. 5188–5192. DOI: 10.1103/PhysRevB.13.5188. (Visited on 09/11/2026).

[36] M. C. Payne, M. P. Teter, D. C. Allan, T. A. Arias, and J. D. Joannopoulos. “Iterative minimization techniques for *ab initio* total-energy calculations: molecular dynamics and conjugate gradients.” en. *Reviews of Modern Physics* 64.4 (Oct. 1992), pp. 1045–1097. DOI: 10.1103/RevModPhys.64.1045. (Visited on 09/11/2026).

[37] G. Kresse and J. Furthmüller. “Efficient iterative schemes for *ab initio* total-energy calculations using a plane-wave basis set.” en. *Physical Review B* 54.16 (Oct. 1996), pp. 11169–11186. DOI: 10.1103/PhysRevB.54.11169. (Visited on 09/11/2026).

[38] P. E. Blöchl. “Projector augmented-wave method.” en. *Physical Review B* 50.24 (Dec. 1994), pp. 17953–17979. DOI: 10.1103/PhysRevB.50.17953. (Visited on 09/11/2026).

[39] G. Kresse and D. Joubert. “From ultrasoft pseudopotentials to the projector augmented-wave method.” en. *Physical Review B* 59.3 (Jan. 1999), pp. 1758–1775. DOI: 10.1103/PhysRevB.59.1758. (Visited on 09/11/2026).

[40] Carsten Rostgaard. *The Projector Augmented-wave Method*. arXiv:0910.1921 [cond-mat.mtrl-sci]. Oct. 2009. DOI: 10.48550/arXiv.0910.1921. (Visited on 09/11/2026).

[41] N. David Mermin. “Thermal Properties of the Inhomogeneous Electron Gas.” en. *Physical Review* 137.5A (Mar. 1965), A1441–A1443. DOI: 10.1103/PhysRev.137.A1441. (Visited on 09/14/2026).

[42] M. Methfessel and A. T. Paxton. “High-precision sampling for Brillouin-zone integration in metals.” en. *Physical Review B* 40.6 (Aug. 1989), pp. 3616–3621. DOI: 10.1103/PhysRevB.40.3616. (Visited on 09/11/2026).

[43] Nicola Marzari, David Vanderbilt, and M. C. Payne. “Ensemble Density-Functional Theory for *Ab Initio* Molecular Dynamics of Metals and Finite-Temperature Insulators.” en. *Physical Review Letters* 79.7 (Aug. 1997), pp. 1337–1340. DOI: 10.1103/PhysRevLett.79.1337. (Visited on 09/14/2026).

[44] Jens K. Nørskov, Frank Abild-Pedersen, Felix Studt, and Thomas Bligaard. "Density functional theory in surface chemistry and catalysis." *Proceedings of the National Academy of Sciences* 108.3 (Jan. 2011), pp. 937–943. DOI: 10.1073/pnas.1006652108. (Visited on 09/19/2026).

[45] Juarez L. F. Da Silva, Catherine Stampfl, and Matthias Scheffler. "Converged properties of clean metal surfaces by all-electron first-principles calculations." *Surface Science* 600.3 (Feb. 2006), pp. 703–715. DOI: 10.1016/j.susc.2005.12.008. (Visited on 09/19/2026).

[46] Lennart Bengtsson. "Dipole correction for surface supercell calculations." *Physical Review B* 59.19 (May 1999), pp. 12301–12304. DOI: 10.1103/PhysRevB.59.12301. (Visited on 09/19/2026).

[47] Mihai-Cosmin Marinica, Cyrille Barreteau, Daniel Spanjaard, and Marie-Catherine Desjonquères. "Diffusion rates of Cu adatoms on Cu(111) in the presence of an adisland nucleated at fcc or hcp sites." *Physical Review B* 72.11 (Sept. 2005), p. 115402. DOI: 10.1103/PhysRevB.72.115402. (Visited on 09/19/2026).

[48] Marek Gajdoš, Andreas Eichler, and Jürgen Hafner. "CO adsorption on close-packed transition and noble metal surfaces: trends from ab initio calculations." en. *Journal of Physics: Condensed Matter* 16.8 (Feb. 2004), p. 1141. DOI: 10.1088/0953-8984/16/8/001. (Visited on 09/19/2026).

[49] H. Bernhard Schlegel. "Geometry optimization." *WIREs Computational Molecular Science* (2011). DOI: 10.1002/wcms.34. (Visited on 09/16/2026).

[50] J. K. Nørskov, J. Rossmeisl, A. Logadottir, L. Lindqvist, J. R. Kitchin, T. Bligaard, and H. Jónsson. "Origin of the Overpotential for Oxygen Reduction at a Fuel-Cell Cathode." *The Journal of Physical Chemistry B* 108.46 (Nov. 2004), pp. 17886–17892. DOI: 10.1021/jp047349j. (Visited on 09/19/2026).

[51] Hannes J?nsson, Greg Mills, and Karsten W. Jacobsen. "Nudged elastic band method for finding minimum energy paths of transitions." *Classical and Quantum Dynamics in Condensed Phase Simulations*. WORLD SCIENTIFIC, June 1998, pp. 385–404. ISBN: 978-981-02-3498-0. DOI: 10.1142/9789812839664_0016. (Visited on 09/16/2026).

[52] George H. Vineyard. "Frequency factors and isotope effects in solid state rate processes." *Journal of Physics and Chemistry of Solids* (1957). DOI: 10.1016/0022-3697(57)90059-8. (Visited on 09/16/2026).

[53] *RheoMan - Nudged Elastic Band*. https://umet.univ-lille.fr/Projets/RheoMan/en/to-learn-more-about/nudged-elastic-band.php.html.

[54] Yorick L. A. Schmerwitz, Vilhjálmur Ásgeirsson, and Hannes Jónsson. *Improved Initialization of Optimal Path Calculations Using Sequential Traversal over the Image Dependent Pair Potential Surface*. arXiv:2310.04531 [physics.chem-ph] version: 1. Oct. 2023. DOI: 10.48550/arXiv.2310.04531. (Visited on 09/25/2026).

[55] Graeme Henkelman and Hannes Jónsson. "Improved tangent estimate in the nudged elastic band method for finding minimum energy paths and saddle points." *The Journal of Chemical Physics* (2000). DOI: 10.1063/1.1323224. (Visited on 09/16/2026).

[56] Graeme Henkelman, Blas P. Uberuaga, and Hannes Jónsson. "A climbing image nudged elastic band method for finding saddle points and minimum energy paths." *The Journal of Chemical Physics* (2000). DOI: 10.1063/1.1329672. (Visited on 09/16/2026).

[57] Donald G Truhlar, Bruce C Garrett, and Stephen J Klippenstein. "Current Status of Transition-State Theory." en ().

[58] Henry Eyring. “The Activated Complex in Chemical Reactions.” *The Journal of Chemical Physics* (1935). DOI: 10.1063/1.1749604. (Visited on 09/16/2026).

[59] Michele Re Fiorentin, Michele G. Bianchi, Magnus A. H. Christiansen, Anna Ciotti, Francesca Risplendi, Wei Wang, Elvar Ö. Jónsson, Hannes Jónsson, and Giancarlo Cicero. “Methodological Frameworks for Computational Electrocatalysis: From Theory to Practice.” en. *Small Methods* 10.5 (2026), e01542. DOI: 10.1002/smtd.202501542. (Visited on 09/07/2026).

[60] Nuria Garcia-Araez, Victor Climent, and Juan Feliu. “Potential-Dependent Water Orientation on Pt(111), Pt(100), and Pt(110), As Inferred from Laser-Pulsed Experiments. Electrostatic and Chemical Effects.” en. *The Journal of Physical Chemistry C* 113.21 (May 2009), pp. 9290–9304. DOI: 10.1021/jp900792q. (Visited on 09/17/2026).

[61] H. Helmholtz. “Studien über electrische Grenzschichten.” en. *Annalen der Physik* 243.7 (1879), pp. 337–382. DOI: 10.1002/andp.18792430702. (Visited on 09/17/2026).

[62] M. Gouy. “Sur la constitution de la charge électrique à la surface d’un électrolyte.” fr. *Journal de Physique Théorique et Appliquée* 9.1 (1910), pp. 457–468. DOI: 10.1051/jphystap:019100090045700. (Visited on 09/17/2026).

[63] David Leonard Chapman. “LI. A contribution to the theory of electrocapillarity.” *The London, Edinburgh, and Dublin Philosophical Magazine and Journal of Science* 25.148 (Apr. 1913), pp. 475–481. DOI: 10.1080/14786440408634187. (Visited on 09/17/2026).

[64] Otto Stern. “Zur Theorie Der Elektrolytischen Doppelschicht.” en. *Zeitschrift für Elektrochemie und angewandte physikalische Chemie* 30.21-22 (1924), pp. 508–516. DOI: 10.1002/bbpc.192400182. (Visited on 09/17/2026).

[65] David C. Grahame. “The Electrical Double Layer and the Theory of Electrocapillarity.” *Chemical Reviews* 41.3 (Dec. 1947), pp. 441–501. DOI: 10.1021/cr60130a002. (Visited on 09/17/2026).

[66] Wolfgang Schmickler and Elizabeth Santos. *Interfacial Electrochemistry*. en. Google-Books-ID: JkIJpYaWp2sC. Springer Science & Business Media, Aug. 2010. ISBN: 978-3-642-04937-8.

[67] Kasinath Ojha, Katharina Doblhoff-Dier, and Marc T. M. Koper. “Double-layer structure of the Pt(111)–aqueous electrolyte interface.” *Proceedings of the National Academy of Sciences* 119.3 (Jan. 2022), e2116016119. DOI: 10.1073/pnas.2116016119. (Visited on 09/17/2026).

[68] S. Trasatti. “The absolute electrode potential: an explanatory note (Recommendations 1986).” en. *Pure and Applied Chemistry* 58.7 (Jan. 1986), pp. 955–966. DOI: 10.1351/pac198658070955. (Visited on 09/17/2026).

[69] Sergio Trasatti. “The concept of absolute electrode potential an attempt at a calculation.” *Journal of Electroanalytical Chemistry and Interfacial Electrochemistry* 52.3 (May 1974), pp. 313–329. DOI: 10.1016/S0022-0728(74)80446-8. (Visited on 09/19/2026).

[70] Vladimir Tripkovic, Mårten E. Björketun, Egill Skúlason, and Jan Rossmeisl. “Standard hydrogen electrode and potential of zero charge in density functional calculations.” *Physical Review B* 84.11 (Sept. 2011), p. 115452. DOI: 10.1103/PhysRevB.84.115452. (Visited on 09/19/2026).

[71] Jun Haruyama, Tamio Ikeshoji, and Minoru Otani. “Electrode potential from density functional theory calculations combined with implicit solvation theory.” *Physical Review*

Materials 2.9 (Sept. 2018), p. 095801. DOI: 10.1103/PhysRevMaterials.2.095801. (Visited on 09/17/2026).

[72] Walther Nernst. "Die elektromotorische Wirksamkeit der Jonen." de. *Zeitschrift für Physikalische Chemie* 4U.1 (July 1889), pp. 129–181. DOI: 10.1515/zpch-1889-0412. (Visited on 09/19/2026).

[73] J. K. Nørskov, T. Bligaard, A. Logadottir, J. R. Kitchin, and Al Et. "Trends in the Exchange Current for Hydrogen Evolution." *Journal of The Electrochemical Society* (2005). DOI: 10.1149/1.1856988. (Visited on 09/19/2026).

[74] Andrew A. Peterson, Frank Abild-Pedersen, Felix Studt, Jan Rossmeisl, and Al Et. "How copper catalyzes the electroreduction of carbon dioxide into hydrocarbon fuels." *Energy & Environmental Science* (2010). DOI: 10.1039/c0ee00071j. (Visited on 09/19/2026).

[75] Kiran Mathew, Ravishankar Sundararaman, Kendra Letchworth-Weaver, T. A. Arias, and Richard G. Hennig. "Implicit solvation model for density-functional study of nanocrystal surfaces and reaction pathways." *The Journal of Chemical Physics* 140.8 (Feb. 2014), p. 084106. DOI: 10.1063/1.4865107. (Visited on 09/19/2026).

[76] Kiran Mathew, V. S. Chaitanya Kolluru, Srinidhi Mula, Stephan N. Steinmann, and Richard G. Hennig. "Implicit self-consistent electrolyte model in plane-wave density-functional theory." *The Journal of Chemical Physics* 151.23 (Dec. 2019), p. 234101. DOI: 10.1063/1.5132354. (Visited on 09/19/2026).

[77] Oliviero Andreussi, Ismaila Dabo, and Nicola Marzari. "Revised self-consistent continuum solvation in electronic-structure calculations." *The Journal of Chemical Physics* 136.6 (Feb. 2012), p. 064102. DOI: 10.1063/1.3676407. (Visited on 09/19/2026).

[78] S. M. Rezwanul Islam, Foroogh Khezeli, Stefan Ringe, and Craig Plaisance. "An implicit electrolyte model for plane wave density functional theory exhibiting nonlinear response and a nonlocal cavity definition." *The Journal of Chemical Physics* 159.23 (Dec. 2023), p. 234117. DOI: 10.1063/5.0176308. (Visited on 09/19/2026).

[79] Itamar Borukhov, David Andelman, and Henri Orland. "Steric Effects in Electrolytes: A Modified Poisson-Boltzmann Equation." *Physical Review Letters* 79.3 (July 1997), pp. 435–438. DOI: 10.1103/PhysRevLett.79.435. (Visited on 09/19/2026).

[80] Oliviero Andreussi, Nicolas Georg Hörmann, Francesco Nattino, Giuseppe Fisicaro, Stefan Goedecker, and Nicola Marzari. "Solvent-Aware Interfaces in Continuum Solvation." *Journal of Chemical Theory and Computation* 15.3 (Mar. 2019), pp. 1996–2009. DOI: 10.1021/acs.jctc.8b01174. (Visited on 09/19/2026).

[81] Ravishankar Sundararaman, William A. Goddard III, and Tomas A. Arias. "Grand canonical electronic density-functional theory: Algorithms and applications to electrochemistry." *The Journal of Chemical Physics* 146.11 (Mar. 2017), p. 114104. DOI: 10.1063/1.4978411. (Visited on 09/19/2026).

[82] Nicolas G. Hörmann, Oliviero Andreussi, and Nicola Marzari. "Grand canonical simulations of electrochemical interfaces in implicit solvation models." *The Journal of Chemical Physics* 150.4 (Jan. 2019), p. 041730. DOI: 10.1063/1.5054580. (Visited on 09/19/2026).

[83] Nicolas G. Hörmann, Simeon D. Beinlich, and Karsten Reuter. "Converging Divergent Paths: Constant Charge vs Constant Potential Energetics in Computational Electrochemistry." *The Journal of Physical Chemistry C* 128.13 (Apr. 2024), pp. 5524–5531. DOI: 10.1021/acs.jpcc.3c07954. (Visited on 09/19/2026).

[84] Nicolas G. Hörmann, Nicola Marzari, and Karsten Reuter. "Electrosorption at metal surfaces from first principles." en. *npj Computational Materials* 6.1 (Sept. 2020), p. 136. DOI: 10.1038/s41524-020-00394-4. (Visited on 09/19/2026).

[85] Simeon D. Beinlich, Georg Kastlunger, Karsten Reuter, and Nicolas G. Hörmann. "Controlled Electrochemical Barrier Calculations without Potential Control." *Journal of Chemical Theory and Computation* 19.22 (Nov. 2023), pp. 8323–8331. DOI: 10.1021/acs.jctc.3c00836. (Visited on 09/19/2026).

[86] Devin T. Whipple and Paul J. A. Kenis. "Prospects of CO2 Utilization via Direct Heterogeneous Electrochemical Reduction." *The Journal of Physical Chemistry Letters* 1.24 (Dec. 2010), pp. 3451–3458. DOI: 10.1021/jz1012627. (Visited on 09/19/2026).

[87] Yoshio Hori, Katsuhei Kikuchi, and Shin Suzuki. "PRODUCTION OF CO AND CH4 IN ELECTROCHEMICAL REDUCTION OF CO2 AT METAL ELECTRODES IN AQUEOUS HYDROGENCARBONATE SOLUTION." *Chemistry Letters* 14.11 (Nov. 1985), pp. 1695–1698. DOI: 10.1246/cl.1985.1695. (Visited on 09/19/2026).

[88] Brian Seger, Georg Kastlunger, Alexander Bagger, and Soren B. Scott. "A Perspective on the Reaction Mechanisms of CO2 Electrolysis." *ACS Energy Letters* 10.5 (May 2025), pp. 2212–2227. DOI: 10.1021/acsenergylett.4c03599. (Visited on 09/19/2026).

[89] Sunmoon Yu, Sheena Louisia, and Peidong Yang. "The Interactive Dynamics of Nanocatalyst Structure and Microenvironment during Electrochemical CO_2 Conversion." en. *JACS Au* 2.3 (Mar. 2022), pp. 562–572. DOI: 10.1021/jacsau.1c00562. (Visited on 09/20/2026).

[90] Pierre van Rysselberghe, George J. Alkire, and John M. McGee. "Polarographic Reduction of Carbon Dioxide. III. Description and Interpretation of the Waves1." *Journal of the American Chemical Society* 68.10 (Oct. 1946), pp. 2050–2055. DOI: 10.1021/ja01214a053. (Visited on 09/20/2026).

[91] Truman E. Teeter and Pierre Van Rysselberghe. "Reduction of Carbon Dioxide on Mercury Cathodes." *The Journal of Chemical Physics* 22.4 (Apr. 1954), pp. 759–760. DOI: 10.1063/1.1740178. (Visited on 09/20/2026).

[92] M. Gattrell, N. Gupta, and A. Co. "A review of the aqueous electrochemical reduction of CO2 to hydrocarbons at copper." *Journal of Electroanalytical Chemistry* 594.1 (Aug. 2006), pp. 1–19. DOI: 10.1016/j.jelechem.2006.05.013. (Visited on 09/19/2026).

[93] Andrew A. Peterson and Jens K. Nørskov. "Activity Descriptors for CO_2 Electroreduction to Methane on Transition-Metal Catalysts." en. *The Journal of Physical Chemistry Letters* 3.2 (Jan. 2012), pp. 251–258. DOI: 10.1021/jz201461p. (Visited on 09/20/2026).

[94] Kendra P. Kuhl, Etosha R. Cave, David N. Abram, and Thomas F. Jaramillo. "New insights into the electrochemical reduction of carbon dioxide on metallic copper surfaces." en. *Energy & Environmental Science* 5.5 (2012), p. 7050. DOI: 10.1039/c2ee21234j. (Visited on 09/20/2026).

[95] Colin P. O'Brien, Rui Kai Miao, Ali Shayesteh Zeraati, Geonhui Lee, Edward H. Sargent, and David Sinton. "CO2 Electrolyzers." *Chemical Reviews* 124.7 (Apr. 2024), pp. 3648–3693. DOI: 10.1021/acs.chemrev.3c00206. (Visited on 09/19/2026).

[96] Jianfeng Huang, Nicolas Hörmann, Emad Oveisi, Anna Loiudice, Gian Luca De Gregorio, Oliviero Andreussi, Nicola Marzari, and Raffaella Buonsanti. "Potential-induced nanoclustering of metallic catalysts during electrochemical CO2 reduction." en. *Nature*

Communications 9.1 (Aug. 2018), p. 3117. DOI: 10.1038/s41467-018-05544-3. (Visited on 09/20/2026).

[97] Jesse Kok, Petru P. Albertini, Jari Leemans, Raffaella Buonsanti, and Thomas Burdyny. "Overcoming copper stability challenges in CO2 electrolysis." en. *Nature Reviews Materials* 10.7 (July 2025), pp. 550–563. DOI: 10.1038/s41578-025-00815-0. (Visited on 09/20/2026).

[98] Maxime Van den Bossche, Christoph Rose-Petruck, and Hannes Jónsson. "Competing HCOOH and CO Pathways in CO2 Electroreduction at Copper Electrodes: Calculations of Voltage-Dependent Activation Energy." *The Journal of Physical Chemistry C* 125.25 (July 2021), pp. 13802–13808. DOI: 10.1021/acs.jpcc.1c01481. (Visited on 10/12/2026).

[99] Michele Re Fiorentin, Francesca Risplendi, Clara Salvini, Juqin Zeng, Giancarlo Cicero, and Hannes Jónsson. "Silver Electrodes Are Highly Selective for CO in CO2 Electroreduction due to Interplay between Voltage Dependent Kinetics and Thermodynamics." *The Journal of Physical Chemistry Letters* 15.46 (Nov. 2024), pp. 11538–11545. DOI: 10.1021/acs.jpclett.4c02869. (Visited on 10/12/2026).

[100] Javed Hussain, Hannes Jónsson, and Egill Skúlason. "Calculations of Product Selectivity in Electrochemical CO2 Reduction." *ACS Catalysis* 8.6 (June 2018), pp. 5240–5249. DOI: 10.1021/acscatal.7b03308. (Visited on 09/20/2026).

[101] Jung Yoon 'Timothy' Kim, Chase Sellers, Shaoyun Hao, Thomas P. Senftle, and Haotian Wang. "Different distributions of multi-carbon products in CO2 and CO electroreduction under practical reaction conditions." en. *Nature Catalysis* 6.12 (Dec. 2023), pp. 1115–1124. DOI: 10.1038/s41929-023-01082-4. (Visited on 09/20/2026).

[102] Philipp Grosse, Dunfeng Gao, Fabian Scholten, Ilya Sinev, Hemma Mistry, and Beatriz Roldan Cuenya. "Dynamic Changes in the Structure, Chemical State and Catalytic Selectivity of Cu Nanocubes during CO2 Electroreduction: Size and Support Effects." en. *Angewandte Chemie* 130.21 (2018), pp. 6300–6305. DOI: 10.1002/ange.201802083. (Visited on 09/21/2026).

[103] Klaas Jan P. Schouten, Zisheng Qin, Elena Pérez Gallent, and Marc T. M. Koper. "Two Pathways for the Formation of Ethylene in CO Reduction on Single-Crystal Copper Electrodes." en. *Journal of the American Chemical Society* 134.24 (June 2012), pp. 9864–9867. DOI: 10.1021/ja302668n. (Visited on 09/09/2026).

[104] Christopher Hahn, Toru Hatsukade, Youn-Geun Kim, Arturas Vailionis, Jack H. Baricuatro, Drew C. Higgins, Stephanie A. Nitopi, Manuel P. Soriaga, and Thomas F. Jaramillo. "Engineering Cu surfaces for the electrocatalytic conversion of CO2: Controlling selectivity toward oxygenates and hydrocarbons." *Proceedings of the National Academy of Sciences* 114.23 (June 2017), pp. 5918–5923. DOI: 10.1073/pnas.1618935114. (Visited on 09/21/2026).

[105] Rulle Reske, Hemma Mistry, Farzad Behafarid, Beatriz Roldan Cuenya, and Peter Strasser. "Particle Size Effects in the Catalytic Electroreduction of CO2 on Cu Nanoparticles." *Journal of the American Chemical Society* 136.19 (May 2014), pp. 6978–6986. DOI: 10.1021/ja500328k. (Visited on 09/22/2026).

[106] Hemma Mistry, Farzad Behafarid, Rulle Reske, Ana Sofia Varela, Peter Strasser, and Beatriz Roldan Cuenya. "Tuning Catalytic Selectivity at the Mesoscale via Interparticle Interactions." *ACS Catalysis* 6.2 (Feb. 2016), pp. 1075–1080. DOI: 10.1021/acscatal.5b02202. (Visited on 09/22/2026).

[107] Hemma Mistry, Ana Sofia Varela, Cecile S. Bonifacio, Ioannis Zegkinoglou, Ilya Sinev, Yong-Wook Choi, Kim Kisslinger, Eric A. Stach, Judith C. Yang, Peter Strasser, and Beatriz Roldan Cuenya. "Highly selective plasma-activated copper catalysts for carbon dioxide reduction to ethylene." en. *Nature Communications* 7.1 (June 2016), p. 12123. DOI: 10.1038/ncomms12123. (Visited on 09/22/2026).

[108] Jan Vavra, Gaétan P. L. Ramona, Federico Dattila, Attila Kormányos, Tatiana Priamushko, Petru P. Albertini, Anna Loiudice, Serhiy Cherevko, Núria Lopéz, and Raffaella Buonsanti. "Solution-based Cu+ transient species mediate the reconstruction of copper electrocatalysts for CO2 reduction." en. *Nature Catalysis* 7.1 (Jan. 2024), pp. 89–97. DOI: 10.1038/s41929-023-01070-8. (Visited on 09/22/2026).

[109] Jie Wei, Zisheng Zhang, Winston Gee, Yu Wei, Ya-Wei Zhou, Matias Herran, Philippe Sautet, Anastassia N. Alexandrova, Beatriz Roldan Cuenya, and Christopher S. Kley. "Role of Surface Hydroxyls in Atomic-Scale Copper Restructuring during CO Electroreduction." *Journal of the American Chemical Society* 147.49 (Dec. 2025), pp. 45178–45188. DOI: 10.1021/jacs.5c14516. (Visited on 09/22/2026).

[110] Anna Wuttig, Can Liu, Qiling Peng, Momo Yaguchi, Christopher H. Hendon, Kenta Motobayashi, Shen Ye, Masatoshi Osawa, and Yogesh Surendranath. "Tracking a Common Surface-Bound Intermediate during CO2-to-Fuels Catalysis." *ACS Central Science* 2.8 (Aug. 2016), pp. 522–528. DOI: 10.1021/acscentsci.6b00155. (Visited on 09/22/2026).

[111] George Blyholder. "Molecular Orbital View of Chemisorbed Carbon Monoxide." *The Journal of Physical Chemistry* 68.10 (Oct. 1964), pp. 2772–2777. DOI: 10.1021/j100792a006. (Visited on 09/22/2026).

[112] B. Hammer, Y. Morikawa, and J. K. Nørskov. "CO Chemisorption at Metal Surfaces and Overlayers." *Physical Review Letters* 76.12 (Mar. 1996), pp. 2141–2144. DOI: 10.1103/PhysRevLett.76.2141. (Visited on 09/22/2026).

[113] Paul Sabatier. *Nobel Prize in Chemistry 1912*. en-US. 1912. (Visited on 09/25/2026).

[114] T. Bligaard, J. K. Nørskov, S. Dahl, J. Matthiesen, C. H. Christensen, and J. Sehested. "The Brønsted–Evans–Polanyi relation and the volcano curve in heterogeneous catalysis." *Journal of Catalysis* 224.1 (May 2004), pp. 206–217. DOI: 10.1016/j.jcat.2004.02.034. (Visited on 09/25/2026).

[115] Marc T. M. Koper. "Thermodynamic theory of multi-electron transfer reactions: Implications for electrocatalysis." *Journal of Electroanalytical Chemistry*. Physics and Chemistry of Charge Transfer in Condensed Media 660.2 (Sept. 2011), pp. 254–260. DOI: 10.1016/j.jelechem.2010.10.004. (Visited on 09/25/2026).

[116] Georg Kastlunger. "Electrocatalysts Beyond Copper for CO2 Reduction to Multicarbon Products From Systematic First Principle-Based Screening." en. *ChemCatChem* 18.5 (2026), e01744. DOI: 10.1002/cctc.202501744. (Visited on 09/25/2026).

[117] Magnus A. H. Christiansen, Alejandro Peña-Torres, Elvar Ö. Jónsson, and Hannes Jónsson. "Single-Atom Substituents in Copper Surfaces May Adsorb Multiple CO Molecules." en. *The Journal of Physical Chemistry Letters* 15.21 (May 2024), pp. 5654–5658. DOI: 10.1021/acs.jpclett.4c00899. (Visited on 09/07/2026).

[118] Magnus A. H. Christiansen, Wei Wang, Elvar Ö. Jónsson, Giancarlo Cicero, and Hannes Jónsson. "Multiple Adsorption of CO Molecules on Transition Metal Substitutional Impurities in Copper Surfaces." en. *ChemCatChem* 17.18 (Sept. 2025), e00765. DOI: 10.1002/cctc.202500765. (Visited on 09/07/2026).

[119] Kin L. Wong, Bommisetty V. Rao, Greg Pawin, Erick Ulin-Avila, and Ludwig Bartels. "Coverage and nearest-neighbor dependence of adsorbate diffusion." *The Journal of Chemical Physics* 123.20 (Nov. 2005), p. 201102. DOI: 10.1063/1.2124687. (Visited on 09/22/2026).

[120] Christopher Zaum and Karina Morgenstern. "Experimental Evidence for a Three-Body Interaction between Diffusing CO Molecules." *Nano Letters* 16.5 (May 2016), pp. 3001–3004. DOI: 10.1021/acs.nanolett.5b05212. (Visited on 09/22/2026).

[121] Robert B. Sandberg, Joseph H. Montoya, Karen Chan, and Jens K. Nørskov. "CO-CO coupling on Cu facets: Coverage, strain and field effects." *Surface Science* 654 (Dec. 2016), pp. 56–62. DOI: 10.1016/j.susc.2016.08.006. (Visited on 09/22/2026).

[122] Joseph H. Montoya, Chuan Shi, Karen Chan, and Jens K. Nørskov. "Theoretical Insights into a CO Dimerization Mechanism in CO2 Electroreduction." *The Journal of Physical Chemistry Letters* 6.11 (June 2015), pp. 2032–2037. DOI: 10.1021/acs.jpclett.5b00722. (Visited on 09/23/2026).

[123] Elena Pérez-Gallent, Marta C. Figueiredo, Federico Calle-Vallejo, and Marc T. M. Koper. "Spectroscopic Observation of a Hydrogenated CO Dimer Intermediate During CO Reduction on Cu(100) Electrodes." en. *Angewandte Chemie International Edition* 56.13 (2017), pp. 3621–3624. DOI: 10.1002/anie.201700580. (Visited on 09/23/2026).

[124] Jason D. Goodpaster, Alexis T. Bell, and Martin Head-Gordon. "Identification of Possible Pathways for C–C Bond Formation during Electrochemical Reduction of CO2: New Theoretical Insights from an Improved Electrochemical Model." *The Journal of Physical Chemistry Letters* 7.8 (Apr. 2016), pp. 1471–1477. DOI: 10.1021/acs.jpclett.6b00358. (Visited on 09/23/2026).

[125] Erlend Bertheussen, Arnau Verdaguer-Casadevall, Davide Ravasio, Joseph H. Montoya, Daniel B. Trimarco, Claudie Roy, Sebastian Meier, Jürgen Wendland, Jens K. Nørskov, Ifan E. L. Stephens, and Ib Chorkendorff. "Acetaldehyde as an Intermediate in the Electroreduction of Carbon Monoxide to Ethanol on Oxide-Derived Copper." en. *Angewandte Chemie International Edition* 55.4 (2016), pp. 1450–1454. DOI: 10.1002/anie.201508851. (Visited on 09/23/2026).

[126] Hendrik H. Heenen, Haeun Shin, Georg Kastlunger, Sean Overa, Joseph A. Gauthier, Feng Jiao, and Karen Chan. "The mechanism for acetate formation in electrochemical CO(2) reduction on Cu: selectivity with potential, pH, and nanostructuring." *Energy & Environmental Science* 15.9 (Sept. 2022), pp. 3978–3990. DOI: 10.1039/d2ee01485h. (Visited on 09/23/2026).

[127] Di Tian, Zefeng Wang, Zhou Xu, Yiquan Zhu, Yan Yan, Jifeng Yang, Siyuan He, Zaibin Xue, Zhenzhen Wang, Kang Li, Wenxuan Fan, Miaomiao Xue, Zehua Qu, Wei Xia, and Mingkai Liu. "Elevating CO2 selective conversion: Insights into copper-based single atom alloy catalysts." en. *Advanced Composites and Hybrid Materials* 8.1 (Dec. 2024), p. 49. DOI: 10.1007/s42114-024-01105-z. (Visited on 09/23/2026).

[128] Wenjie Wu, Jun Long, and Jianping Xiao. "Recent Advances in Electrochemical CO2 Reduction Catalyzed by Single-Atom Alloys." en. *ChemCatChem* 17.6 (2025), e202401785. DOI: 10.1002/cctc.202401785. (Visited on 09/23/2026).

[129] Georgios Kyriakou, Matthew B. Boucher, April D. Jewell, Emily A. Lewis, Timothy J. Lawton, Ashleigh E. Baber, Heather L. Tierney, Maria Flytzani-Stephanopoulos, and E. Charles H. Sykes. "Isolated Metal Atom Geometries as a Strategy for Selective Heterogeneous Hydrogenations." *Science* 335.6073 (Mar. 2012), pp. 1209–1212. DOI: 10.1126/science.1215864. (Visited on 09/23/2026).

[130] Zehua Jin, Yuting Xu, Manjeet Chhetri, Julia Wood, Brian Torreon, Fanglin Che, and Ming Yang. "Recent developments of single atom alloy catalysts for electrocatalytic hydrogenation reactions." *Chemical Engineering Journal* 491 (July 2024), p. 152072. DOI: 10.1016/j.cej.2024.152072. (Visited on 09/23/2026).

[131] Mao Ding, Zhaoyang Chen, Chunxiao Liu, Youpeng Wang, Chengbo Li, Xu Li, Tingting Zheng, Qiu Jiang, and Chuan Xia. "Electrochemical CO2 reduction: Progress and opportunity with alloying copper." *Materials Reports: Energy*. Special Issue on CO Reductions to Fuels and Carbon Feedstocks (Part 1) 3.1 (Feb. 2023), p. 100175. DOI: 10.1016/j.matre.2023.100175. (Visited on 09/23/2026).

[132] M. T. Greiner, T. E. Jones, S. Beeg, L. Zwiener, M. Scherzer, F. Girgsdies, S. Piccinin, M. Armbrüster, A. Knop-Gericke, and R. Schlögl. "Free-atom-like d states in single-atom alloy catalysts." en. *Nature Chemistry* 10.10 (Oct. 2018), pp. 1008–1015. DOI: 10.1038/s41557-018-0125-5. (Visited on 09/23/2026).

[133] Fabian Berger, Julia Schumann, Romain Réocreux, Michail Stamatakis, and Angelos Michaelides. "Bringing Molecules Together: Synergistic Coadsorption at Dopant Sites of Single Atom Alloys." en. *Journal of the American Chemical Society* (Oct. 2024), jacs.4c07621. DOI: 10.1021/jacs.4c07621. (Visited on 09/23/2026).

[134] Juan Pablo Simonovis, Adrian Hunt, Robert M. Palomino, Sanjaya D. Senanayake, and Iradwikanari Waluyo. "Enhanced Stability of Pt-Cu Single-Atom Alloy Catalysts: In Situ Characterization of the Pt/Cu(111) Surface in an Ambient Pressure of CO." *The Journal of Physical Chemistry C* 122.8 (Mar. 2018), pp. 4488–4495. DOI: 10.1021/acs.jpcc.8b00078. (Visited on 09/23/2026).

[135] Matthew T. Darby, E. Charles H. Sykes, Angelos Michaelides, and Michail Stamatakis. "Carbon Monoxide Poisoning Resistance and Structural Stability of Single Atom Alloys." en. *Topics in Catalysis* 61.5 (May 2018), pp. 428–438. DOI: 10.1007/s11244-017-0882-1. (Visited on 09/23/2026).

[136] Tianfu Liu, Guohui Song, Xiaoju Liu, Zhou Chen, Yu Shen, Qi Wang, Zhangquan Peng, and Guoxiong Wang. "Insights into the Mechanism in Electrochemical CO_2 Reduction over Single-Atom Copper Alloy Catalysts: A DFT Study." *iScience* 26 (10 2023), p. 107953. DOI: 10.1016/j.isci.2023.107953.

[137] G. Kresse and J. Furthmüller. "Efficient Iterative Schemes for Ab Initio Total-Energy Calculations Using a Plane-Wave Basis Set." *Phys. Rev. B* 54 (16 Oct. 1996), pp. 11169–11186. DOI: 10.1103/PhysRevB.54.11169.

[138] G. Kresse and D. Joubert. "From Ultrasoft Pseudopotentials to the Projector Augmented-Wave Method." *Phys. Rev. B* 59 (3 Jan. 1999), pp. 1758–1775. DOI: 10.1103/PhysRevB.59.1758.

[139] Zisheng Zhang, Winston Gee, Philippe Sautet, and Anastassia N. Alexandrova. "H and CO Co-Induced Roughening of Cu Surface in CO2 Electroreduction Conditions." *Journal of the American Chemical Society* 146.23 (June 2024), pp. 16119–16127. DOI: 10.1021/jacs.4c03515. (Visited on 10/12/2026).

Appendix A: Publications

Publication I

Single-Atom Substituents in Copper Surfaces May Adsorb Multiple CO Molecules

Magnus A. H. Christiansen, Alejandro Peña-Torres, Elvar Ö. Jónsson, and Hannes Jónsson

J. Phys. Chem. Lett. 15, 5654–5658 (2024)

Used with permission; see publisher terms.

THE JOURNAL OF PHYSICAL CHEMISTRY LETTERS
A JOURNAL OF THE AMERICAN CHEMICAL SOCIETY

pubs.acs.org/JPCL Letter

Single-Atom Substituents in Copper Surfaces May Adsorb Multiple CO Molecules

Magnus A. H. Christiansen,* Alejandro Peña-Torres, Elvar Ö. Jónsson, and Hannes Jónsson*

Cite This: J. Phys. Chem. Lett. 2024, 15, 5654−5658 Read Online

ACCESS | Metrics & More | Article Recommendations | Supporting Information

ABSTRACT: Copper is a good CO_2 electroreduction catalyst as products beyond CO form, but efficiency and selectivity is low. Experiments have shown that an admixture of other elements can help, and computational screening studies have pointed out various promising candidates based on the adsorption of a single CO molecule as a descriptor. Our calculations of CO adsorption on surfaces where a first row transition metal atom replaces a Cu atom show that multiple CO molecules, not just one, bind to the substitutional atom. For Fe, Co, and Ni atoms, a decrease in binding energy is found, but the reverse trend, namely, increasing bond strength, is found for V, Cr, and Mn and the first three CO molecules. Magnetic moment, charge, and position of the substitutional atom are also strongly affected by the CO adsorption in most cases. Magnetic moment is stepwise reduced to zero, and the outward displacement of the substitutional atom increased.

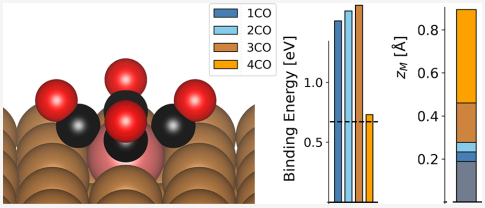

The electrochemical reduction reaction of CO_2, referred to as CO2RR, is a promising way of converting CO_2 into useful products.[1,2] Depending on the electrode material, various products can be formed, e.g., formic acid, CO, and further reduced products including methane and even C_2 products, such as ethylene (see, for example, Rhimi et al.[3] for a recent review). Remarkably, more ethylene than C_1 products are formed at the Cu(100) surface for a certain range of applied voltage.[4] A two-parameter descriptor based on the binding energy of a CO admolecule and of an H adatom on the surface of the catalyst has been proposed as a measure for predicting the products formed in CO2RR.[5,6] Copper electrodes are particularly promising, as the CO intermediate binds strongly enough to the surface to become reduced further, while the coverage of hydrogen is low enough for the hydrogen evolution reaction not to dominate when the magnitude of the applied voltage is in the right window.[5] Formation of formate is a competing reaction path that terminates as the anion is repelled from the negatively charged electrode surface.[7] The efficiency and selectivity for specific products need to be improved, though, in order for the process to become economical.

There have been reports of experiments where improved efficiency and/or selectivity is obtained by adding other elements as substitutional impurities, for example, cobalt[8,9] and nickel.[10] Even with a low surface concentration of the added element, the reaction pathway and overpotential needed for CO2RR can be modified substantially. Such copper-based surfaces with a small amount of substitutional impurities can be regarded as examples of a wider class of catalysts referred to as single-atom alloys (SAAs) where individual atoms of more reactive element, such as Pt, Fe, Co, or Ni, are embedded in a matrix of a less reactive element, copper in the present case.[11−13]

In an effort to search for better CO2RR electrocatalysts, the adsorption energy of a CO molecule on the surface has been used as a key indicator, and the calculations are typically carried out using density functional theory (DFT) (see, for example, Liu et al.[14]). From a large number of such calculations, machine learned models are being developed for predicting the adsorption energy of a CO molecule on copper surfaces modified by introducing a wide range of other elements.[15] Following the Sabatier principle, a good catalyst should have the right balance between keeping the intermediates on the surface and releasing the products. The binding of a CO molecule is taken to be a good descriptor for any intermediate where a C atom binds to the surface, such as, for example, OCOH, COH, and CH_3, and the search for a better CO2RR catalyst has therefore focused on finding the optimal value for the binding energy of a single CO molecule on the catalyst surface.

There are, however, some indications that more than one CO molecule can adsorb on a transition metal substitution atom on a copper surface. Adsorption of two CO molecules

Received: March 26, 2024
Revised: April 29, 2024
Accepted: May 3, 2024
Published: May 20, 2024



ACS Publications © 2024 American Chemical Society

https://doi.org/10.1021/acs.jpclett.4c00899
J. Phys. Chem. Lett. 2024, 15, 5654−5658

Downloaded from pubs.acs.org/jpclcd/article-pdf/15/21/5654/3368947/jz4c00899.pdf by NATL AND UNIV LBRY OF ICELAND user on 07 September 2026

has been experimentally observed for Cu surfaces doped with either Co[16] or with Rh,[17] and this has been supported by DFT calculations. This indicates that in order to apply the Sabatier principle correctly and assess the catalytic performance, one needs to consider the adsorption of whatever number of CO molecules is expected to be present under reaction conditions, not just the adsorption of the first CO. It is then more likely that the binding energy of the last adsorbed CO molecule on the substitutional atom will be a useful descriptor of the CO2RR catalytic performance.

Here, the adsorption of multiple CO molecules on substitutional atoms from the first row of transition metals left of copper in the periodic table is studied using DFT calculations for Cu(100) and Cu(111) surfaces. The structure and energy for up to four CO admolecules are found, and in some cases the 4th CO admolecule binds more strongly on the substitutional atom than on the pure copper surface. This shows that it is essential to consider the binding of multiple CO molecules in order to assess the CO2RR catalytic performance. Various properties such as magnetic moment, charge transfer, and outward displacement of the substitutional atom are strongly affected by the CO adsorption. In a broader context, our results can be relevant for SAA catalysts of other reactions in that one should be careful to consider the possibility of multiple admolecules binding to the same site.

Figure 1 shows the structure obtained when a vanadium atom is placed in the Cu(100) surface layer and up to 4 CO

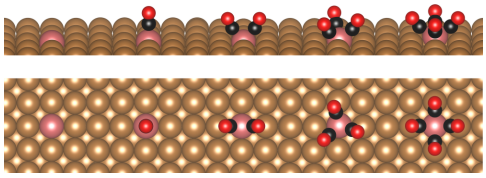

Figure 1. Minimum energy structure of the Cu(100) surface where one of the Cu atoms has been replaced with a V atom (pink) and then 1, 2, 3, and 4 CO molecules adsorbed on the V atom (O atom red, C atom black). Even the fourth CO molecule is bound more strongly to the V atom than on the pure Cu(100) surface.

molecules bind to it. Even the fourth CO molecule binds more strongly to the V atom than to the clean Cu(100) surface. However, on the Cu(111) surface, the 4th CO molecule is bound more strongly on the copper surface than on the V atom.

Figure 2a shows the calculated differential binding energy, $E_{b\text{-}n^{th}CO/M@Cu}$ (see Methods), for CO on Sc, Ti, V, Cr, Mn, Fe, Co, and Ni substitutional atom in Cu(100). Analogous results for Cu(111) are shown in Figure 2b. The binding energy of a single CO molecule on the corresponding pure Cu surface is shown for comparison. The differential binding energy gives the change in the total energy as the nth CO molecule coming from the gas phase adsorbs on the substitutional atom with $n-1$ CO molecules present already. The differential binding energy in most cases depends strongly on the number of CO admolecules.

For Fe, Co, and Ni, the differential binding energy decreases as more CO molecules are adsorbed. This is the expected trend; the more bonds are formed to a given atom, the weaker each bond is. For both the (111) and (100) facets, the Fe and

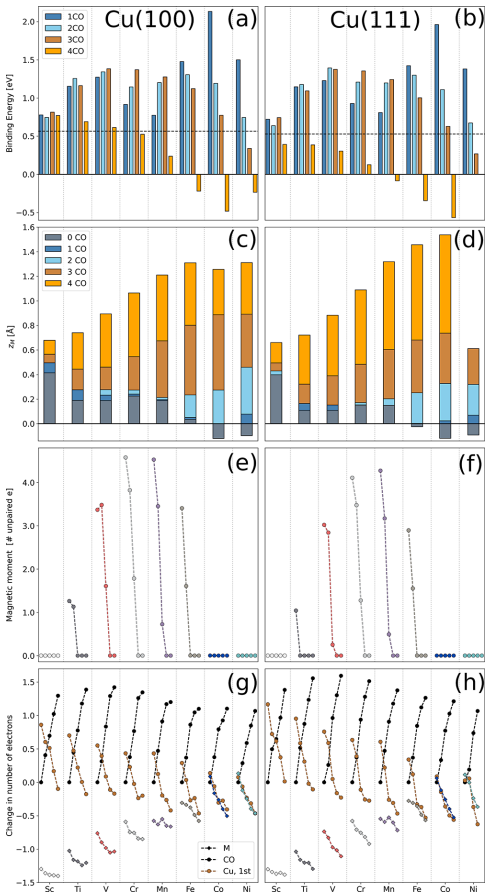

Figure 2. Left: Cu(100). Right: Cu(111). (a and b) Differential binding energy, $E_{b\text{-}n^{th}CO/M@Cu}$, of a CO molecule adsorbed on a substituent atom, M. Up to 4 CO molecules are adsorbed on a single M atom. The black dashed lines indicate the binding energy of a CO molecule on the pure copper surfaces. (c and d) Position of the M atom with respect to the surface plane (z-coordinate) when no and up to 4 CO molecules are adsorbed. (e and f) Total magnetic moment of the simulated system, $(CO)_n$-M@Cu, indicating the number of unpaired electrons. (g and h) Change in the number of electrons associated with the M atom, the first neighboring surface Cu atoms, and CO molecules adsorbed on M for varying number of adsorbed CO molecules, based on Bader analysis.

Co atoms can bind three CO molecules more strongly than the pure copper surface. While there is a local minimum on the energy surface for the adsorption of a 4th molecule, the energy of the system is lowered by placing the molecule on the copper surface far from the substitutional atom. For Ni, 2 CO molecules adsorb more strongly than on the pure copper surface. The variation in differential binding energy is particularly large for Co and Ni, where the second CO

https://doi.org/10.1021/acs.jpclett.4c00899
J. Phys. Chem. Lett. 2024, 15, 5654−5658

Downloaded from pubs.acs.org/jpclcd/article-pdf/15/21/5654/3368947/jz4c00899.pdf by NATL AND UNIV LBRY OF ICELAND user on 07 September 2026

molecule has a binding energy nearly 1 eV lower than that of the first one.

An opposite trend is found for the differential binding energy on Cr and Mn atoms, as it increases for the first three CO molecules. This is unusual. The 4th CO binds less strongly than on the pure copper surface. An analysis of the electronic structure changes associated with the CO adsorption is discussed below. For Sc, Ti, and V the differential binding energy is rather constant for the first three CO admolecules, but it decreases for the 4th one. Sc on the Cu(100) surface is an exception in that all four CO molecules have similar binding energy. The Sc, Ti, and V atoms in a Cu(100) surface are special in that the 4th CO admolecule binds more strongly than on the pure copper surface.

The substitutional atoms are displaced outward with respect to the surface plane as the CO molecules adsorb. This is shown in Figure 2c,d for the Cu(100) and Cu(111) surfaces, respectively. The position of the substitutional atom in the direction normal to the surface, with respect to the average position of the Cu atoms in the surface layer of the M@Cu system, is displayed. Sc being the largest of the first row transition metal atoms, it is displaced outward by 0.4 Å even in the absence of CO admolecules. The adsorption of CO increases the displacement only slightly, by ca. 0.1 Å, except for the second CO admolecule. On the other end of the sequence, the Co and Ni atoms are relatively smaller, and they are ca. 0.1 Å lower than the surface Cu atoms in the absence of CO. In all cases, the adsorption of CO leads to outward displacement of the substitutional atoms. As the 4th CO molecule is adsorbed, the outward displacement can be greater than 1.5 Å. We note that it is in some cases important to first displace the substitutional atom outward as a new CO molecule is added before carrying out local energy minimization in order to find the global or local energy minimum corresponding to the increased number of CO admolecules.

The calculated magnetic moment, indicating the number of unpaired d-electrons, is shown in Figure 2e,f. As the number of CO admolecules increases, the magnetic moment, in most cases, decreases strongly. The reason for this appears to be a shift in the energy of the d-orbitals of the substitutional atoms as the CO molecules adsorb. This is to be expected since CO is a strong ligand. For Sc, Co, and Ni the magnetic moment is zero and remains unchanged. The transfer of electrons is estimated using Bader analysis, and the results are shown in Figure 2g,f. Electrons get transferred to the CO admolecules, mainly from the adjacent Cu atoms but also from the substitutional atom. This electron transfer likely also contributes to the changes in the magnetic moment.

The calculated results presented here show that several CO molecules can be bound to a first row transition metal substituent atom on (111) and (100) copper surfaces. The differential binding energy varies in most cases significantly, as more CO molecules are adsorbed. This means that the binding of a single CO molecule is not likely to be a good descriptor of the CO2RR activity. Copper is known to be a good electrocatalyst for CO_2 reduction because the affinity for admolecules is just about right, strong enough for the CO to remain on the surface at room temperature while the binding of H-adatoms is weak enough for the hydrogen evolution reaction not to dominate.[5] The C−C bond formation is known to be particularly efficient on Cu(100), and an interesting question is the possible reaction of a CO bound to a substitutional atom with a CO molecule bound on nearby sites formed by Cu atoms. By analogy, only the rather weakly bound CO molecules on the substitutional atoms are most likely to react to form C_2 products. The strongly bound CO molecules are unlikely to be reactive.

For the Cu(100) surface, it is the 4th CO molecule on Ti, V, or Cr that has a differential binding energy close to that of CO on the pure Cu(100). The 3rd CO molecule on Co and the 2nd on Ni are close but bind a bit too strongly, as are all CO molecules adsorbed on Sc. None of the CO molecules adsorbed on a Mn or Fe substitutional atom have differential binding energy in the right range. The first CO bound to Mn is only a bit too strongly bound, but the second and third CO molecules bind so strongly that the most stable situation is three strongly bound and chemically inactive CO admolecules. For the Cu(111) surface, only the 3rd CO molecule on Co and the 2nd on Ni have a differential binding energy close to that of the pure copper surface. A stable structure with four CO molecules bound to the Ni atom in Cu(111) was not found.

The anomalous trend of increasing differential binding energy as additional CO molecules are adsorbed on Ti, V, Cr, and Mn substitutional atoms seems to be associated with changes in the magnetic moments; namely, a reduction in the number of unpaired electrons. The nonmagnetic Sc, Co, and Ni substitutional atoms in the copper surfaces show the expected trend of decreasing differential binding energy as the number of CO molecules is increased. A more detailed analysis of the bonding and electronic structure is called for to obtain a better understanding of these results.

The large outward displacement of the substitutional atoms as 3 and even 4 CO molecules are adsorbed, on the order of an Ångström, raises the question of whether the substitutional atom may leave the surface altogether as a carbonyl complex. This is an important issue, as the stability of electrocatalysts is equally important as efficiency. Again, further studies of this are in order and will be the subject of later reports.

The sites on the copper surface in the vicinity of the substitutional atom can also be modified as compared with analogous sites on a pure surface. This in itself could lead to changes in the CO2RR activity even if none of the CO molecules adsorbed on the substitutional atom are active. This requires additional calculations and will be addressed in later studies.

The main outcome of the studies presented here is a warning that should be kept in mind in the large computational effort now being undertaken in a search for an improved CO2RR catalyst by adding a minority component to copper and in studies of SAA catalysts in general. The binding energy of a single CO molecule on a transition metal substitutional atom on a copper surface is not likely to be a good descriptor of CO2RR activity. Multiple CO molecules can be bound, in most cases, too strongly to be reactive. The 3rd or even the 4th CO molecule adsorbed on the substitutional atom is more likely to be reactive than the first one. In some cases, the differential binding energy increases as more CO molecules are adsorbed, unlike the usual trend of bonds weakening as more bonds are formed. The reason for this appears to be related to the magnetic properties, i.e., reduction in the number of unpaired electrons.

METHODS

The calculations were carried out using spin-polarized density functional theory (DFT).[18] A plane-wave basis set with 450 eV cutoff energy was used to represent the valence electrons, in a

https://doi.org/10.1021/acs.jpclett.4c00899
J. Phys. Chem. Lett. 2024, 15, 5654−5658

Downloaded from pubs.acs.org/jpclcd/article-pdf/15/21/5654/3368947/jz4c00899.pdf by NATL AND UNIV LBRY OF ICELAND user on 07 September 2026

gamma-centered k-point grid of 4 × 4 × 1, while the effect of the inner electrons was included using the projector augmented wave (PAW) approach.[19] The revised Perdew–Burke–Ernzerhof (RPBE) functional approximation[20] was used as it is parametrized to give quite good agreement between calculated and measured energy of molecular adsorption on solid surfaces. The binding energy of a CO molecule on the clean Cu(100) and Cu(111) surfaces was found to be 0.57 and 0.53 eV, as compared with the experimental values of 0.53 and 0.49 eV.[21] The calculated lattice constant of the copper crystal comes out to be 3.70 Å, 2% larger than the experimental value.

The minimization of the energy is carried out using a conjugate gradient optimizer until the magnitude of all atomic forces drops below 0.01 eV/Å. The electronic structure optimization is carried out until self-consistency is reached at a level of 10^{-6} eV. The calculations are carried out using the Vienna *ab initio* simulation package (VASP).[22,23]

The substitutional atom is termed M, and the copper surface with a substitutional atom is referred to as M@Cu. In order to find the energy minimum for more than one CO molecule adsorbed on the substitutional atom, it sometimes needs to be lifted higher above the surface plane before local minimization of the energy is applied with respect to atom coordinates. A comparison is then made with the energy of the system when the added CO molecule is placed on a pure copper surface to determine whether adsorption on the substitutional atom is preferable.

The differential binding energy, i.e. energy gain/cost of adding the nth CO molecule coming from the gas phase, is calculated as

$$E_{\text{b-}n^{\text{th}}\text{CO/M@Cu}} = E_{(\text{CO})_n/\text{M@Cu}} - E_{(\text{CO})_{n-1}/\text{M@Cu}} - E_{\text{CO}}$$

where E_{CO} is the energy of an isolated CO molecule and $E_{(\text{CO})_n/\text{M@Cu}}$ is the value obtained for the total energy of the M@Cu surface with n CO molecules adsorbed. The energy of the converged $(\text{CO})_n$/M@Cu structures depends on the configuration of the CO molecules, with some surfaces having energy minimas for the CO molecules either pointing toward the hollow sites or bridge sites or pointing away perpendicular from the surface. All these configurations were considered with the initial structures of the structural optimization calculations.

The charge on the atoms was estimated using the Bader definition[24] implemented using a grid approach.[25]

■ ASSOCIATED CONTENT

Supporting Information

The Supporting Information is available free of charge at https://pubs.acs.org/doi/10.1021/acs.jpclett.4c00899.

Note on the geometry of an adsorbed CO; minimum energy structures (Figures S1 and S2); and tables of binding energy, outward displacement, and magnetic moment values (Tables S1 and S2) (PDF)

Transparent Peer Review report available (PDF)

■ AUTHOR INFORMATION

Corresponding Authors

Magnus A. H. Christiansen − *Science Institute and Faculty of Physical Sciences, U. of Iceland, 107 Reykjavík, Iceland;* orcid.org/0009-0004-9837-3469; Email: mah107@hi.is

Hannes Jónsson − *Science Institute and Faculty of Physical Sciences, U. of Iceland, 107 Reykjavík, Iceland;* orcid.org/0000-0001-8285-5421; Email: hj@hi.is

Authors

Alejandro Peña-Torres − *Science Institute and Faculty of Physical Sciences, U. of Iceland, 107 Reykjavík, Iceland;* orcid.org/0000-0001-8745-2912

Elvar Ö. Jónsson − *Science Institute and Faculty of Physical Sciences, U. of Iceland, 107 Reykjavík, Iceland;* orcid.org/0000-0001-6273-1237

Complete contact information is available at: https://pubs.acs.org/10.1021/acs.jpclett.4c00899

Notes

The authors declare no competing financial interest.

■ ACKNOWLEDGMENTS

This work was funded by the Icelandic Research Fund (Grant No. 207283-053) and the EU's Horizon 2021 programme under the Marie Skłodowska-Curie Doctoral Networks (MSCA-DN) Grant Agreement No. 101072830 (ECO-MATES). We thank Giancarlo Cicero, Kuber Rawat, and Kun Zhao for helpful discussions. Views and opinions expressed are those of the authors and do not necessarily reflect the official policy or position of the European Union or the Granting Authority, and neither can be held responsible for them.

■ REFERENCES

(1) Hori, Y.; Takahashi, I.; Koga, O.; Hoshi, N. Selective Formation of C2 Compounds from Electrochemical Reduction of CO_2 at a Series of Copper Single Crystal Electrodes. *J. Phys. Chem. B* **2002**, *106*, 15–17.

(2) Hori, Y.; Takahashi, I.; Koga, O.; Hoshi, N. Electrochemical Reduction of Carbon Dioxide at Various Series of Copper Single Crystal Electrodes. *J. Mol. Catal. A Chem.* **2003**, *199*, 39–47.

(3) Rhimi, B.; Zhou, M.; Yan, Z.; Cai, X.; Jiang, Z. Cu-Based Materials for Enhanced C2+ Product Selectivity in Photo-/Electro-Catalytic CO_2 Reduction: Challenges and Prospects. *Nano-Micro Lett.* **2024**, *16*, 64.

(4) Schouten, K. J. P.; Qin, Z.; Pérez Gallent, E.; Koper, M. T. M. Two Pathways for the Formation of Ethylene in CO Reduction on Single-Crystal Copper Electrodes. *J. Am. Chem. Soc.* **2012**, *134*, 9864–9867.

(5) Hussain, J.; Jónsson, H.; Skúlason, E. Calculations of Product Selectivity in Electrochemical CO_2 Reduction. *ACS Catal.* **2018**, *8*, 5240–5249.

(6) Bagger, A.; Ju, W.; Varela, A. S.; Strasser, P.; Rossmeisl, J. Electrochemical CO_2 Reduction: Classifying Cu Facets. *ACS Catal.* **2019**, *9*, 7894–7899.

(7) Van den Bossche, M.; Rose-Petruck, C.; Jónsson, H. Competing HCOOH and CO Pathways in CO_2 Electroreduction at Copper Electrodes: Calculations of Voltage Dependent Activation Energy. *J. Phys. Chem. C* **2021**, *125*, 13802–13808.

(8) Bernal, M.; Bagger, A.; Scholten, F.; Sinev, I.; Bergmann, A.; Ahmadi, M.; Rossmeisl, J.; Cuenya, B. CO_2 Electroreduction on Copper-Cobalt Nanoparticles: Size and Composition Effect. *Nano Energy* **2018**, *53*, 27–36.

(9) Yan, Y.; Zhao, Z.; Zhao, J.; Tang, W.; Huang, W.; Lee, J.-M. Atomic-Thin Hexagonal CuCo Nanocrystals with d-band Tuning for CO_2 Reduction. *J. Mater. Chem. A* **2021**, *9*, 7496–7502.

(10) Xu, C.; Vasileff, A.; Jin, B.; Wang, D.; Xu, H.; Zheng, Y.; Qiao, S. Graphene-Encapsulated Nickel-Copper Bimetallic Nanoparticle Catalysts for Electrochemical Reduction of CO_2 to CO. *ChemComm* **2020**, *56*, 11275–11278.

Downloaded from pubs.acs.org/jpclcd/article-pdf/15/21/5654/3368947/jz4c00899.pdf by NATL AND UNIV LBRY OF ICELAND user on 07 September 2026

(11) Hannagan, R. T.; Giannakakis, G.; Flytzani-Stephanopoulos, M.; Sykes, E. C. H. Single-Atom Alloy Catalysis. *Chem. Rev.* **2020**, *120*, 12044−12088.
(12) Réocreux, R.; Stamatakis, M. One Decade of Computational Studies on Single-Atom Alloys: Is in Silico Design within Reach? *Acc. Chem. Res.* **2022**, *55*, 87−97.
(13) Schumann, J.; Stamatakis, M.; Michaelides, A.; Réocreux, R. Ten-Electron Count Rule for the Binding of Adsorbates on Single-Atom Alloy Catalysts. *Nat. Chem.* **2024**, 1−6.
(14) Liu, T.; Song, G.; Liu, X.; Chen, Z.; Shen, Y.; Wang, Q.; Peng, Z.; Wang, G. Insights into the Mechanism in Electrochemical CO_2 Reduction over Single-Atom Copper Alloy Catalysts: A DFT Study. *iScience* **2023**, *26*, No. 107953.
(15) Salomone, M.; Fiorentin, M. R.; Risplendi, F.; Raffone, F.; Sommer, T.; García-Melchor, M.; Cicero, G. Efficient Mapping of CO Adsorption on $Cu_{(1-x)}M_x$ Bimetallic Alloys via Machine Learning. *ChemRxiv* **2023**, DOI: 10.26434/chemrxiv-2023-kc7s7. (accessed 2024-04-29)
(16) Eren, B.; Torres, D.; Karslıoğlu, O.; Liu, Z.; Wu, C. H.; Stacchiola, D.; Bluhm, H.; Somorjai, G. A.; Salmeron, M. Structure of Copper−Cobalt Surface Alloys in Equilibrium with Carbon Monoxide Gas. *J. Am. Chem. Soc.* **2018**, *140*, 6575−6581.
(17) Wang, Y.; Schumann, J.; Happel, E. E.; Çınar, V.; Sykes, E. C. H.; Stamatakis, M.; Michaelides, A.; Hannagan, R. T. Observation and Characterization of Dicarbonyls on a RhCu Single-Atom Alloy. *J. Phys. Chem. Lett.* **2022**, *13*, 6316−6322.
(18) Kohn, W. Nobel Lecture: Electronic Structure of Matter—Wave Functions and Density Functionals. *RMP* **1999**, *71*, 1253−1266.
(19) Blöchl, P. E. Projector Augmented-Wave Method. *Phys. Rev. B* **1994**, *50*, 17953−17979.
(20) Hammer, B.; Hansen, L. B.; Nørskov, J. K. Improved Adsorption Energetics within Density-Functional Theory Using Revised Perdew-Burke-Ernzerhof Functionals. *Phys. Rev. B* **1999**, *59*, 7413−7421.
(21) Vollmer, S.; Witte, G.; Wöll, C. Determination of Site Specific Adsorption Energies of CO on Copper. *Catal. Lett.* **2001**, *77*, 97−101.
(22) Kresse, G.; Furthmüller, J. Efficient Iterative Schemes for Ab Initio Total-Energy Calculations Using a Plane-Wave Basis Set. *Phys. Rev. B* **1996**, *54*, 11169−11186.
(23) Kresse, G.; Joubert, D. From Ultrasoft Pseudopotentials to the Projector Augmented-Wave Method. *Phys. Rev. B* **1999**, *59*, 1758−1775.
(24) Bader, R. *Atoms in Molecules: A Quantum Theory*; Oxford University Press,: New York, 1990.
(25) Henkelman, G.; Arnaldsson, A.; Jónsson, H. A Fast and Robust Algorithm for Bader Decomposition of Charge Density. *Comput. Mater. Sci.* **2006**, *36*, 354−360.

Downloaded from pubs.acs.org/jpclcd/article-pdf/15/21/5654/3368947/jz4c00899.pdf by NATL AND UNIV LBRY OF ICELAND user on 07 September 2026

https://doi.org/10.1021/acs.jpclett.4c00899
J. Phys. Chem. Lett. 2024, 15, 5654−5658

Publication II

Multiple Adsorption of CO Molecules on Transition Metal Substitutional Impurities in Copper Surfaces

Magnus A. H. Christiansen, Wei Wang, Elvar Ö. Jónsson, Giancarlo Cicero, and Hannes Jónsson

ChemCatChem 17, no. 18 (2025)

Check for updates

ChemCatChem

Research Article
doi.org/10.1002/cctc.202500765

Chemistry Europe
European Chemical Societies Publishing

www.chemcatchem.org

Multiple Adsorption of CO Molecules on Transition Metal Substitutional Impurities in Copper Surfaces

Magnus A. H. Christiansen,*[a] Wei Wang,[b] Elvar Ö. Jónsson,[a] Giancarlo Cicero,[b] and Hannes Jónsson*[c, d]

Copper-based catalysts are of particular interest for electrochemical reduction of CO_2 (CO2RR) as products beyond CO can form. To improve activity and selectivity, several studies have focused on the addition of other elements as substitutional impurities. Although the adsorption of a single CO molecule has often been used as a descriptor for CO2RR activity, our recent calculations using the RPBE functional showed that multiple CO molecules can bind to first-row transition metal impurities. Here, we extend the study to second-row transition metals and also to a functional that explicitly includes dispersion interaction, BEEF-vdW. The binding energy of the first CO molecule on the impurity atom is found to be significantly larger than on the clean Cu(111) and Cu(100) surfaces, but the differential binding energy generally drops as more CO molecules adsorb. The dispersion interaction is found to make a significant contribution to the binding energy, in particular for the last and weakest bound CO molecule, the one that is most likely to participate in CO2RR. In some cases, four CO admolecules can bind more strongly on the impurity atom than on the clean copper surface. The adsorption of CO causes the position of the impurity atom to shift outwards and in some cases, even escape from the surface layer. The C—O stretch frequencies are calculated in order to identify possible experimental signatures of multiple CO adsorption.

1. Introduction

Copper is a promising catalyst for CO_2 electroreduction (CO2RR), as products beyond CO can form such as methane and ethene.[1,2] There, the CO intermediate binds strongly enough on the surface to get further reduced while the coverage of hydrogen remains low because of weak binding to H adatoms, and thereby relatively slow hydrogen evolution reaction. The CO2RR catalytic activity has been characterized by using a two-parameter descriptor involving the binding energy of a CO admolecule on the one hand and the adsorption strength of hydrogen on the other hand, either at high H-coverage[3] or for a single H adatom.[4] Although the two are somewhat correlated, there is a qualitative difference in that the dispersion interaction makes an important contribution to the binding of a CO molecule while it is unimportant for the binding of an H atom. Too weak binding of CO leads to its release, and thereby no further reduction, as on silver surfaces,[5,6] while the presence of H adatoms on the surface can lead to a competing reaction pathway resulting in the release of formate without further reduction.[7] On surfaces where the hydrogen coverage can become high, such as Pt surfaces, only hydrogen is formed under reducing conditions[8,9] because the rate of the hydrogen evolution reaction is significantly higher than the CO2RR rate.[10] The two parameter descriptor of a CO molecule and hydrogen adsorption can, in principle, also be used to predict the efficiency of copper surfaces modified by incorporation of other elements, but additional complications may arise, as it may not be sufficient to consider the binding of only a single CO molecule.[11]

The activity and selectivity of copper as a CO2RR catalyst is, however, not high enough for the process to be cost-effective. Several experimental reports have shown that the addition of another element to a copper surface, such as Co,[12,13] Ni,[14] or Pd,[15–17] can lead to significant improvements. Even a trace amount of these atoms can substantially influence the reaction rate, selectivity, and overpotential required for CO2RR. These copper-based surfaces with small amounts of substitutional impurities belong to a class of catalysts known as single atom alloys (SAAs).[18–24] There, the secondary metal is present in such a low concentration that the atoms are dispersed as substitutional impurities in the surface of the host metal. Typically, the host metal is a less active but more selective material, copper in the present case, while the substituent atoms are of more reactive elements, here transition metals with less occupied d-electron orbitals.

In computational searches for improved CO2RR electrocatalyst materials, the binding energy of an adsorbed CO molecule to the surface is commonly used as a key indicator for the catalytic

[a] M. A. H. Christiansen, E. Ö. Jónsson
Science Institute of the University of Iceland, Reykjavík107, Iceland
E-mail: mah107@hi.is

[b] W. Wang, G. Cicero
Department of Applied Science and Technology, Politecnico di Torino, Torino 10129, Italy

[c] H. Jónsson
Faculty of Physical Sciences, University of Iceland, Reykjavík107, Iceland
E-mail: hj@hi.is

[d] H. Jónsson
On leave at Oxford University, Oxford, UK

Magnus A. H. Christiansen and Wei Wang contributed equally to this work.

Supporting information for this article is available on the WWW under https://doi.org/10.1002/cctc.202500765

© 2025 Wiley-VCH GmbH

18673899, 2025, 18, Downloaded from https://chemistry-europe.onlinelibrary.wiley.com/doi/10.1002/cctc.202500765 by Brown University Library, Wiley Online Library on [19/09/2025]. See the Terms and Conditions (https://onlinelibrary.wiley.com/terms-and-conditions) on Wiley Online Library for rules of use; OA articles are governed by the applicable Creative Commons License

activity. According to the Sabatier principle,[25] a good catalyst should strike a balance between having strong enough binding energy of intermediates to the surface and weak enough binding energy of the final product for facile release from the surface. The binding energy of a CO molecule is taken to be a reliable descriptor for the various intermediates involving bonding to a C atom to the surface, such as in COOH, COH, CHO, and CH_3. Consequently, the search for improved CO2RR catalysts has focused on optimizing the binding energy of a single CO molecule on the catalyst surface.[26,27] However, recent density functional theory (DFT) calculations on CO binding to first-row transition metal (TM) impurities in Cu(111) and Cu(100) surfaces, show that up to four CO molecules can bind to the same TM surface atom in some cases.[11] The first CO molecule binds so strongly that it is not likely to participate in CO2RR. Instead, it is either the second, third, or possibly the fourth CO molecule that binds weakly enough to be reactive. It is, therefore, essential to identify the CO molecule that binds weakest to the substituent atom, while the binding energy is still comparable to that which other sites on the surface offer.

Here, we present results of calculations on the binding of multiple CO molecules onto substitutional atoms from the second row of TMs in Cu(100) and Cu(111) surfaces, as well as a re-evaluation of the binding to first-row TMs, using a density functional that has been shown to be more accurate for CO binding to copper surfaces and includes explicitly the dispersion interaction. Although the densely packed (111) facet corresponds to the lowest surface energy, the second lowest energy facet, the (100) surface, is especially interesting as it has been shown to produce more C_2 product, namely, ethylene, than C_1 products, such as methane.[28] For all the first and second row TM, except for Zn, Ag, and Cd, the substitutional atom adsorbs more than one CO molecule more strongly than on the pure copper surface, and in some cases up to four CO molecules. The binding of multiple CO molecules to the substitutional atom significantly affects its position, in some cases displacing it by over 0.8 Å outward from the surface plane and even, for Mn, Fe, and Co, bringing it out of the lattice site. Various properties, such as magnetic moment, are evaluated, and the vibrational frequencies of the adsorbed CO molecules are calculated to assess the possibility of detecting the multiple CO bindings experimentally by Raman or infrared (IR) spectroscopy.

2. Methods

The spin-polarized density functional theory (DFT) calculations are carried out using the Bayesian error estimation functional, BEEF-vdW.[29] It includes a nonlocal correlation term representing fluctuating dipoles (see Equation 3 of ref. [29]), which is referred to as dispersion interaction. It has been shown to give an estimate of CO adsorption energy on various surfaces that is in good agreement with experiments.[30] The calculations are carried out for a four-layer slab with a 4 × 4 surface supercell, using a plane wave representation of the valence electrons with a cutoff energy of 450 eV, while the projector augmented wave (PAW) approach[31] is used to describe the effect of the inner electrons. A 5 × 5 × 1 Monkhorst–Pack k-point grid is used.

The minimum energy configuration of the atoms is obtained using a conjugate gradient optimizer until all atomic forces are smaller than 0.01 eV $Å^{-1}$, and the electronic structure is optimized to self-consistency to a tolerance of 10^{-6} eV. The relaxed copper crystal has a lattice parameter of 3.6551 Å, 1.39% larger than the experimental value. The Vienna ab initio simulation package (VASP)[32,33] is used to carry out the calculations.[34]

The differential binding energy, i.e., the energy required to remove the *n*-thCO molecule from the surface and bring it into the vacuum, is calculated as

$$E_{\text{b-n}^{\text{th}}\,\text{CO/M@Cu}} = E_{\text{CO}} + E_{(\text{CO})_{n-1}/\text{M@Cu}} - E_{(\text{CO})_n/\text{M@Cu}},$$

where M is the substitutional atom and M@Cu is the copper surface with a substitutional atom. E_{CO} is the energy of the isolated CO molecule, while $E_{(CO)_n/M@Cu}$ is the energy of the system consisting of the M@Cu surface with *n* CO molecules bound to the substituent atom. The number of unpaired electrons, i.e., magnetization, is evaluated from the output of the spin-polarized DFT calculations, calculated from the difference in integrated spin-up and spin-down electron density.

Only CO adsorption is considered here and the presence of adsorbed hydrogen atoms not considered. The hydrogen evolution reaction is a competing reaction and the coverage of H adatoms is likely to be significant under CO2RR conditions. The H adatoms compete with CO molecules for surface sites. This would add significant complexity to the calculations, as multiple configurations of H and CO on the surface should be evaluated to determine the minimum energy arrangement for different levels of hydrogen coverage and varying numbers of adsorbed CO molecules. This will be addressed in future studies.

The data on which the results presented in this article are based and the input parameters for the calculations are available at Zenodo.[35]

3. Results and Discussion

3.1. CO Adsorption on Cu(111) and Cu(100)

The Cu(100) surface has three adsorption sites: top, bridge, and hollow site. Calculations with the BEEF-vdW functional give the strongest CO binding on the top site, followed by the bridge site, and then the hollow site provides the weakest binding. The top site binding energy is estimated to be 0.61 eV based on the minimum energy configuration, and this gets reduced to 0.57 eV if the zero-point energy is subtracted. This is in good agreement with the experimentally determined value of 0.53 eV.[36,37] The ordering of the binding sites is also in agreement with both the interpretation of the experimental measurements and the results of higher-level theoretical calculations based on the random phase approximation.[38] The commonly used RPBE functional

© 2025 Wiley-VCH GmbH

18673898, 2025, 18, Downloaded from https://chemistry-europe.onlinelibrary.wiley.com/doi/10.1002/cctc.202500765 by Brown University Library, Wiley Online Library on [19/09/2025]. See the Terms and Conditions (https://onlinelibrary.wiley.com/terms-and-conditions) on Wiley Online Library for rules of use; OA articles are governed by the applicable Creative Commons License

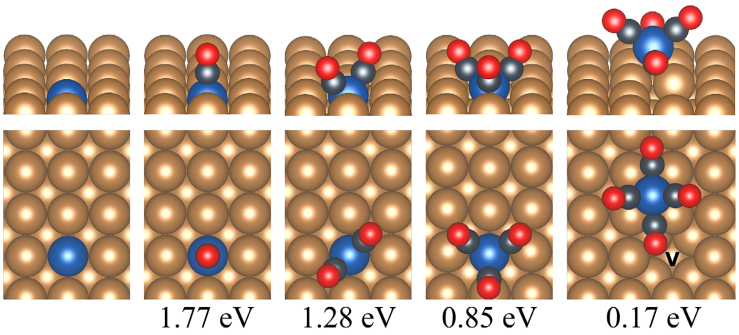

Figure 1. Minimum energy atomic structure of the Cu(100) surface with a Co substitutional atom (blue) and up to four CO molecules (black: C atoms; red: O atoms). After the fourth CO molecule is adsorbed, the Co atom moves out of the surface layer and a vacancy (indicated by V) is formed. The differential binding energy is written below their respective structures. This is a composite figure, the calculations are carried out for just one substitutional atom in the surface.

does not give the same ordering, as it predicts the hollow site to provide the strongest binding to the CO molecule.

The Cu(111) surface has four distinct adsorption sites: top, bridge, hollow FCC, and hollow HCP sites. The BEEF-vdW calculations give the strongest CO binding at the hollow FCC site, followed by the hollow HCP site, then the top site, and finally the bridge site. The binding energy at the hollow site is 0.53 eV based on the minimum energy configuration and 0.49 eV if the zero-point energy is subtracted, in close agreement with the experimental estimate of 0.49 eV.[36]

3.2. CO Binding on 3d TM Impurity

The introduction of a metal atom from the first row of the transition metals to the left of copper into the Cu(111) and Cu(100) surfaces creates a strong adsorption site for CO molecules. An example is shown in Figure 1, where a Co atom has replaced one of the Cu atoms in the Cu(100) surface. The minimum energy structures of up to four CO adsorbed to the Co atom are shown. As more CO molecules bind to the Co atom, its position moves outwards from the plane of the surface atoms. When four CO molecules are adsorbed, the Co atom moves out of the surface site, and a vacancy is formed in the surface layer. The differential binding energy of the fourth CO molecule is, however, smaller than the binding energy to the clean Cu(100) surfaces, so this displacement of the $Co(CO)_4$ complex will only occur at high CO coverage.

The calculated differential CO binding energy on a 3d TM substitutional atom (Sc, Ti, V, Cr, Mn, Fe, Co, Ni) in Cu(100) and Cu(111) surfaces is illustrated in Figure 2. The binding energy of CO on the clean copper surfaces is indicated for reference. The results obtained here using the BEEF-vdW functional are similar to the previously reported results obtained with the RPBE functional,[11] although it does not include the dispersion interaction. Since the RPBE functional is fitted to give quite good binding energy for molecules on surfaces even without explicit inclusion of dispersion interaction, it is implicitly taking the net effect of the dispersion interaction into account in some way.

Three distinct trends in the differential binding energy can be seen from Figure 2. The expected trend of decreasing bond strength with the number of CO molecules is seen for Fe, Co, and Ni substitutional atoms. As a general rule, an atom makes weaker bonds the more bonds it forms. For Fe and Co, the differential binding energy is stronger for the first, second, and third adsorbed CO molecules compared to the pure Cu surface on both the (100) and (111) facets. A metastable minimum energy structure is obtained for the fourth adsorbed CO molecule, although the differential binding energy at that point is weaker than for adsorption on the pure copper surface, i.e., far from the substitutional atom. For Ni, the differential binding energy is stronger for the first and second adsorbed CO molecules compared to the pure surface of Cu(100) and Cu(111), while the third and fourth COs binds stronger to the pure copper surfaces.

The opposite trend, namely, increasing differential binding energy, is obtained for the first three CO molecules binding to V, Cr, and Mn substitutional atoms. This trend stops for the fourth CO molecule as the differential binding energy drops abruptly. On the Cu(100) surface, the fourth CO binds slightly weaker to the Cr and Mn than to the pure copper surface, by 0.04 and 0.08 eV, respectively. For the Cu(111) surface, the fourth CO binds significantly weaker to the Cr and Mn compared to the pure copper surface, by 0.28 and 0.51 eV, respectively.

The third trend is roughly constant differential binding energy for the first three CO molecules on Ti and all four on Sc. When placed in the Cu(100) surface, the differential binding energy of the fourth CO is still significantly stronger for the Sc and Ti compared to the pure copper surface. In the Cu(111) surface, the differential binding energy for the fourth CO is almost identical (ca. 0.01 eV difference) to the CO binding energy on Cu(111).

For the V substitutional atom, the trend is somewhat different depending on which copper facet it is placed in. For the Cu(100) surface, binding to a V substitutional atom shows a sim-

© 2025 Wiley-VCH GmbH

18673899, 2025, 18, Downloaded from https://chemistry-europe.onlinelibrary.wiley.com/doi/10.1002/cctc.202500765 by Brown University Library, Wiley Online Library on [19/09/2025]. See the Terms and Conditions (https://onlinelibrary.wiley.com/terms-and-conditions) on Wiley Online Library for rules of use; OA articles are governed by the applicable Creative Commons License

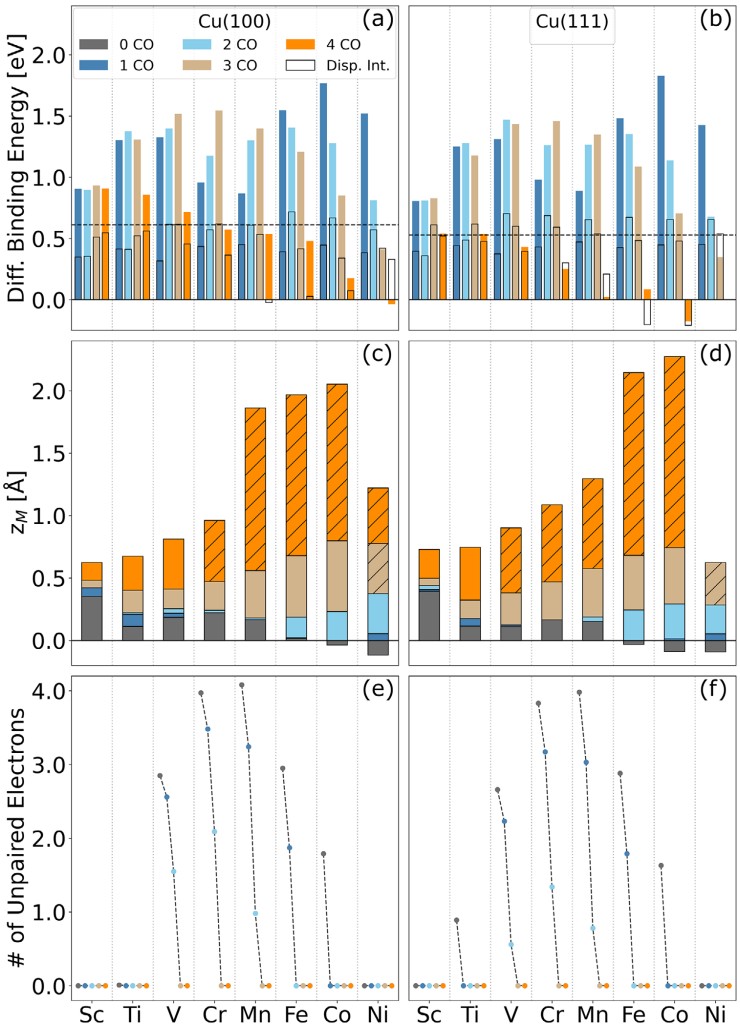

Figure 2. Left panel shows calculated results for Cu(100) and the right panel for Cu(111). (a, b) Differential binding energy, $E_{b\text{-}n^{th}\,CO/M@Cu}$, for the first, second, third, and fourth CO molecules bound to a 3d transition metal substitutional atom. The open bars indicate the contribution from the dispersion interaction as estimated by the BEEF-vdW functional. The black dashed lines indicate the binding energy of a single CO molecule on the clean copper surface. (c, d) *z*-Coordinate of the M atom with respect to the copper surface, which lies in the *xy*-plane at $z = 0$, when up to four CO molecules adsorb to the M atom. The hatched bars indicate structures that are higher in energy than a structure where one of the CO molecules is placed on the pure copper surface, i.e., far from the M atom. (e, f) Number of unpaired electrons of the substitutional M atom. The binding of CO increases the energy splitting between the d-orbitals and reduces the number of unpaired electrons.

ilar trend as for Cr and Mn atoms, i.e., increased differential binding energy for the first three adsorbed CO molecules and then a decrease for the fourth CO, but still stronger binding than to the pure copper surface. When placed in the Cu(111) surface, the differential binding energy decreases slightly for the third CO. The fourth CO binds weaker to the V atom than on the clean Cu(111) surface.

Figure 2 also shows how the position of the substitutional metal atom relative to the copper surface plane changes as the CO molecules are adsorbed. Sc, the largest of the first-row transition metal atoms, initially sits 0.35 and 0.39 Å above the Cu(100) and Cu(111) surface planes, respectively, in the absence of CO adsorption. As the CO molecules adsorb, the Sc atom is further displaced outward by 0.2–0.3 Å. The smallest of these

© 2025 Wiley-VCH GmbH

18673898, 2025, 18, Downloaded from https://chemistry-europe.onlinelibrary.wiley.com/doi/10.1002/cctc.202500765 by Brown University Library, Wiley Online Library on [19/09/2025]. See the Terms and Conditions (https://onlinelibrary.wiley.com/terms-and-conditions) on Wiley Online Library for rules of use; OA articles are governed by the applicable Creative Commons License

atoms, Ni, initially sits ~0.1 Å below the Cu(100) and Cu(111) surface planes. Co exhibits similar behavior, sitting 0.04 and 0.09 Å below the Cu(100) and Cu(111) surface planes, respectively. The V atom exhibits the largest outward displacement, 0.81 Å above the Cu(100) surface with four adsorbed CO molecules. On the Cu(111) surface, the Ti atom shows the largest displacement, 0.75 Å above the surface plane with four CO molecules adsorbed.

A more drastic displacement occurs when four CO are bound to Mn, Fe, and Co substitutional atoms in the Cu(100) surface, as they move from the lattice site and relocate onto the copper surface, thereby creating a vacancy in the surface layer. The Mn, Fe, and Co atoms are positioned 1.86, 1.97, and 2.05 Å above the Cu(100) surface plane, respectively. On the Cu(111) surface, only the Fe and Co substitutional atoms move outward onto the surface, positioned at 2.15 and 2.27 Å above the Cu(111) surface plane, respectively. However, the adsorption of the fourth CO molecule on these atoms is less energetically favorable compared to CO adsorption on the pure Cu(100) surface, as shown in Figure 2a. Therefore, these structures are only likely to form for high CO coverage.

The open bars in Figure 2a,b indicate the contribution from the dispersion interaction to the differential binding energy as obtained from the BEEF-vdW functional. As seen with the Sc substituent atom, which undergoes only small change in its position with respect to the surface plane as CO molecules adsorb, the contribution of the dispersion interaction to the differential binding energy tends to increase with the number of adsorbed CO molecules. By the time the fourth CO molecule adsorbs, the majority of the binding energy arises from dispersion interaction. An exception to this trend is observed for the Mn, Fe, and Co substituent atoms, where the interaction between the CO molecules and the substituent atoms is so strong that the atoms are pulled from their lattice sites onto the copper surface. As a result, the distance between the copper surface and the metal–carbonyl complex increases significantly, leading to a decrease in the dispersion interaction. In these cases, the differential dispersion interaction contribution even becomes negative.

The change in the differential binding energy of the CO molecules can be correlated with the number of unpaired d-electrons. Figure 2e,f shows the calculated magnetic moments of the substitutional transition metals atoms. For Sc and Ni, the initial magnetic moment is zero, while Ti and Co begin with a small magnetic moment that disappears upon adsorption of the first CO molecule. For the other first-row transition metals, the magnetic moment decreases monotonically in a stepwise manner as more CO molecules adsorb. This results from an increased energy difference between the different d-orbitals of the substitutional atoms as more of the CO molecules adsorb, and thereby more pairing of the d-electrons. This helps explain the unusual increase in differential binding energy calculated for Cr and Mn as the second and third CO molecules are added.

3.3. CO Binding to 4d TM Impurities

Figure 3 shows the calculated results for substitutional atoms from the second row of transition metals (Y, Zr, Nb, Mo, Tc, Ru, Rh, Pd). Two trends are observed in the differential binding energy. For Tc, Ru, Rh, and Pd, it decreases as more CO molecules adsorb. In contrast, for Y, Zr, and Nb, the differential binding energy remains relatively constant until it decreases upon adsorption of the fourth CO molecule. A trend of increasing differential binding energy, as obtained for some of the 3d TM substitutional atoms, is not found here. The first CO molecule is bound most strongly to a Ru atom, the second CO molecule binds most strongly to the Mo atom, the third CO molecule adsorbs most strongly to the Nb and Mo substituent atoms, while the fourth CO molecule is most strongly bound to the Zr substitutional atom.

The Mo, Tc, and Ru atoms can adsorb up to three CO molecules with a differential binding energy stronger than that of CO adsorption on pure copper surfaces, while Rh adsorbs up to two CO molecules. Pd adsorbs two CO molecules when placed

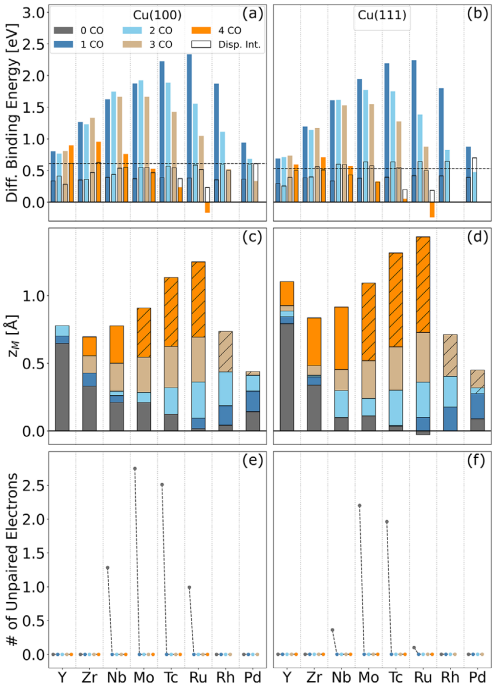

Figure 3. Left panel shows calculated results for Cu(100) and the right panel for Cu(111). (a, b): Differential binding energy, $E_{b\text{-}n^{th}\ CO/M@Cu}$, for first and up to fourth CO molecule bound to a 4d transition metal substitutional atom. The black dashed lines indicate the binding energy of a single CO molecule on the clean copper surface. The open bar (black outlines) indicates the contribution of the dispersion interaction to the differential binding energy. (c, d): *z*-Coordinate of the substitutional atom with respect to the copper surface plane when up to four CO molecules bind to it. The hatched bars indicate structures that are higher in energy than a structure where one of the CO molecules is placed on the pure copper surface, i.e., far from the M atom. (e, f): Number of unpaired electrons of the substitutional M atom. The binding of CO increases the energy splitting between the d-orbitals and reduces the number of unpaired electrons.

© 2025 Wiley-VCH GmbH

18673898, 2025, 18, Downloaded from https://chemistry-europe.onlinelibrary.wiley.com/doi/10.1002/cctc.202500765 by Brown University Library, Wiley Online Library on [19/09/2025]. See the Terms and Conditions (https://onlinelibrary.wiley.com/terms-and-conditions) on Wiley Online Library for rules of use; OA articles are governed by the applicable Creative Commons License

in the Cu(100) surface and one when placed in the Cu(111) surface more strongly than the clean copper surface. Y, Zr, and Nb can adsorb up to four CO molecules with a differential binding energy that exceeds that of CO adsorption on the pure copper surfaces. Among the 4d TMs on the Cu(100) surface, Mo, Rh, and Pd show the most promise for enhanced CO2RR. The differential binding energy for the fourth CO bound to Mo and for the third CO bound to Rh in the Cu(100) surface are both lower by ca. 0.08 eV, compared to the CO binding energy on clean Cu(100). The second CO binds to Pd atom in the Cu(100) surface with a differential binding energy 0.07 eV stronger than the binding energy of CO on the Cu(100) surface, so it is also likely to be able to participate in CO2RR.

Figure 3c,d shows the position of the 4d TM substitutional atoms with respect to the plane of the copper surface atoms. The atom with the largest radius, Y, sits above the surface plane by 0.6 and 0.8 Å for Cu(100) and Cu(111), respectively. As the atomic radius gets reduced going to the right along the second row of TM, the substitutional atom sits closer to the surface. The Ru atom is nearly in the surface plane of Cu(100) while it is slightly below the surface when placed in the Cu(111) surface. Compared to their first-row counterparts, significant differences in the positions are found only for Y, Zr, and Pd. For Nb, Mo, Tc, Ru, and Rh, the difference compared to their first-row counterparts is less than 0.1 Å.

The binding of CO molecules to the Y substitutional atom does not change much its location over the surface plane. When placed in the Cu(100) surface, Y is displaced by up to 0.13 Å, with no significant changes after the first two CO molecules adsorb. On the Cu(111) surface, Y is displaced outwards by 0.31 Å with four adsorbed CO molecules. For Mo, Tc, and Ru, which are smaller than Y, the substitutional atom is displaced slightly in the absence of CO, while the adsorption of the fourth CO molecule can cause a significant outward displacement of over 1 Å. On both the Cu(100) and Cu(111) surfaces, Nb and Ru exhibit the largest displacements as they bind to CO molecules. With three CO molecules adsorbed, Ru is displaced by an additional 0.67 Å on the Cu(100) surface and 0.76 Å on the Cu(111) surface. In the case of Nb bound to four CO molecules, the outward displacement is 0.57 Å when placed in the Cu(100) and by 0.82 Å when placed in the Cu(111) surface.

None of the 4d TM substitutional atoms are found to move onto the copper surface to form an adsorbed carbonyl complex and create a vacancy in the surface layer as found for the Mn, Fe, and Co substitutional atoms when a fourth CO is adsorbed. This indicates that 4d TM substitutional atoms might be more stable as SAA catalysts compared to their 3d TM counterparts.

The number of unpaired electrons of the 4d TM substitutional atoms is smaller than for corresponding 3d TMs, as shown in Figure 3e,f. For Nb, Mo, Tc, and Ru, the magnetic moment drops to zero after adsorbing just a single CO molecule, in contrast to the stepwise decrease observed for the 3d TMs. As can be seen from the larger differential binding energy of the first CO bound to a 4d TM substitutional atom as compared to the corresponding 3d TM atom, the TM–CO interaction is stronger, and this leads to a large energy difference between the different d orbitals and thereby an increased tendency for pairing of the electrons.

Table 1. CO stretching frequencies (cm^{-1}) for CO molecules bound to a substitutional atom, M, in the Cu(100) surface, as well as an isolated CO molecule and CO adsorbed on the pure Cu(100) surface.

M@Cu(100)	Configuration	Frequency (cm^{-1})	Reference
–	CO (gas)	2127	2143 (exp)[a]
Cu	CO(T)	2008	2082-2112 (exp), 2011 (calc)[b]
	CO(B)	1877	1872 (calc)[c]
	CO(H)	1696	
Rh	1 CO	1955	1978 (exp), 1934 (calc)[d]
	2 CO	1896, 1864	1926 (exp), 1891 (calc)[d]
	3 CO	1897, 1862, 1860	
Pd	1 CO	2004	2032 (exp, low exposure)[e]
	2 CO	1910, 1882	1887 (exp, high exposure)[e]
	3 CO	1928, 1899, 1728	1887 (exp, high exposure)[e]
V	1 CO	1964	
	2 CO	1861, 1831	
	3 CO	1852, 1821, 1788	
	4 CO	1862, 1816, 1816, 1812	
Co	1 CO	1929	
	2 CO	1846, 1819	
	3 CO	1891, 1852, 1847	
	4 CO	2017, 1982, 1853, 1824	

[a] Experimental result from Huber et al.[39]
[b] Experimental and calculated results from Roiaz et al.[40]
[c] Calculated result from Zhan et al.[41]
[d] Experimental and calculated results from Wang et al.[42]
[e] Experimental results on CuPd alloy with 9% Pd from Rao et al.[43]

3.4. CO Stretch Vibrational Frequency

The C—O vibrational frequency has been calculated within the harmonic approximation for some of the systems in order to identify possible experimental signatures of multiple CO adsorption on substitutional TM atoms. The results are shown in Table 1 along with calculated results for gas phase CO and CO adsorbed on Cu(100). Some experimental data and previous vibrational calculations are available for some of the systems and are listed in the table for comparison. Although the calculated frequency differs from the experimental results for gas phase CO and CO adsorbed on Cu(100), possibly because of anharmonic contributions as well as shortcomings of the functional approximation, the trends for different binding sites agree well with experiments.[40]

The CO stretch frequency decreases upon adsorption on the Cu(100) surface due to back-donation from the metal to the π^* orbital of the CO molecule, thereby weakening the C-O bond and lowering its stretch frequency.[44,45] The stronger this back-donation interaction is, the lower the CO stretching frequency becomes. A Rh substitutional atom in Cu(100) surface has been shown to adsorb two CO molecules, both from experiments

© 2025 Wiley-VCH GmbH

18673898, 2025, 18, Downloaded from https://chemistry-europe.onlinelibrary.wiley.com/doi/10.1002/cctc.202500765 by Brown University Library, Wiley Online Library on [19/09/2025]. See the Terms and Conditions (https://onlinelibrary.wiley.com/terms-and-conditions) on Wiley Online Library for rules of use; OA articles are governed by the applicable Creative Commons License

and DFT calculations. The monocarbonyl and symmetric dicarbonyl stretches appear at 1978 and 1926 cm^{-1} with a 52 cm^{-1} interval according to experiments, consistent with the calculated results as shown in Table 1.[42] Our results give 1955 and 1896 cm^{-1} with a difference of 59 cm^{-1}, in good agreement with the experimental results.

For a CuPd alloy, experimental measurements[43] found CO stretching frequencies at 2032 cm^{-1} at low CO exposure and 1887 cm^{-1} at high CO exposure, which is close to our calculations of 2004 cm^{-1} for one CO adsorption and ca. 1920 cm^{-1} for two and three CO adsorptions, indicating that the Pd atoms on the alloy surface were bound to two CO molecules in the experimental measurements. The difference in calculated stretch frequencies for two and three CO molecules adsorbed on substitutional atoms is small, so it may be hard to distinguish these two configurations by vibration spectroscopy.

For a V substitutional atom, which can adsorb up to four CO molecules more strongly than the pure Cu(100) surface, the difference between monocarbonyl and dicarbonyl stretches is over 100 cm^{-1}, and should be observable experimentally. The symmetric CO stretches for multiple CO adsorption are, however, close, and there is only a slight red shift from two to three CO molecules and a blue shift from three to four, consistent with the changes in calculated differential binding energy. The asymmetric CO stretch of three CO molecules on the V atom at 1788 cm^{-1} may offer a measurable signature.

On a Co substitutional atom, the calculated results show a significant red shift from one to two adsorbed CO molecules, followed by a slight blue shift with further CO adsorption. This is a different trend from the assignments made in experimental studies[46] of Co deposited on the Cu(110) surface, possibly due to clustering of the Co atoms and/or the broad infrared absorption band.

4. Conclusions

The results presented here from calculations of binding of up to four CO molecule on 3d and 4d TM substitutional atoms in Cu(100) and Cu(111) surfaces using the BEEF-vdW functional highlight the importance of multiple CO adsorption and the importance of the dispersion interaction, especially for the last and weakest bound CO molecule, which is expected to be most important for CO2RR. The differential binding energy decreases as more CO molecules adsorb for most 3d and 4d TM substituent atoms, but binding to Cr and Mn atoms shows the opposite trend, which can be attributed to a change in the number of unpaired d-electrons due to the ligand effect. When Mn, Fe, and Co substitutional atoms bind four CO molecules, they leave the lattice site and form a carbonyl complex on the copper surface indicating a possible degradation mechanism of SAA catalysts. Calculated CO stretch frequencies show that the adsorption of multiple CO molecules could be experimentally detectable with vibrational spectroscopy.

The CO molecules that bind to a substitutional atom with similar strength as CO adsorption to the pure copper surface are most likely to be active reactants in CO2RR. For the Cu(100) surface, the V, Cr, Mn, Nb, and Mo substitutional atoms bind the fourth CO molecule with a differential binding energy close to that of the pure copper surface, while the third CO binds with similar strength to a Rh atom, and the second CO on a Pd atom. For the Cu(111) surface, the Sc, Ti, Y, Zr, and Nb substitutional atoms bind the fourth CO with a differential binding energy close to that of the pristine Cu(111) surface. It is unlikely that two CO molecules adsorbed to the same substituent will dimerize, since this would require overcoming the binding energy of both the last and the second-to-last CO (which can be greater than 1.5 eV). However, if the binding energy of the last adsorbed CO is weak enough, it could undergo C—C coupling with a second CO adsorbed on a neighboring site.

Although we have focused here entirely on the reduction of CO, it could also be interesting to study how substitutional atoms in copper could enhance the CO_2-to-CO conversion. Also, here we have focused entirely on a single substitutional atom in a copper surface, while there are some indications that some substitutional atoms tend to agglomerate into dimers or larger clusters, depending on concentration.[46,47]

Our results show that multiple adsorption of CO molecules on substitutional TM atoms can play a crucial role in determining the activity and stability of copper based electrocatalysts. More generally, similar multiple reactant adsorption could play a role on various SAA catalysts.

Acknowledgments

This work was funded by the Icelandic Research Fund (grant no. 207283-053) and the EU's Horizon 2021 programme under the Marie Skłodowska-Curie Doctoral Networks (MSCA-DN) grant agreement No 101072830 (ECOMATES). H.J. acknowledges support from the Leverhulme Trust (no. VP1-2024-007) and helpful discussions with Prof. Michail Stamatakis.

Views and opinions expressed are those of the authors and do not necessarily reflect the official policy or position of the European Union or the Granting Authority, and neither can be held responsible for them.

Conflict of Interests

The authors declare no conflict of interest.

Data Availability Statement

The data that support the findings of this study are available in the supplementary material of this article and in Ref. [35].

Keywords: CORR · Cu(100) · Cu(111) · Geminal multicarbonyl · Single-atom alloys · Substitutional impurities

© 2025 Wiley-VCH GmbH

18673898, 2025, 18, Downloaded from https://chemistry-europe.onlinelibrary.wiley.com/doi/10.1002/cctc.202500765 by Brown University Library, Wiley Online Library on [19/09/2025]. See the Terms and Conditions (https://onlinelibrary.wiley.com/terms-and-conditions) on Wiley Online Library for rules of use; OA articles are governed by the applicable Creative Commons License

References

[1] Y. Hori, I. Takahashi, O. Koga, N. Hoshi, *J. Phys. Chem. B* **2002**, *106*, 15–17.
[2] Y. Hori, I. Takahashi, O. Koga, N. Hoshi, *J. Mol. Catal. A Chem.* **2003**, *199*, 39–47.
[3] J. Husssain, H. Jónsson, E. Skúlason, *ACS Catal.* **2018**, *8*, 5240–5249.
[4] A. Bagger, W. Ju, A. S. Varela, P. Strasser, J. Rossmeisl, *ACS Catal.* **2019**, *9*, 7894–7899.
[5] N. Hoshi, M. Kato, Y. Hori, *J. Electroanal. Chem.* **1997**, *440*, 283.
[6] M. Re Fiorentin, F. Risplendi, C. Salvini, J. Zeng, G. Cicero, H. Jónsson, *J. Phys. Chem. Lett.* **2024**, *15*, 11538.
[7] M. Van den Bossche, C. Rose-Petruck, H. Jónsson, *J. Phys. Chem. C* **2021**, *125*, 13802–13808.
[8] Y. Hori, A. Murata, R. Takahashi, *J. Chem. Soc. Faraday Trans.* **1989**, *85*, 2309.
[9] Y. Hori, H. Wakebe, T. Tsukamoto, O. Koga, *Electrochim. Acta.* **1994**, *39*, 1833.
[10] J. Hussain, H. Jónsson, E. Skúlason, *Faraday Discuss.* **2016**, *195*, 619.
[11] M. A. H. Christiansen, A. Peña-Torres, E. Ö. Jónsson, H. Jónsson, *J. Phys. Chem. Lett.* **2024**, *15*, 5654–5658.
[12] M. Bernal, A. Bagger, F. Scholten, I. Sinev, A. Bergmann, M. Ahmadi, J. Rossmeisl, B. Cuenya, *Nano Energy* **2018**, *53*, 27–36.
[13] Y. Yan, Z. Zhao, J. Zhao, W. Tang, W. Huang, J.-M. Lee, *J. Mater. Chem. A* **2021**, *9*, 7496–7502.
[14] C. Xu, A. Vasileff, B. Jin, D. Wang, H. Xu, Y. Zheng, S. Qiao, *ChemComm* **2020**, *56*, 11275–11278.
[15] M. Rahaman, et al., *Green Chem.* **2020**, *22*, 6497.
[16] J. Li, et al., *Nat. Comm.* **2020**, *11*, 3685.
[17] Y. Xie, et al., *Nat. Catal.* **2022**, *5*, 564.
[18] R. T. Hannagan, G. Giannakakis, M. Flytzani-Stephanopoulos, E. C. H. Sykes, *Chem. Rev.* **2020**, *120*, 12044–12088.
[19] X. Cui, W. Li, P. Ryabchuk, K. Junge, M. Beller, *Nat. Catal.* **2018**, *1*, 385–397.
[20] X.-F. Yang, A. Wang, B. Qiao, J. Li, J. Liu, T. Zhang, *Acc. Chem. Res.* **2013**, *46*, 1740–1748.
[21] G. Kyriakou, M. B. Boucher, A. D. Jewell, E. A. Lewis, T. J. Lawton, A. E. Baber, H. L. Tierney, M. Flytzani-Stephanopoulos, E. C. H. Sykes, *Science* **2012**, *335*, 1209–1212.
[22] R. Réocreux, M. Stamatakis, *Acc. Chem. Res.* **2021**, *55*, 87–97.
[23] J. D. Lee, J. B. Miller, A. V. Shneidman, L. Sun, J. F. Weaver, J. Aizenberg, J. Biener, J. A. Boscoboinik, A. C. Foucher, A. I. Frenkel, J. E. S. van der Hoeven, B. Kozinsky, N. Marcella, M. M. Montemore, H. T. Ngan, C. R. O'Connor, C. J. Owen, D. J. Stacchiola, E. A. Stach, R. J. Madix, P. Sautet, C. M. Friend, *Chem. Rev.* **2022**, *122*, 8758–8808.
[24] J. Schumann, M. Stamatakis, A. Michaelides, R. Réocreux, *Nat. Chem.* **2024**, *16*, 749–754.
[25] P. Sabatier, *Ber. Dtsch. Chem. Ges.* **1911**, *44*, 1984–2001.
[26] M. J. Kolb, D. Loffreda, P. Sautet, F. Calle-Vallejo, *J. Catal.* **2021**, *395*, 136–142.
[27] F. Calle-Vallejo, M. T. Koper, *ACS Catal.* **2017**, *7*, 7346–7351.
[28] K. J. P. Schouten, Z. Qin, E. P. Gallent, M. T. M. Koper, *J. Am. Chem. Soc.* **2012**, *134*, 9864–9867.
[29] J. Wellendorff, K. T. Lundgaard, A. Møgelhøj, V. Petzold, D. D. Landis, J. K. Nørskov, T. Bligaard, K. W. Jacobsen, *Phys. Rev. B* **2012**, *85*, 235149.
[30] J. Wellendorff, T. L. Silbaugh, D. Garcia-Pintos, J. K. Nørskov, T. Bligaard, F. Studt, C. T. Campbell, *Surf. Sci.* **2015**, *640*, 36–44.
[31] P. E. Blöchl, *Phys. Rev. B* **1994**, *50*, 17953–17979.
[32] G. Kresse, J. Furthmüller, *Phys. Rev. B* **1996**, *54*, 11169–11186.
[33] G. Kresse, D. Joubert, *Phys. Rev. B* **1999**, *59*, 1758–1775.
[34] W. Kohn, *RMP* **1999**, *71*, 1253–1266.
[35] M. A. H. Christiansen, W. Wang, E. Ö. Jónsson, G. Cicero, H. Jónsson, Dataset for the article "multiple adsorption of CO molecules on transition metal substitutional impurities in copper surfaces", **2025**, https://doi.org/10.5281/zenodo.15648227.
[36] S. Vollmer, G. Witte, C. Wöll, *Catal. Lett.* **2001**, *77*, 97–101.
[37] C. M. Truong, J. Rodriguez, D. Goodman, *Surf. Sci.* **1992**, *271*, L385–L391.
[38] Z. Wei, F. Göltl, P. Sautet, *J. Chem. Theory Comput.* **2021**, *17*, 7862–7872.
[39] K. P. Huber, G. Herzberg, *Molecular Spectra and Molecular Structure: IV. Constants of Diatomic Molecules*, Springer, New York, NY **1979**.
[40] M. Roiaz, L. Falivene, C. Rameshan, L. Cavallo, S. M. Kozlov, G. Rupprechter, *J. Phys. Chem. C* **2019**, *123*, 8112–8121.
[41] C. Zhan, F. Dattila, C. Rettenmaier, A. Herzog, M. Herran, T. Wagner, F. Scholten, A. Bergmann, N. López, B. R. Cuenya, *Nat. Energy.* **2024**, *09*, 1485–1496.
[42] Y. Wang, J. Schumann, E. E. Happel, V. Çınar, E. C. H. Sykes, M. Stamatakis, A. Michaelides, R. T. Hannagan, *J. Phys. Chem. Lett.* **2022**, *13*, 6316–6322.
[43] C. N. R. Rao, P. V. Kamath, K. Prabhakaran, M. S. Hegde, *Can. J. Chem.* **1985**, *63*, 1780–1787.
[44] A. S. Goldman, K. Krogh-Jespersen, *J. Am. Chem. Soc.* **1996**, *118*, 12159–12166.
[45] G. Bistoni, S. Rampino, N. Scafuri, G. Ciancaleoni, D. Zuccaccia, L. Belpassi, F. Tarantelli, *Chem. Sci.* **2016**, *7*, 1174–1184.
[46] B. Eren, D. Torres, O. Karslıoğlu, Z. Liu, C. H. Wu, D. Stacchiola, H. Bluhm, G. A. Somorjai, M. Salmeron, *J. Am. Chem. Soc.* **2018**, *140*, 6575–6581.
[47] Z.-K. Han, D. Sarker, R. Ouyang, A. Mazheika, Y. Gao, S. V. Levchenko, *Nat. Commun.* **2021**, *12*, 1833.

Manuscript received: April 28, 2025
Revised manuscript received: June 20, 2025
Accepted manuscript online: June 25, 2025
Version of record online: July 15, 2025

© 2025 Wiley-VCH GmbH

Publication III

Adsorption of CO Molecules on Stepped Copper Surfaces with and without Transition Metal Impurities

Magnus A. H. Christiansen, Elvar Ö. Jónsson, and Hannes Jónsson

Used with permission; see publisher terms.

Adsorption of CO on Surface Islands of Copper, With and Without Substitutional Atoms of More Reactive Transition Metals

Magnus A. Hilduberg Christiansen[1], Elvar Örn Jónsson[1], and Hannes Jónsson*[1]

[1]Science Institute and Faculty of Physical Sciences, University of Iceland VR-III, 107 Reykjavík, Iceland

*Email: hj@hi.is

Abstract

Copper-based catalysts are important for many chemical reactions, for example the electrochemical reduction of CO to C_2H_4 where the C–C bond formation is a key step. Recent experimental studies have highlighted the importance of surface steps for the catalytic activity and other studies have indicated that substitutional surface atoms of a more reactive transition metal can enhance the selectivity towards such C_2 products. Here, the minimum energy paths of CO migration on Cu islands are calculated and the results show a strong tendency for the admolecules to decorate steps. The probability of finding CO molecules sitting at adjacent sites, even at relatively low coverage, thereby becomes higher and the calculated step formation energy at both Cu(111) and Cu(100) surfaces is reduce to a half. Also, the effect of introducing 3d (Sc–Ni) and 4d (Y–Pd) transition metal substitutional atoms at the steps is studied. Not only does the first CO molecule bind more strongly on such a substitutional step atom than on the clean copper surface, but the second and third CO admolecules can have even stronger differential binding energy in several cases. Depending on the transition metal and facet of copper, up to four CO molecules can adsorb on a single substitutional atom to form a surface carbonyl complex. While the substitutional atoms preferentially sit in terrace sites, or in subsurface sites near but not at steps, the carbonyl complex is in most cases more stable at a step site. Their presence thereby further reduces the step formation energy. This could be part of the reason why the introduction of a small amount of a more reactive transition metal has been found experimentally to increase catalytic activity as well as selectivity towards C_2 products.

Introduction

Copper is an important catalyst for many chemical reactions. It is, for example, the only pure metal that can catalyze electrochemical reduction of CO_2 beyond CO to form hydrocarbons [1, 2]. Remarkably, C–C bond formation can occur during the reaction and ethylene is produced more readily than methane, especially when the crystal is oriented to expose the (100) facet [3]. The catalytic activity and selectivity of copper have been rationalized in terms of two descriptors: the adsorption energy of CO which is sufficiently large for it to be retained on the surface and thereby further reduced, and the adsorption energy of H which is sufficiently small for the competing hydrogen evolution reaction not to dominate [4, 5]. The binding energy of an adsorbed CO molecule has frequently been used as a descriptor for catalytic activity in computational studies [6, 7].

Catalytic activity of solid surfaces can depend strongly on surface morphology, in particular the abundance of undercoordinated sites such as steps. An elegant demonstration of this was provided by the joint experimental and theoretical study of the groups of Chorkendorff and Nørskov where the addition of a small amount of Au on Ru(0001) surfaces, just enough to decorate steps, was shown to eliminate the dissociative adsorption of N_2 molecules, and thereby formation of NH_3. Recently, experiments by Cheng et al. [8] have

demonstrated that pristine Cu(111) and Cu(100) surfaces exhibit little CO_2 reduction activity and instead predominantly catalyze the hydrogen evolution reaction. However, after steps have been induced, ethylene and methane production increases significantly, showing that steps play a key role. Their observation indicates that the interaction of reaction intermediates such as CO with steps on copper surfaces plays an important role in the catalytic activity.

The surface morphology can change in response to CO adsorption. Eren et al. [9] demonstrated that exposure to CO induces the restructuring of Cu(111) into nanoclusters, while Roiaz et al. [10] reported CO-induced roughening and the formation of Cu adatoms and clusters on Cu(100) at elevated CO pressure. Under electrochemical conditions, Amirbeigiarab et al. [11] observed CO-promoted nanocluster formation near the onset of CO_2 reduction, accompanied by persistent changes in the atomic-scale surface structure. More recently, Wei et al. combined experimental measurements and grand-canonical modeling to show that co-adsorbed hydroxyls and CO can act together to promote Cu adatom and nanocluster formation during CO electroreduction [12]. These findings establish a close connection between CO adsorption and copper surface reconstruction, where undercoordinated sites bind reaction intermediates more strongly and the presence of the adsorbate thereby lowers the formation energy of surface defects.

The catalytic properties of copper can also be modified by incorporating atoms of another element. Experimental studies have shown that the addition of a small amount of a more reactive transition metal such as Co [13–15], Ni [16], or Pd [17–19] can influence the activity and selectivity in CO_2 electroreduction. When the added metal remains atomically dispersed within the Cu host, the resulting material is referred to as a single-atom alloy (SAA) [20–26]. The substitutional atom provides a chemically distinct adsorption site and can open new reaction pathways. Its location can be affected by the adsorbate. For example, Simonovis et al. [27] observed CO-induced surface segregation of Pt in a Pt/Cu(111) SAA, demonstrating that adsorption can modify the distribution of a dilute alloy component.

An interesting feature of SAA active sites is their ability to accommodate multiple admolecules. Wang et al. [28] identified dicarbonyl species at Rh atoms in a RhCu(100) SAA using temperature-programmed desorption and reflection absorption infrared spectroscopy measurements supported by density functional theory (DFT) calculations. In our previous DFT studies, we showed that up to four CO molecules can adsorb on 3d (Sc–Ni) and 4d (Y–Pd) substitutional atoms in Cu(111) and Cu(100) surfaces with the strongest differential binding energy in some cases obtained for the second or third CO admolecule [29, 30]. Such an increase in the differential binding energy was found to correlate with a reduction in the magnetic moment of the substitutional atom. Calculations by Berger et al. also show favorable adsorption of two admolecules at the same site for a range of SAAs and types of admolecules, including NO adsorption [31].

However, the adsorption of two or more CO molecules on the same substitutional atom does not lead to C–C bond formation as the CO molecules are bound too strongly, typically by 1 eV or more. As a result, CO molecules bound to a substitutional atom of a more reactive transition metal than Cu are less reactive than CO admolecules on a clean Cu surface where the adsorption energy is around 0.5 eV. The strong binding of CO makes the reaction barrier too high for C–C bond formation to be viable. Calculations by Wang et al. [32], for example, show that a Pd substitutional atom in Cu(100) makes C–C bond formation less favorable than on the clean copper surface under electrochemical conditions. If, however, the intrinsic reaction barrier at the substitutional atom is no higher than on the clean surface, the reactivity can be enhanced since the molecules are brought together into close proximity, as has been demonstrated in kinetic Monte Carlo simulations [31]. The question therefore remains why the introduction of more reactive transition metal atoms in copper surfaces increases the catalytic activity as well as the selectivity towards C_2 products.

A possible explanation is that substitutional atoms influence catalytic activity through their effect on the surface morphology. Dopant atoms can change the formation energy of defects, such as steps, and thereby shift reaction pathways. Establishing this connection requires a systematic comparison of the stability of CO and surface carbonyl complexes at steps vs. terraces. Surface steps provide different bonding and reaction energetics than flat terraces.

We present here results of calculations of the binding energy and minimum energy paths for CO admolecule migration on islands of Cu(100) and Cu(111) surfaces, showing how CO molecules tend to migrate to and then diffuse along the steps, thereby decorating the steps even at low CO coverage. The calculated formation energy of steps is reduced to a half when decorated with CO as compared with clean copper surfaces. The effect of introducing substitutional transition metal atoms from the first-row (Sc–Ni) and second-row (Y–Pd) at steps is also studied and their optimal location determined with and without the adsorption of CO

molecules. More than one CO admolecule binds on the substitutional atoms more strongly than on clean Cu, in some cases four, and the energy of such surface carbonyl complexes turns out to be lower at steps than on flat terraces, thereby reducing even further the formation energy of steps. The results of these calculations provide a basis for evaluating the possible effect of CO adsorption and the presence of substitutional atoms on copper surface morphology and catalytic activity, for example in CO_2 electrochemical reduction to C_2 products.

Methods

The electronic structure calculations were carried out using the BEEF-vdW functional approximation [33]. This functional has previously been found to provide a reliable description of CO adsorption on copper surfaces (see below) [30, 34]. Spin-polarized calculations were performed using a plane-wave basis with an energy cutoff of 450 eV within the projector augmented-wave (PAW) formalism, using the Vienna Ab initio Simulation Package (VASP) [35]. The Brillouin zone of the slab supercells was sampled using a $5 \times 2 \times 1$ k-point grid, which gives converged CO adsorption energy and magnetic moments. The self-consistency calculations were converged to within 10^{-6} eV and atomic coordinates were optimized until the maximum force on unconstrained atoms dropped below 0.01 eV $Å^{-1}$. The optimized lattice constant obtained for the copper crystal is 3.655 Å. The minimum energy paths for CO migration were calculated using the nudged elastic band method [36, 37].

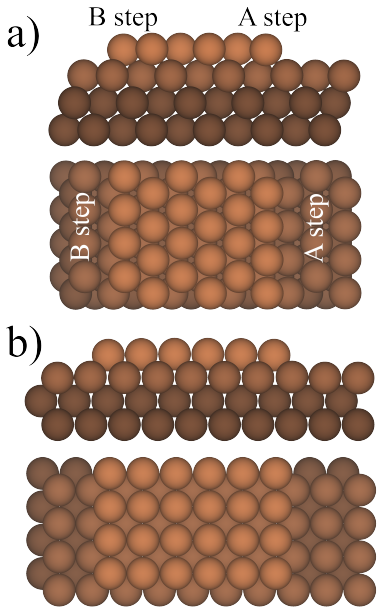

Figure 1: Side and top view of the structural models used to study steps on copper surfaces. The structure consists of a $4 \times 6 \times 1$ striped island on the surface of a $4 \times 10 \times 3$ Cu(111) slab. Atoms of the various layers are shaded differently to highlight the island atoms which have the lightest shade. (a) On Cu(111), the island has two distinct compact step structures, denoted as A- and B-type. (b) On Cu(100) the two steps on the island are equivalent.

The Cu(111) and Cu(100) surfaces were modeled by constructing a $4 \times 10 \times 3$ slab with vacuum on both

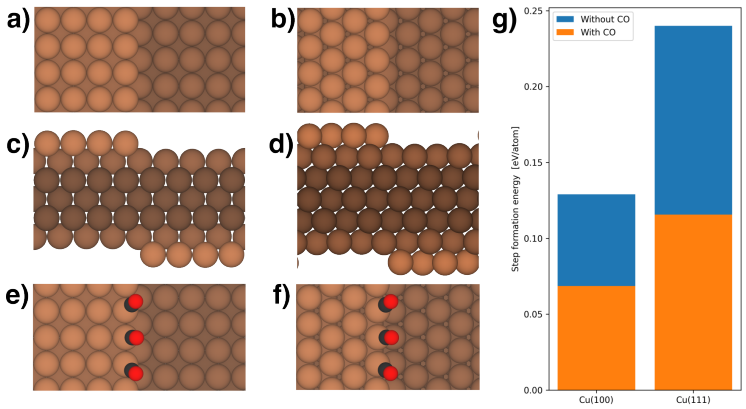

Figure 2: (a–f) Structural models for calculating the formation energy of steps on Cu(100) and Cu(111) surfaces, with and without the adsorption of CO molecules. (a–b) top view, (c–d) side view, and (e–f) top view of the surfaces with adsorbed CO. (g) Calculated step-formation energy. For clean Cu(111), the formation energy is found to be 0.24 eV per step atom, in close agreement with the experimental estimate of 0.22 eV [38]. For the less compact Cu(100) surface, a lower value of 0.13 eV/atom is found. When CO admolecules decorate the steps, the formation energy is lowered significantly, to 0.12 eV/atom for Cu(111) and to 0.07 eV/atom for Cu(100). The results for clean copper surfaces are illustrated by the top of the blue bars, while the results for CO-decorated steps are illustrated by the orange bars.

sides. A vacuum region of 20 Å separates the slab and its periodic images. The atoms in the two bottom layers of the slab were fixed at crystal positions, while the positions of the remaining of the Cu atoms were adjusted to minimize the energy. Steps on Cu(111) and Cu(100) surfaces were modeled by introducing a striped island of $4 \times 6 \times 1$. The structural models are illustrated in figure 1. This way of modeling surface steps is chosen instead of the more common periodic array of steps because it allows for easy evaluation of the step formation energy, as explained below, and the long range strain from steps does not build up as in the periodic step model. For example, the calculated binding energy of a CO molecule in the center of the island on Cu(100) is within 0.01 eV of the value calculated for a flat (100) facet, while the binding energy in the center of a micro-terrace of a (711) periodic stepped surface is 0.05 eV lower.

To determine the formation energy of steps on the surfaces, a thicker slab of $4 \times 8 \times 6$ was generated, and its energy was compared to that of a corresponding slab with striped islands on both sides of the slab, obtained by shifting half of the surface layer on one side to the other side (see figure 2). The atoms in the two central layers of the slab were fixed at crystal positions, while the position of the rest of the Cu atoms was adjusted to minimize the energy. The step formation (SF) energy was calculated as

$$E_{\mathrm{SF}} = \frac{E_{\mathrm{Cu,island}} - E_{\mathrm{Cu,flat}}}{L_{\mathrm{step}}} \tag{1}$$

where $E_{\mathrm{Cu,island}}$ and $E_{\mathrm{Cu,flat}}$ are the values of the energy of the slab with islands and flat Cu surfaces, respectively. The energy difference is divided by the step length expressed as the number of step atoms, L_{step}, yielding the formation energy per step atom.

The binding energy of a CO molecule adsorbed on a Cu surface was calculated as

$$E_{b,{}^*\mathrm{CO/Cu}} = E_{\mathrm{Cu}} + E_{\mathrm{CO(g)}} - E_{{}^*\mathrm{CO/Cu}}, \tag{2}$$

corresponding to

$$^*\mathrm{CO/Cu} \rightarrow \mathrm{CO(g)} + \mathrm{Cu}. \tag{3}$$

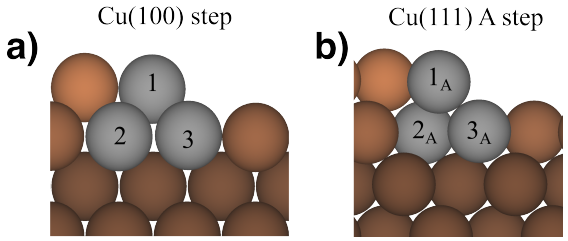

Figure 3: The various possible low energy locations of a substitutional atom of a 3d and 4d transition metal more reactive than Cu near a step on the Cu(100) surface (a), and an A-type step on the Cu(111) surface (b). The labeling of the sites at the B-type step on a Cu(111) surface is similar to that for the A-type step, but with subscript B.

The binding energy on the flat Cu(111) surface was calculated to be 0.53 eV. After subtracting zero-point energy the value reduced to 0.49 eV, matching the experimental value of 0.49 eV [39]. On the flat Cu(100) surface, the binding energy was calculated to be 0.61 eV. Subtraction of the zero-point energy reduced the value to 0.57 eV. This is in good agreement with the experimentally determined value of 0.53 eV [39, 40]. We thereby conclude that the BEEF-vdW functional approximation is a good choice.

The structures that include a more reactive transition metal atom, M, were generated by replacing a Cu atom in a terrace, subsurface, or step with a 3d (Sc–Ni) or 4d (Y–Pd) atom. The various sites near and at steps are illustrated in figure 3.

The differential binding energy of the nth CO molecule adsorbed to a substitutional atom relative to adsorption on the clean Cu surface is calculated as

$$E_{b,n^{th}\text{CO/MCu}} = E_{(^*\text{CO})_{n-1}/\text{MCu}} + E_{^*\text{CO/Cu}} - E_{(^*\text{CO})_n/\text{MCu}} - E_{\text{Cu}} \tag{4}$$

corresponding to

$$(^*\text{CO})_n\text{MCu} + \text{Cu} \rightarrow (^*\text{CO})_{n-1}\text{MCu} + {}^*\text{CO/Cu}. \tag{5}$$

The relative energy for a carbonyl complex to sit at a step rather than a terrace site was calculated as

$$\Delta E_{(^*\text{CO})n/\text{MCu}} = E^{\text{step}}_{(^*\text{CO})n/\text{MCu}} - E^{\text{terrace}}_{(^*\text{CO})_n/\text{MCu}} \tag{6}$$

where $E^{\text{step}}_{(^*\text{CO})n/\text{MCu}}$ and $E^{\text{terrace}}_{(^*\text{CO})_n/\text{MCu}}$ represent the energy of the carbonyl complex located at a step and a terrace site, respectively. A negative value of $\Delta E_{(^*\text{CO})_n/\text{MCu}}$ indicates that a step site is favored for the carbonyl complex.

Results

Step formation

The step formation energy is calculated to be 0.24 eV per step atom on the Cu(111) surface. This is in close agreement with the reported experimental results of 0.22 eV [38]. For Cu(100), the calculated step formation energy is smaller, 0.13 eV, as would be expected from the more open structure and higher surface energy. These results are illustrated in figure 2.

When CO molecules adsorb on the surface, they most likely land on a flat terrace, on top of or in between islands. The preferred binding site is on top of a Cu atom, where the binding energy is 0.53 eV on Cu(111) and 0.61 eV on Cu(100), but bridge sites also provide a weak binding site ca. 0.03 eV higher in energy. The calculated energy barrier for a diffusion hop from one on-top site to another is low, 0.06 eV. While this barrier is likely an underestimate, as is typical for generalized gradient approximation density functionals

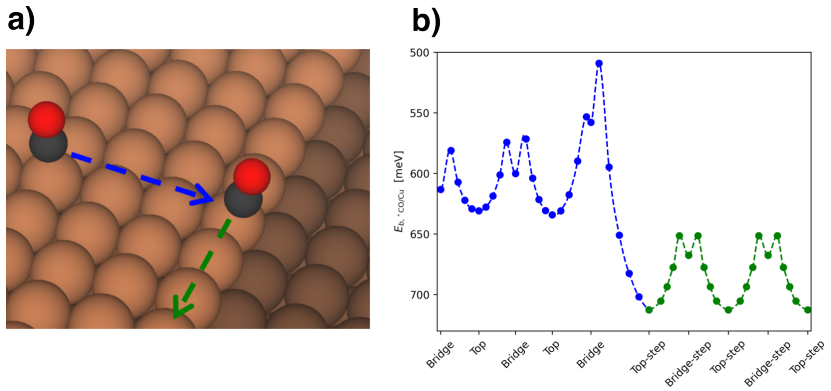

Figure 4: (a) Minimum energy path for the migration of a CO admolecule across a striped island on the Cu(100) surface to a step (blue) and then along the step edge (green). (b) Variation of the binding energy, $E_{b,^*CO/Cu}$, along the minimum energy path, using the same color coding as in (a). This shows that CO admolecules diffuse rapidly at room temperature, tend to migrate to a step where the binding is stronger, and then migrate mainly along the step edge.

such as BEEF-vdW, the diffusion of CO is indeed expected to be fast at room temperature. The minimum energy path for migration of a CO admolecule across the striped island on the Cu(100) surface to the step is shown in figure 4. The binding energy at the step is 0.1 eV larger than at the flat terrace, as would be expected from the undercoordination of the Cu step atoms. The minimum energy path shows that a CO admolecule has to overcome a barrier of 0.12 eV to reach the step site from the site on the island preceding the step. But, once the molecule has reached the step, migration along the step is facile, with a low barrier of 0.052 eV, similar to that of the flat terrace, while the barrier for leaving the step and returning to the interior of the island is significantly higher, 0.20 eV. Thus the molecules that make it to the step are expected to migrate mainly along the step edge and only rarely return to the interior of the island or to the terrace in between islands. CO admolecules are, therefore, expected to collect at steps and can decorate steps even when the overall surface coverage is low.

The lowest-energy structure for CO admolecules at a fully decorated step on Cu(100) is shown in Figure 2. The binding energy of a second CO at the step, with one vacant on-top site between that and the first one, is almost the same as for the first one, 0.1 eV larger than at the Cu(100) terrace. The site in between can also be filled, but the energy lowering is then just 0.01 eV with respect to binding at the terrace. The fully decorated step can, therefore, have 3 out of 4 on-top sites filled. As can be seen from figure 2, the two outer CO molecules tilt away from the central one in the trimer. The migration of three CO molecules to 4 adjacent sites on the Cu(100) step lowers the energy by ca. 0.2 eV, and the step formation energy is thereby lowered from 0.13 eV to 0.07 eV per step atom, as illustrated in figure 2.

The decoration of CO at steps on the Cu(111) surface is energetically even more favorable than at Cu(100), both for the A-type and B-type steps, where also 3 out of 4 on-top sites can be filled, with the energy lowering for the first CO being 0.19 eV, the second 0.18 eV, and the third 0.13 eV, with respect to binding on the Cu(111) terrace. On Cu(111) the step formation energy decreases from 0.24 eV to 0.12 eV per step atom. Thus, CO adsorption lowers the step formation energy to a half on both of these most stable surfaces of copper. This stabilization originates from the stronger binding of CO to the undercoordinated Cu atoms at the steps than at flat terraces.

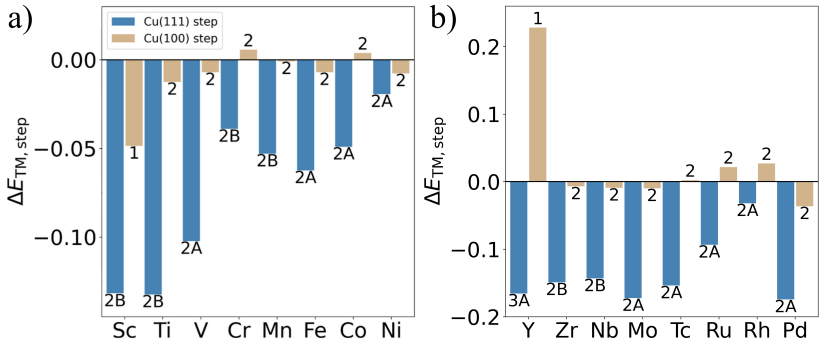

Figure 5: Difference in energy when a substitutional atom (from the 3d row in (a), and from the 4d row in (b)) is located near a step vs. a terrace site on Cu(100) and Cu(111) surfaces. The label at each bar indicates the minimum energy location of the substitutional atom as defined in figure 3.

Substitutional atoms

The introduction of a substitutional atom near a step can involve several different sites. For a step on Cu(100), as well as the steps on Cu(111), there are three locations that are found to be preferred, depending on the type of atom. These locations are shown in figure 3 for the step on Cu(100) and the A-type step on Cu(111). The preferred sites at the B-type step on Cu(111) are equivalent. These sites are the exposed step (denoted 1), the covered subsurface at the step (denoted 2), or the exposed subsurface at the step (denoted 3). The subscript indicates which type of step on the Cu(111) surface is being referred to. Some types of substitutional atoms actually sit preferably at the terrace, either at surface or subsurface sites. This is the case most strongly for Y in the Cu(100) surface, but also to a lesser extent for Cr, Co, Ru and Rh. Figure 5 shows the difference in energy between the lowest energy location at a step and at a terrace site. A negative value indicates that the substitutional atom preferentially segregates to a step. In most cases, there is only a small difference in the energy for the equivalent sites at A-type and B-type steps, Sc being an exception where the difference is 0.1 eV in favor of the B-type step.

The addition of CO on surfaces with more reactive transition metal substitutional atoms leads to many different structures and has a significant effect on the stability of steps. Figure 6 shows examples of minimum energy configurations of CO molecules adsorbed on a substitutional atom at a Cu(100) step, and A- and B-type steps on Cu(111).

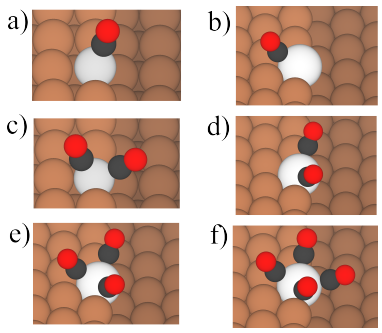

Figure 6: (a) CO bound to a Cr substitutional atom at a Cu(100) step. (b) CO bound to Sc substitutional atom at an A-type step on Cu(111). (c) Two CO molecules bound to Cr at Cu(100) step. (d) Two CO molecules bound to a Sc atom at an A-type step on Cu(111). (e) Three CO molecules bound to a Sc atom. (f) Four CO molecules bound to a Sc atom.

Adsorption of 1 to 4 CO molecules on Cr and Sc substitutional atoms is shown. A single CO admolecule on Cr tilts slightly away from the step. Equivalent structures were found for the first CO adsorbed to V–Ni, and Nb–Pd at both the Cu(100) and the Cu(111) steps. However, CO bound to a Sc atom points towards the center of the islands, and equivalent minimum energy structures were obtained for Sc–Ti and Y–Zr.

The figure also shows a minimum energy structure where two CO molecules are bound to a Cr substitutional atom. They point perpendicular to the step. Such a structure was found to be of minimum energy for Cr–Ni and Mo–Pd at all the investigated steps. However, when two CO molecules are bound to a Sc substitutional atom, they point parallel to the step. Such a structure was found to be of minimum energy for Sc–V and Y–Nb at all steps. When three CO molecules bind to a Sc substitutional atom at the Cu(111) A-type step, two of the CO molecules point away from the step, while a single CO molecule points towards the center of the island. Similar minimum energy structure was found for three admolecules at the other substitutional atoms at all the steps. Up to four CO molecules can be adsorbed to a Sc substitutional atom at the Cu(111) A step, more strongly than at the clean terrace. As shown in figure 6, two of the CO molecules point parallel to the step, while a single CO molecule points away from the step and another points towards the interior of the island. Similar minimum energy structures were found for all substitutional atoms and the different types of steps when four CO molecules can be adsorbed.

Figure 7 shows the calculated differential binding energy, $E_{b,n^{\text{th}}\text{CO/MCu}}$, for the first and up to fourth CO molecule on a 3d (Sc–Ni) and 4d (Y–Pd) substitutional step atom minus the binding energy of CO on the corresponding clean copper facet. For all three types of steps, adsorption of the first CO molecule is weakly favorable or even slightly unfavorable as for Sc–Mn and Y–Mo. This is due to the cost of bringing the substitutional atom to the exposed step site. This is particularly pronounced for Ti, Mn, Y, Zr and Nb.

Moving across the 3d and 4d rows, the relative differential binding energy of the first CO molecule generally increases, reaching approximately 0.5–0.9 eV for the late transition metals Fe–Ni and Tc–Pd. For all the substitutional atoms, the second and even the third CO molecule binds more strongly than the first. The largest differential binding energy is found for the elements in the middle of the rows, where adsorption of the third CO molecule can be more than 1 eV stronger than the binding at the clean terrace. For V–Fe and Nb–Mo, the third CO molecule is generally most strongly bound. Adsorption of a fourth CO molecule coming from a clean terrace is favorable only for some of the substitutional atoms. For Sc–Cr and Y–Nb (and Mn and Tc in the case of the Cu(111) A step), the fourth CO molecule binds strongly enough to be energetically favorable compared with binding on the corresponding clean copper terrace, but the differential binding energy is smaller than for the second and third CO molecules. In contrast, adsorption of a fourth CO molecule becomes unfavorable for the middle and late transition metals, particularly Mn–Co and Tc–Rh (except for the A-type step cases noted above). The Cu(111) A-type and B-type steps exhibit similar adsorption trends across both transition-metal rows. The Cu(100) step shows the same overall behavior,

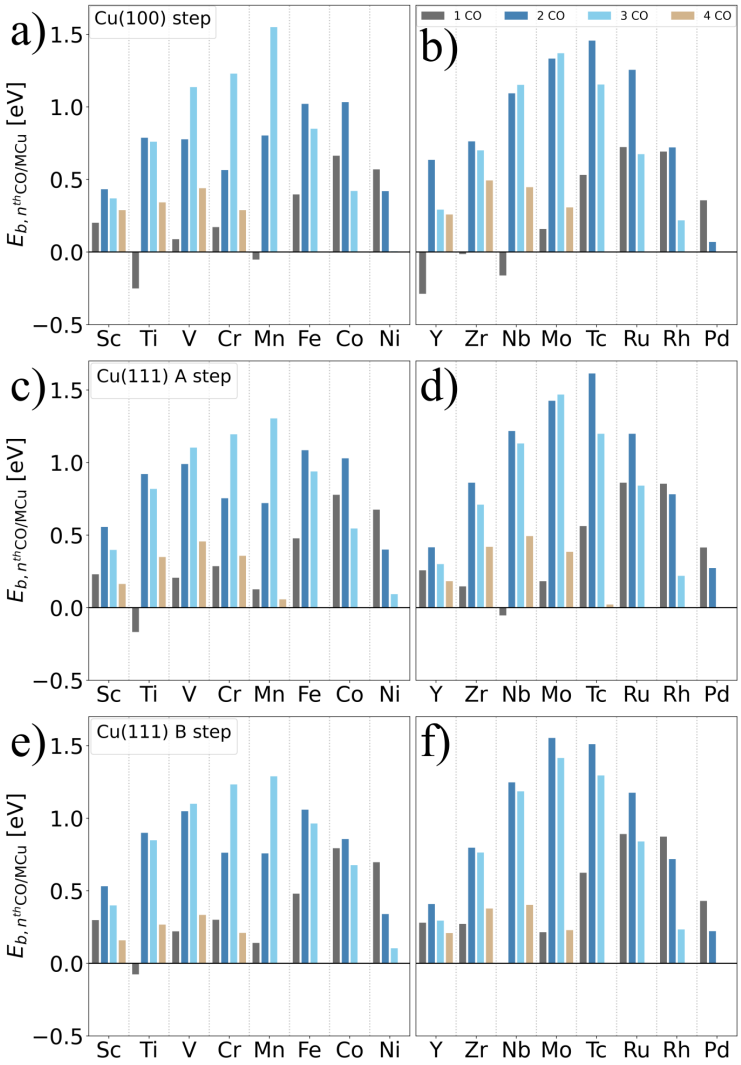

Figure 7: Differential binding energy, $E_{b,n^{th}\mathrm{CO/MCu}}$, for first and up to fourth CO molecule bound to a 3d (left panels) or 4d (right panels) substitutional step atom with respect to binding on the corresponding clean copper terrace. (a,b): at a step on Cu(100). (c,d): at an A-type step on Cu(111). (e,f): at a B-type step on Cu(111). A missing bar means that the additional CO binds more strongly on the clean copper terrace.

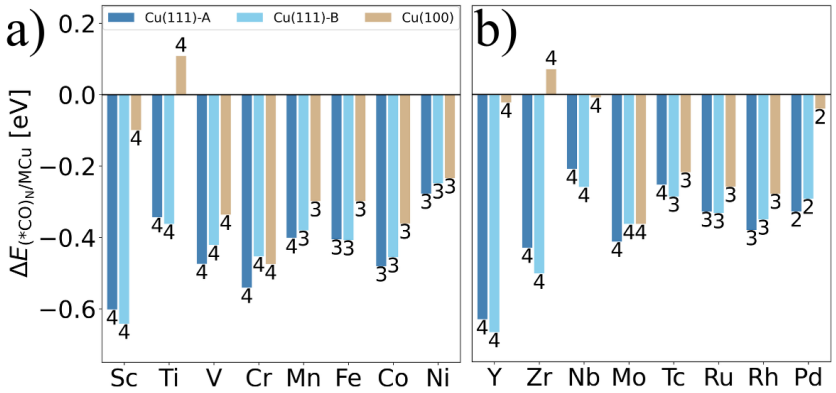

Figure 8: Difference in energy, $\Delta E_{(*\mathrm{CO})_n/\mathrm{MCu}}$, between a step and a terrace location of the surface carbonyl complex, i.e. substitutional atom and the adsorbed CO molecules bound to it. (a) and (b) for 3d and 4d transition metal substitutional atoms, resp. A negative value indicates that the carbonyl complex is energetically more stable at the step relative to the terrace. The number shown at the top of each bar is the maximum number of CO admolecules that bind to the substitutional atom more strongly than on the corresponding clean copper terrace.

although larger variations in differential binding energy are observed for several of the early transition metals. Overall, the calculated results show that the substitutional atoms located at steps on Cu(111) and Cu(100) surfaces can adsorb multiple CO molecules, with the strongest differential binding energy generally found for the second or third CO molecule.

The binding of CO molecules to a substitutional atom strongly affects the relative energy of a step vs. a terrace site. Figure 8 shows the energy difference, $\Delta E_{(*\mathrm{CO})_n/\mathrm{MCu}}$, between the most stable surface carbonyl complex located at a step and at the corresponding flat terrace. The terrace carbonyl-complex energy is taken from our previous calculations of CO adsorption on transition metal substitutional atoms in Cu(100) and Cu(111) terraces [30]. The resulting energy differences represent the energetic preference of the surface carbonyl complexes for step sites. For nearly all the substitutional atoms studied here, $\Delta E_{(*\mathrm{CO})_n/\mathrm{MCu}}$ is negative, indicating that the carbonyl complex is more stable at a step than at a flat terrace. The stabilization is particularly pronounced for the Cu(111) steps, where values between ca. -0.2 and -0.7 eV are obtained for both 3d and 4d atoms. The largest reduction in energy is observed for Sc, Y, Cr and Zr. The two types of steps on the Cu(111) surface exhibit similar trends for both 3d and 4d substitutional atoms. In contrast, the Cu(100) step displays a stronger dependence on the type of the substitutional atom. For most substitutional atoms, the Cu(100) step site is more stable than the corresponding terrace site, although the reduction in energy is generally smaller than for the Cu(111) steps. Two exceptions are observed, Ti and Zr exhibit a slight preference for the Cu(100) terrace relative to the step. The number shown at the top of each bar in figure 8 indicates the maximum number of CO molecules that are bound more strongly than at the clean copper terrace, as determined from the differential adsorption energy shown in figure 7. Early transition metals generally adsorb up to four CO molecules, whereas the middle and late transition metals typically adsorb three. Pd only adsorbs two CO molecules. The energetic preference of the carbonyl complexes for step sites as compared to terrace sites translates into a lowering of the step formation energy.

Discussion

The results of the calculations presented here show how the presence of CO can enhance the tendency for step formation on copper surfaces. The calculated step formation for clean Cu(111) is in close agreement

with the available experimental estimate [38], and by decorating 3/4 of the sites on a step with CO, the formation energy is reduced to a half compared to the clean surface, both for Cu(111) and Cu(100). This is consistent with the experimental observation that steps tend to form during CO_2 electroreduction on copper, as CO is a common intermediate (although not for the competing mechanism leading to formation of formate [41]). These results are consistent with the recent work of Cheng et al. [8], whose calculations show that CO adsorption stabilizes periodic stepped Cu surfaces with respect to flat terraces for a range in CO pressure and applied voltage.

This is likely of particular importance for C-C bonding as in ethylene formation. The calculated energy landscape shows that CO admolecules tend to migrate to steps and subsequently diffuse along step edges. This will increase the probability of two or more molecules meeting up and forming C-C bonds. If the coverage of CO under realistic CO_2 reduction conditions is rather low, the statistical enhancement of bringing two CO molecules to adjacent sites is likely an important factor in C-C bond formation.

When a substitutional atom of a more reactive 3d and 4d transition metal is introduced in a copper surface with an island, there are several possible sites and there is, in general, not a strong energetic preference for a site near or at a step. However, when CO molecules are introduced, the substitutional atoms readily adsorb more than one CO and the preference for a step site becomes strong.

The binding of more than one and up to four CO molecules at a substitutional atoms is analogous to what we have previously reported for flat Cu(100) and Cu(111) surfaces [30]. For both the 3d and 4d substitutional atoms, the strongest differential adsorption energy is generally associated with the second and third CO molecules, while adsorption of a fourth CO molecule is favorable only for the early transition metals (Sc-Mn, and Y-Tc). At the same time, the steps significantly influence the energetic stability of the resulting carbonyl complexes. Comparison with the terrace structures shows that the majority of the carbonyls are stabilized at Cu steps relative to the corresponding terrace sites, Ti and Zr being two exceptions. This stabilization is particularly pronounced for the Cu(111) A- and B-type steps, where all the substitutional atoms have an energetic preference for the step after adsorption of CO molecules. The results furthermore show that the adsorption of additional CO molecules leads to a stronger preference for step sites. For a Y substitutional atom in the Cu(100) island surface, for example, there is a 0.2 eV preference for a terrace site, but after binding four CO molecules this switches to a preference of -0.02 eV for the step. The opposite trend observed for Ti and Zr at Cu(100) steps results from a special adsorption site for the CO, which is at a bridge between the substitutional atom and a neighboring Cu atom. Since a step provides fewer such bridge sites than the terrace, adsorption of the fourth CO molecule becomes less favorable at a step.

The energetic preference for carbonyl complexes to be located at steps likely arises from the lower coordination of the substitutional atom and the greater structural flexibility of the step environment. The reduced coordination of the substitutional atom increases the driving force for CO adsorption, and the undercoordinated step geometry more readily accommodates the structural distortions associated with multiple CO adsorption. In several cases, the substitutional atom partially protrudes from the Cu lattice upon adsorption of multiple CO molecules, weakening the bonding to the neighboring Cu atoms while strengthening the bonding to the CO molecules. Such a relaxation is more difficult to accommodate on flat terraces and may contribute to the enhanced stability of the carbonyl complex at steps, particularly on the more closely packed Cu(111) surface.

The lowering of the energy as a substitutional atom gets to sit at a step site rather than at a flat terrace reduces step formation energy. Experiments on a similar system, Pd substitutional atoms in Cu(111), have showed such an effect [23]. In the presence of adsorbed hydrogen, the density of steps is strongly increased. The results of the calculations presented here suggest that analogous effects may occur during CO_2 reduction where CO is formed as an intermediate. For example, the experimental observation of an increased yield of ethylene in CO_2 electroreduction when a small amount, around 1%, of Co is added to copper electrodes [13] could be due to increased step density, and thereby greater probability of two or more CO admolecules sitting at adjacent sites, a prerequisite for C–C bond formation. The effect of adding Co on the product selectivity would thereby be indirect, through changes in the surface morphology.

The possible magnitude of this effect can be illustrated with an example where the Co surface concentration is 1%, with 10% of the surface atoms located at steps and all Co atoms occupying step sites. Then, one in ten step atoms are Co. After adsorption of CO, the presence of the Co atom will lead to a further reduction of the step energy of roughly 0.04 eV per step atom on the Cu(100) surface, and 0.05 eV per step atom on the Cu(111) surface. This is significant for the step formation on both surfaces, as the presence of

the substitutional atom would reduce the step-formation energy of the Cu(100) surface from 0.07 eV/atom to approximately 0.03 eV/atom, and it would reduce the step-formation energy of Cu(111) from 0.12 eV/atom to 0.07 eV/atom.

The stabilization of the surface carbonyl complexes at the steps may also help maintain a higher step density by pinning existing steps. Scanning tunneling microscopy measurements show that Cu steps fluctuate rapidly at room temperature through kink motion and atomic diffusion [42, 43]. A fluctuating step could therefore encounter a substitutional atom or surface carbonyl complex initially located in a terrace, without requiring the impurity itself to migrate towards the step. Subsequent migration of the step away from the substitutional atom would then incur the associated energy cost of returning the carbonyl complex to a less favorable terrace site. The surface carbonyl complexes may in this way pin the mobile steps, hindering their disappearance and helping to sustain a higher step density. This provides a possible consequence of the calculated energetic stabilization, but the lifetime of such pinning would depend on the energy barriers for the corresponding atomic rearrangements.

Testing these hypotheses will require more detailed calculations and simulations of long time scale evolution. The relevance to electrochemical settings should also include the effect of applied voltage and presence of electrolyte. Such investigations are, however, outside the scope of the present study.

Conclusion

The results presented here show that CO admolecules diffuse rapidly on Cu(111) and Cu(100) surfaces and tend to migrate to steps where the binding energy is stronger because of the undercoordination of the Cu atoms. After a CO molecule has reached a step, the diffusion will mainly be one-dimensional, along the step, and CO molecules will tend to collect at the step, generating a substantial local coverage there even though the overall coverage may be low. This may be an important aspect of C-C bonding in, for example, ethylene formation during CO_2 electrochemical reduction. At the same time, the presence of CO lowers the calculated step formation energy to a half on both Cu(111) and Cu(100) surfaces. The presence of CO as an intermediate in CO_2 electrochemical reduction will, therefore, tend to increase step density on copper surfaces. This is consistent with experimental observations where initially flat copper surfaces are found to become rough during the reduction reaction.

Substitutional 3d (Sc–Ni) and 4d (Y–Pd) transition metal atoms at steps on Cu(111) and Cu(100) surfaces can adsorb multiple CO molecules more strongly than a CO at a clean copper site, up to four in some cases. The differential binding energy can even increase as additional CO molecules adsorb, making the second and third CO molecules more strongly bound than the first one. While steps do not in general offer significantly lower energy sites for the substitutional atoms, the binding of CO molecules changes that and the carbonyl complexes have a strong preference for step sites, thereby also reducing step formation energy on both (111) and (100) facets of copper.

Recently reported experimental studies have highlighted the importance of steps on copper surfaces for CO_2 electroreduction activity, and the introduction of more reactive transition metal substitutional atoms has been shown to affect selectivity, increasing for example the production of ethylene. The present results suggest that these two effects can be connected through the lowering of step formation energy by the presence of CO and surface carbonyl complexes and the increased probability of CO admolecules being found on adjacent sites when steps are present, thereby setting the stage for C–C bond formation. More generally, this highlights the importance of considering both multiple admolecule binding and catalyst restructuring when modeling single-atom alloy catalysts under reaction conditions.

Acknowledgments

This work was funded by the EU's Horizon 2021 programme under the Marie Skłodowska-Curie Doctoral Networks (MSCA-DN) grant agreement No 101072830 (ECOMATES). Views and opinions expressed are those of the authors and do not necessarily reflect the official policy or position of the European Union or the Granting Authority, and neither can be held responsible for them.

References

(1) Hori, Y.; Takahashi, I.; Koga, O.; Hoshi, N. *J. Phys. Chem. B* **2002**, *106*, 15–17.

(2) Hori, Y.; Takahashi, I.; Koga, O.; Hoshi, N. *J. Mol. Catal. A Chem.* **2003**, *199*, 39–47.

(3) Schouten, K. J. P.; Qin, Z.; Pérez Gallent, E.; Koper, M. T. M. *J. Am. Chem. Soc.* **2012**, *134*, 9864–9867.

(4) Hussain, J.; Jónsson, H.; Skúlason, E. *ACS Catal.* **2018**, *8*, 5240–5249.

(5) Bagger, A.; Ju, W.; Varela, A. S.; Strasser, P.; Rossmeisl, J. *ACS Catal.* **2019**, *9*, 7894–7899.

(6) Kolb, M. J.; Loffreda, D.; Sautet, P.; Calle-Vallejo, F. *J. Catal.* **2021**, *395*, 136–142.

(7) Calle-Vallejo, F.; Koper, M. T. *ACS Catal.* **2017**, *7*, 7346–7351.

(8) Cheng, D.; Nguyen, K.-L. C.; Sumaria, V.; Wei, Z.; Zhang, Z.; Gee, W.; Li, Y.; Morales-Guio, C. G.; Heyde, M.; Roldan Cuenya, B., et al. *Nat. Commun.* **2025**, *16*, 4064.

(9) Eren, B.; Zherebetskyy, D.; Patera, L. L.; Wu, C. H.; Bluhm, H.; Africh, C.; Wang, L.-W.; Somorjai, G. A.; Salmeron, M. *Science* **2016**, *351*, 475–478.

(10) Roiaz, M.; Falivene, L.; Rameshan, C.; Cavallo, L.; Kozlov, S. M.; Rupprechter, G. *J. Phys. Chem. C* **2019**, *123*, 8112–8121.

(11) Amirbeigiarab, R.; Tian, J.; Herzog, A.; Qiu, C.; Bergmann, A.; Roldan Cuenya, B.; Magnussen, O. M. *Nat. Catal.* **2023**, *6*, 837–846.

(12) Wei, J.; Zhang, Z.; Gee, W.; Wei, Y.; Zhou, Y.-W.; Herran, M.; Sautet, P.; Alexandrova, A. N.; Roldan Cuenya, B.; Kley, C. S. *J. Am. Chem. Soc.* **2025**, *147*, 45178–45188.

(13) Soodi, S.; Zhang, J.-J.; Zhang, J.; Liu, Y.; Lashgari, M.; Zafeiratos, S.; Züttel, A.; Zhao, K.; Luo, W. *Chem. Synth.* **2024**, *4*, 44.

(14) Bernal, M.; Bagger, A.; Scholten, F.; Sinev, I.; Bergmann, A.; Ahmadi, M.; Rossmeisl, J.; Cuenya, B. *Nano Energy* **2018**, *53*, 27–36.

(15) Yan, Y.; Zhao, Z.; Zhao, J.; Tang, W.; Huang, W.; Lee, J.-M. *J. Mater. Chem. A* **2021**, *9*, 7496–7502.

(16) Xu, C.; Vasileff, A.; Jin, B.; Wang, D.; Xu, H.; Zheng, Y.; Qiao, S. *ChemComm* **2020**, *56*, 11275–11278.

(17) Rahaman, M.; Kiran, K.; Montiel, I. Z.; Grozovski, V.; Dutta, A.; Broekmann, P. *Green Chem.* **2020**, *22*, 6497.

(18) Li, J. et al. *Nat. Commun.* **2020**, *11*, 3685.

(19) Xie, Y. et al. *Nat. Catal.* **2022**, *5*, 564–570.

(20) Hannagan, R. T.; Giannakakis, G.; Flytzani-Stephanopoulos, M.; Sykes, E. C. H. *Chem. Rev.* **2020**, *120*, 12044–12088.

(21) Cui, X.; Li, W.; Ryabchuk, P.; Junge, K.; Beller, M. *Nat. Catal.* **2018**, *1*, 385–397.

(22) Yang, X.-F.; Wang, A.; Qiao, B.; Li, J.; Liu, J.; Zhang, T. *Acc. Chem. Res.* **2013**, *46*, 1740–1748.

(23) Kyriakou, G.; Boucher, M. B.; Jewell, A. D.; Lewis, E. A.; Lawton, T. J.; Baber, A. E.; Tierney, H. L.; Flytzani-Stephanopoulos, M.; Sykes, E. C. H. *Science* **2012**, *335*, 1209–1212.

(24) Réocreux, R.; Stamatakis, M. *Acc. Chem. Res.* **2021**, *55*, 87–97.

(25) Lee, J. D.; Miller, J. B.; Shneidman, A. V.; Sun, L.; Weaver, J. F.; Aizenberg, J.; Biener, J.; Boscoboinik, J. A.; Foucher, A. C.; Frenkel, A. I., et al. *Chem. Rev.* **2022**, *122*, 8758–8808.

(26) Schumann, J.; Stamatakis, M.; Michaelides, A.; Réocreux, R. *Nat. Chem.* **2024**, *16*, 749–754.

(27) Simonovis, J. P.; Hunt, A.; Palomino, R. M.; Senanayake, S. D.; Waluyo, I. *J. Phys. Chem. C.* **2018**, *122*, 4488–4495.

(28) Wang, Y.; Schumann, J.; Happel, E. E.; Çınar, V.; Sykes, E. C. H.; Stamatakis, M.; Michaelides, A.; Hannagan, R. T. *J. Phys. Chem. Lett.* **2022**, *13*, 6316–6322.

(29) Christiansen, M. A. H.; Peña-Torres, A.; Jónsson, E. Ö.; Jónsson, H. *J. Phys. Chem. Lett.* **2024**, *15*, 5654–5658.

(30) Christiansen, M. A.; Wang, W.; Jónsson, E. Ö.; Cicero, G.; Jónsson, H. *ChemCatChem* **2025**, *17*, e00765.

(31) Berger, F.; Schumann, J.; Réocreux, R.; Stamatakis, M.; Michaelides, A. *J. Am. Chem. Soc.* **2024**, *146*, 28119–28130.

(32) Wang, W.; Salomone, M.; Re Fiorentin, M.; Risplendi, F.; Cicero, G. *ACS Electrochem.* **2025**, *1*, 2512–2520.

(33) Wellendorff, J.; Lundgaard, K. T.; Møgelhøj, A.; Petzold, V.; Landis, D. D.; Nørskov, J. K.; Bligaard, T.; Jacobsen, K. W. *Phys. Rev. B* **2012**, *85*, 235149.

(34) Wellendorff, J.; Silbaugh, T. L.; Garcia-Pintos, D.; Nørskov, J. K.; Bligaard, T.; Studt, F.; Campbell, C. T. *Surf. Sci.* **2015**, *640*, 36–44.

(35) Kresse, G.; Furthmüller, J. *Phys. Rev. B* **1996**, *54*, 11169–11186.

(36) Jónsson, H.; Mills, G.; Jacobsen, K. W. In *Classical and Quantum Dynamics in Condensed Phase Simulations*; World Scientific: 1998, pp 385–404.

(37) Henkelman, G.; Uberuaga, B. P.; Jónsson, H. *J. Chem. Phys.* **2000**, *113*, 9901–9904.

(38) Schlößer, D. C.; Verheij, L. K.; Rosenfeld, G.; Comsa, G. *Phys. Rev. Lett.* **1999**, *82*, 3843.

(39) Vollmer, S.; Witte, G.; Wöll, C. *Catal. Lett.* **2001**, *77*, 97–101.

(40) Truong, C. M.; Rodriguez, J.; Goodman, D. *Surf. Sci.* **1992**, *271*, L385–L391.

(41) Van den Bossche, M.; Rose-Petruck, C.; Jónsson, H. *J. Phys. Chem. C* **2021**, *125*, 13802–13808.

(42) Giesen-Seibert, M.; Jentjens, R.; Poensgen, M.; Ibach, H. *Phys. Rev. Lett.* **1993**, *71*, 3521–3524.

(43) Poensgen, M.; Wolf, J. F.; Frohn, J.; Giesen, M.; Ibach, H. *Surf. Sci.* **1992**, *274*, 430–440.

CO coadsorption stabilizes step sites in Cu SAAs

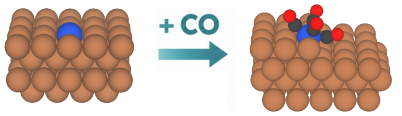

Terrace
MCu(100)

Step
$M(CO)_4$/Cu(100)